# Micro and nano-structured materials with controlled radiative properties for radiative cooling applications

Atousa Pirvaram

A DISSERTATION *SUBMITTED TO

THE FACULTY OF GRADUATE STUDIES

IN PARTIAL FULFILLMENT OF THE REQUIREMENTS

FOR THE DEGREE OF

DOCTOR OF PHILOSOPHY*

GRADUATE PROGRAM IN MECHANICAL ENGINEERING

YORK UNIVERSITY

TORONTO, ONTARIO

December 2024

# Abstract

In response to global environmental crises like climate change, urban heat islands, and rising energy demands, this thesis investigates innovative solutions through radiative cooling (RC) materials and systems. It assesses RC technologies' potential to mitigate climate change by evaluating their global warming potential (GWP) and radiative forcing (RF) using life cycle assessment (LCA) methods. RC materials are compared with conventional construction and roofing materials, highlighting their significant impact on reducing global warming.

One RC material exhibiting an average solar reflectance ($\bar{R}_{solar}$) of 98.2% and an average long-wavelength infrared emittance of ($\bar{\varepsilon}_{LWIR}$) 98.5%, achieved a net cooling power of 160.8 $W \cdot m^{-2}$, leading to a GWP of -252 $kgCO_2\text{-}eq \cdot m^{-2}$ over 20 years and -333 $kgCO_2\text{-}eq \cdot m^{-2}$ over 100 years, with an RF value of -1.01 $W \cdot m^{-2}$ when covering 1% of the Earth's surface, indicating a substantial reduction in radiative forcing compared to conventional materials.

The thesis also explores using reflective undersides to enhance RC performance by redirecting thermal emissions and reducing heat loss. Numerical simulations with Monte Carlo ray-tracing techniques evaluated various configurations, including flat and parabolic reflectors. Results show that, under ideal conditions with selective emittance spectra and no solar absorption or convection, parabolic reflectors can lower steady-state temperatures to ~230 K at 300 K ambient temperature.

Another focus was designing novel micro- and nano-structured materials with controlled radiative properties for passive daytime radiative cooling (PDRC). Enhanced PVDF-HFP-based porous materials were developed using the phase inversion method, achieving high solar reflectivity and long-wave infrared emissivity, such as the (1-8-1.25) sample. These materials minimize solar heat absorption and optimize thermal radiation through the atmospheric window.

Experimental validation included outdoor testing and dew condensation experiments, demonstrating the practicality of PDRC systems. The findings underscore RC technologies' potential to reduce cooling energy demands and mitigate global warming, positioning them as a promising solution for sustainable urban and building environments.

# Acknowledgments

As I conclude my PhD journey, I find myself reflecting not only on the academic and scientific achievements I've made but also on the profound personal growth I have experienced throughout this process.

First and foremost, I want to thank **God** for guiding me through this journey. It is through this experience that I have come to know myself better, discovering strengths I never knew I had and developing resilience in the face of harsh conditions. There were times when challenges seemed impossible to deal with, and I often felt lost, questioning my abilities and my path. Yet, with each obstacle I faced, I learned to cope with failure and rise again, discovering the strength to adapt, learn, and find solutions. This transformative journey has shaped me into a more resilient and resourceful individual, capable of confronting challenges with a newfound sense of confidence.

I would like to express my heartfelt gratitude to my supervisors, **Prof. Paul G. O'Brien** and **Prof. Siu Ning (Sunny) Leung**. Your unwavering belief in me and your guidance were instrumental during the most challenging times. Your mentorship taught me not only about research but also about perseverance and dedication, encouraging me to reach my fullest potential. You have set an example of kind-heartedness, dedication, and support, serving as role models in my life and inspiring me to embody these qualities in my own journey. You have encouraged me to strive to be not just a knowledgeable dweller on this Earth but a true human, open to helping any living being in our collective pursuit of a better world.

I also want to express my gratitude to **my family**, who stood by me with unwavering support. Your love, patience, and understanding were my greatest comfort during the late nights and stressful days. You believed in me when I struggled to believe in myself, and for that, I am eternally grateful. You taught me to be empathic toward all living beings, instilling in me the first encouragement to pursue my PhD journey with a focus on helping our planet and all its inhabitants.

I would also like to thank my committee members for their invaluable support. **Prof. Thomas Cooper**, your profound knowledge and insights helped me navigate numerous challenges; each time I reached out for assistance, you provided guidance that made a significant difference. **Prof. Cuiying Jian**, your careful review of my PhD progress was instrumental in keeping me on track and motivated throughout this journey. Your constructive feedback and encouragement helped me refine my work and push through difficult moments.

I would like to acknowledge the **LIED group** (UMR 8236 Laboratoire Interdisciplinaire des Energies de Demain) at Université Paris Cité, where I had the privilege of completing an internship under the guidance of Professor **Laurent Royon** and his dedicated team.

Finally, I want to acknowledge the countless **moments of self-discovery** I experienced during this journey. Each challenge I encountered pushed me to grow, not just as a researcher but as a person. I emerge from this experience not only with a PhD but with a deeper understanding of myself and the world around me.

Thank you to everyone who played a role in this journey; your support and encouragement have been invaluable in helping me become who I am today.

# Table of Contents

# Table of Figures

**Chapter 2**



**Chapter 3**

**Chapter 4**

**Chapter 5**



**Chapter 6**

# List of Tables

# List of Abbreviations and Acronyms

**AZO**: Al-doped Zinc Oxide

**BECCS**: Bioenergy with Carbon Capture and Storage

**CDR**: Carbon Dioxide Removal

**CMM**: Conical Metamaterial

**COP**: Coefficient of Performance

**DPHA**: Dipentaerythritol Penta-/Hexa-acrylate

**EIPS**: Evaporation-Induced Phase Separation

**FTIR**: Fourier Transform Infrared

**GWP**: Global Warming Potential

**HVAC**: Heating, Ventilation, and Air Conditioning

**IEA**: International Energy Agency

**IPCC**: Intergovernmental Panel on Climate Change

**L/H-DPE:** Low-/High-Density Polyethylene

**LCA**: Life Cycle Assessment

**LWIR:** Long-Wave Infrared

**MCRT**: Monte Carlo Ray Tracing

**NETs:** Negative Emissions Technologies

**NIPS**: Non-Solvent Induced Phase Separation

**PDRC:** Passive Daytime Radiative Cooling

**PE**: Polyethylene

**PEAs:** Polyethylene Aerogels

**PET**: Polyethylene Terephthalate

**PDMS:** Polydimethylsiloxane

**PMMA**: Polymethyl Methacrylate

**PVDF:** Polyvinylidene Difluoride

**PVDF-HFP**: Polyvinylidene Fluoride-Hexafluoropropylene

**PVC:** Polyvinyl Chloride

**PVF (Tedlar)**: Polyvinyl Fluoride

**RC:** Radiative Cooling

**RH**: Relative Humidity

**RF:** Radiative Forcing

**SBS**: Styrene-Butadiene-Styrene Block Copolymer

**SEM:** Scanning Electron Microscope

**SRM**: Solar Radiation Management

**TCOs:** Transparent Conducting Oxides

**TIPS**: Thermally Induced Phase Separation

**TOA:** Top of the Atmosphere

**TPX**: Polymethyl Pentene

**UV-Vis-NIR:** Ultraviolet, Visible, and Near-Infrared Spectroscopy

**VIPS**: Vapor-Induced Phase Separation

# List of Symbols

**A**: Area of the top surface of the radiator.

$\mathbf{AGWP_i(H)}$: Absolute global warming potential for substance i in H years.

$\mathbf{AGWP_{CO_2}(H)}$: Absolute global warming potential for $CO_2$ in H years

$\mathbf{A_{RCi}}$: Projected area of RCi on the horizontal plane.

$\mathbf{A_{tropopause}}$: Area of the tropopause.

**c**: Speed of light in a vacuum.

$\varepsilon_{atm}(\lambda, \theta)$: Spectral directional emittance of the atmosphere.

$\varepsilon_{RC}(\lambda)$: Spectral emittance of the radiator.

$\varepsilon_{AW}$: Emittance of the radiative cooler over the atmospheric window.

$\varepsilon_{sky}(\lambda)$: Emittance of the sky.

$\mathbf{F_{emit\delta-\gamma}}$: Fraction of diffuse rays leaving the RC and propagating into the sky with a zenith angle between δ and γ radians.

$\mathbf{F_{refl0-\frac{\pi}{18}}}$: Fraction of reflected rays from the parabolic reflectors towards the sky in the angle range of 0-π/18.

**f**: Focal length.

$\mathbf{G_{AM1.5}}$: Solar air mass 1.5 (AM1.5) irradiance spectrum.

$\mathbf{GWP_{RCi}(H)}$: Global warming potential of an RC material structure.

$\mathbf{h_p}$: Planck's constant.

**H**: Height.

$\mathbf{I_{BB}}$: Spectral intensity of a blackbody.

$\mathbf{k_B}$: Boltzmann constant.

λ: Wavelength of radiation.

$\mathbf{P_{Incoming,TOA}}$: Incoming solar radiation at the TOA.

$\mathbf{P_{Outgoing,TOA}}$: Outgoing thermal radiation emitted by the Earth at the TOA.

$\mathbf{P_{Nonrad}}$: Heat exchange with the surrounding environment via convection and conduction.

$\mathbf{P_{RC-sky}}$ : Power radiated directly towards the sky.

$\mathbf{P_{RC-Earth}}$ : Radiative power exchange of the RC with the Earth.

$\mathbf{P_{Solar}}$: Heating due to absorption of solar radiation.

$\mathbf{P_{atm}}$ : Heating by absorbing atmospheric radiation.

$\mathbf{P_{RC}}$ : Heat exchange via RC.

$\mathbf{P_{net,Cooling}}$ : The net cooling power.

**q**: Ratio of solar radiation power divided by the radiative power of a blackbody at 300 K in the 8–13 μm spectral range.

$\mathbf{\bar{R}_{solar}}$: Average solar reflectance.

$\mathbf{r_{RC}}$ : Radius of the RC.

**RF**: Radiative forcing.

$\mathbf{T_{amb}}$ : Ambient temperature.

$\mathbf{T_{RC}}$ : Temperature of the radiative cooler.

$\mathbf{T_g}$ : Glass transition temperature.

$\mathbf{T_{g,eff}}$: Effective glass transition temperature.

**τ (λ)**: Spectral atmospheric transmittance in the normal direction.

$\boldsymbol{\psi_d}$**:** Maximum possible deviation from the zenith, occurring when radiation is emitted from the edge of the RC material structure.

$\boldsymbol{\theta_s}$: Supplementary angle to the rim angle.

# Chapter 1

## 1. Introduction

### 1.1. Background and context of the research

Global warming is an unprecedented challenge that poses significant risks to our planet's environmental equilibrium and the well-being of its inhabitants. Driven primarily by the accumulation of greenhouse gases, such as $CO_2$, $CH_4$, and atmospheric $H_2O$, global warming is manifesting in the form of heatwaves, rising sea levels, increased flooding, and severe infrastructure damage [7][8][9][10]. One contributing factor to the predicament is the surging demand for cooling, driven by rising temperatures and the need for comfortable indoor environments. Traditional cooling systems are energy-intensive and, unfortunately, release substantial amounts of pollutants, exacerbating the environmental crisis. In fact, an alarming statistic reveals that approximately 40% of primary energy consumption is attributed to the operation of heating, ventilation, and air conditioning (HVAC) systems within buildings [11][12]. This statistic underscores the urgency to explore alternative cooling methods that can substantially reduce both energy consumption and emissions in the building sector. Addressing this critical modern-day problem requires innovative solutions that not only reduce greenhouse gas emissions but also mitigate the adverse effects of escalating temperatures.

One promising avenue of research lies in passive cooling technologies, which hold the potential to address the aforementioned issues effectively. Passive cooling systems are characterized by their

ability to achieve thermal comfort without reliance on energy-intensive mechanisms. In particular, radiative cooling (RC) technology has emerged as an innovative and sustainable solution that not only caters to the growing demand for cooling but also contributes to global environmental goals in several ways [8][12][13][14][15][16].

RC technology is predicated on the principle of radiating excess heat energy to outer space, thereby utilizing the frigid expanse of space as a natural heat sink. This principal hinges on the atmospheric characteristics of Earth, with specific emphasis on the phenomenon known as the atmospheric window. Within the wavelength range of 8–13 μm, this atmospheric window is characterized by minimal absorption of thermal radiation and is highly transparent to radiative heat transfer [17][18]. Importantly, this wavelength range corresponds with the peak emissions of thermal radiation from terrestrial objects at ambient temperatures. Thus, the large temperature gradient between the Earth's surface (around 300 K) and outer space (approximately 2.7 K) provides an exceptional opportunity for harnessing radiative cooling. In practice, any sky-facing object with high emissivity in the atmospheric window can effectively emit radiative heat to outer space, resulting in a substantial cooling effect [19][20]. Not only does RC technology offer a novel approach to meeting cooling demands, but it also plays a crucial role in mitigating urban heat islands, which, in turn, reduces the need for additional cooling. Furthermore, RC technology's unique ability to emit heat energy directly into outer space contributes to a reduction in global warming by decreasing the net radiative forcing [21][22][23][24].

The interplay between global warming, escalating energy demands for cooling, and the promising capabilities of RC technology provides the overarching context for this research. The pursuit of sustainable cooling solutions, underpinned by RC technology, is imperative in the ongoing battle to address global warming while ensuring a habitable and environmentally responsible future.

## 1.2. Statement of the problem

RC technology offers a promising approach to address the increasing energy demands for in a verity of cooling applications. In RC technology, sky-facing structures with high emissivity within the atmospheric transparency window can efficiently radiate thermal energy to outer space, providing cooling benefits [2]. While efficient RC material structures have been developed for

various applications, a critical challenge hinders their widespread adoption in systems with limited available space. This research encompasses different interrelated components, each addressing a distinct challenge in advancing RC technology.

In the realm of RC technologies, a critical research gap exists in the identification and development of novel materials and designs with enhanced RC properties. While commendable progress has been made in introducing efficient RC material structures for various applications, there is still ample room for investigation into material structures that not only exhibit high emissivity for effective thermal radiation but also possess high solar reflectivity. This dual consideration becomes particularly crucial for applications operating during daylight hours. The development of materials with a balance between high emissivity for efficient RC and high reflectivity for solar rejection is imperative for the continuous integration of RC technologies into applications that operate continuously, both day and night.

Exploring material structures with the capability to effectively manage solar radiation during daylight hours will contribute to the overall efficiency and applicability of RC systems. This involves not only identifying materials with the desired optical properties but also designing structures that can selectively control the absorption and reflection of solar energy.

Closing this research gap is vital for advancing the practicality and versatility of RC technologies. The investigation into material structures with high solar reflectivity, coupled with enhanced RC properties, will not only broaden the scope of applications for RC systems but also address the challenges associated with continuous operation in diverse environmental conditions.

Moreover, while significant progress has been made in the development and implementation of RC technologies for various applications, a critical research gap exists in the design and optimization of RC material structures for spaces with limited surface area. Current literature acknowledges the challenge posed by constrained sky-facing areas in impeding the widespread adoption of RC technologies for environments with limited surface availability [19]. However, existing research has predominantly focused on enhancing the RC performance from the top sky-facing surfaces of objects, neglecting the potential contributions from the bottom surfaces.

To date, the majority of RC material structures have been designed with insulation on the bottom surfaces, assuming limited cooling potential due to the exchange of thermal radiation with

surrounding surfaces. This approach limits the overall efficiency of RC systems, as the bottom surfaces could also play a significant role in radiating thermal energy to outer space. Therefore, a critical research gap exists in the exploration and development of efficient RC material structures capable of simultaneous RC from both the top and bottom surfaces in space-restricted environments.

Addressing this research gap is essential for the advancement of RC technology in spaces where the optimization of sky-facing area becomes a crucial factor. Despite efforts to enhance the cooling performance of RC designs, there is still ample room for innovation in developing material structures that can effectively exploit both sky-facing surfaces for RC in environments with limited surface area. Closing this research gap will not only contribute to the broader adoption of RC technologies in space-restricted environments but also pave the way for more energy-efficient and sustainable cooling solutions in constrained spaces.

## 1.3. Objectives of the research

The high-level objectives of this research are to develop and evaluate novel configurations of micro and nano-structured materials with controlled radiative properties for RC applications. To achieve that, the following objectives should be fulfilled:

***Objective 1:*** *To explore the environmental impact of RC materials in geoengineering applications and Life Cycle Assessment Approaches for this technology.*

This objective seeks to assess the global warming potential (GWP) associated with the use of RC materials, as opposed to traditional surfaces, through life cycle assessment (LCA) methods. By comparing the GWP of RC materials reported in the literature, with that of common construction materials such as white cement paste, road asphalt, concrete, and grey cement, as well as roofing materials like shingles, ceramic roofing tiles, and PVC, this study evaluates the environmental benefits of RC. Additionally, the GWP of natural surfaces, including forests and oceans, is analyzed to offer a broader perspective. To deepen the analysis, idealized surfaces—such as a perfect RC, perfect reflector, and blackbody—are also included to contextualize the environmental

impacts. Furthermore, the potential impact of covering 1% of Earth's surface with RC materials on terrestrial radiative forcing (RF) is explored, providing insights into how surface modifications might influence RF and contribute to climate mitigation strategies. The results aim to inform decision-making in both geoengineering and land-use planning by showcasing the benefits of RC in reducing GWP.

***Objective 2:*** *To perform numerical simulations to investigate the effects of placing reflective surfaces under a RC material structure.*

The aim of this objective is to understand the effects of using underside reflectors on radiative cooling properties of RC material structures. Optical simulations based on Monte Carlo Ray Tracing (MCRT) method are carried out to investigate the effects of the geometric properties of the parabolic reflectors including aperture surface area, focal length, and height on the RC performance. The effects of changing the heat convective transfer coefficient, $h$, the incident solar radiation, $\alpha_{\text{Solar}}$, the atmospheric temperature, $T_{atm}$, and the average emittance over the atmospheric window, $\varepsilon_{AW}$, on the performance of the RC are also investigated.

***Objective 3:*** *To design and experimentally investigate a porous Passive Daytime Radiative Cooler (PDRC) system with an optimized and controlled pore size distribution of micro and nano sizes using phase inversion technique to demonstrate high solar reflectivity as well as high emissivity in Long Wavelength Infrared (LWIR) wavelengths.*

This objective aims to find a correlation between the fabrication parameters of porous material structures and their optical behavior in terms of solar reflectivity and LWIR emissivity. In this objective, phase inversion technique is used to fabricate porous coatings. Poly (vinylidene fluoride-co-hexafluoropropylene) (PVDF-HFP) is a low-cost polymeric material with ideal intrinsic properties suitable for RC applications which is utilized as the base material in this proposed study. The effects of parameters including the polymer; solvent; nonsolvent mass ration, nonsolvent type and temperature on the geometrical aspects of the porous coatings and their optical properties are investigated.

***Objective 4:*** *To demonstrate a proof-of-concept of the developed PDRC material structure in a practical application and to evaluate its performance in an outdoor setup.*

In this objective an experimental setup will be designed to test the performance of the developed PDRC material structure. The rooftop measurement setup includes a chamber of a polystyrene foam covered with a layer of aluminum foil to reduce the effects of convection/conduction and solar radiation. The RC samples employing an underside reflector (parabolic and flat reflectors) are placed inside the insulated chamber and a transparent PE film is used on top to seal the apparatus from wind and convection/conduction. A feedback-controlled heater is attached to the sample to maintain the RC samples at an ambient temperature for cooling power measurements. Thermocouples will be used to measure the temperature directly below the sample as well as the ambient air temperature around the sample. A relative humidity (*RH*) data logger is used to measure and record the relative air humidity. The hemispherical solar irradiance is measured using a pyranometer connected to a computer. For the sub-ambient temperature measurements, the heater switches off and the temperature of the air and RC sample and solar irradiance are recorded over a period of time. The apparatus is placed on top of a roof.

## 1.4. Thesis Outline

This thesis embarks on a comprehensive exploration of RC technology, addressing the pressing challenges related to cooling in applications with limited space. This research is structured into distinct components, each contributing to the advancement of RC technology.

In **Chapter 2 (Literature review),** the focus is on providing an overview of RC technology, outlining its significance in the context of sustainable building practices. The chapter will start with an introduction to the concept of RC and its potential to mitigate the environmental impacts of traditional cooling methods. It will also include a comprehensive literature review on studies investigating RC technology, highlighting key findings and gaps in research.

**Chapter 3 (Environmental implications of RC technologies)** will delve into the environmental implications associated with integrating RC technologies into buildings. It will begin by discussing

the methodologies and frameworks used in assessing the environmental impacts of RC technologies within the built environment. The chapter will then examine key environmental indicators such as energy consumption and greenhouse gas emissions, aiming to quantify the sustainability benefits of incorporating RC technologies. Furthermore, it will explore the complexities of evaluating the GWP of RC technologies, emphasizing their direct effects on radiative forcing.

**Chapter 4 (Utilizing underside reflectors in RC technology)** focuses on the utilization of underside reflectors in RC technology to enhance cooling efficiency. It starts by explaining the conventional emphasis on optimizing RC from top sky-facing surfaces and the challenges associated with cooling contributions from non-sky-faced sides. The research methodology for designing and implementing innovative RC material structures incorporating underside reflectors will be outlined, aiming to redirect thermal radiation and enable dual-sided RC. This chapter will provide insights into the practical implications and potential applications of this approach, especially in settings characterized by limited space.

**Chapter 5 (Enhancing RC material properties for improved cooling)** delves into the properties of RC materials and strategies for enhancing their cooling potential. It will discuss the significance of material choice and optical characteristics in achieving efficient RC. The research methodology for exploring and developing materials with optimized optical properties will be outlined, with a focus on maximizing cooling potential through the optimization of emissivity, spectral properties, and thermal radiation characteristics. This chapter will contribute to advancing the understanding of RC material science and its implications for sustainable cooling solutions.

**Chapter 6 (Experimental setup and testing performance)** presents the design of an outdoor experimental setup tailored to evaluate the performance of the developed RC material structure under real-world conditions. This section provides a detailed description of the experimental setup, including the selection of the testing location, arrangement of instrumentation, and measurement protocols. The chapter emphasizes the importance of outdoor testing to assess the RC material structure's performance accurately in varying environmental conditions, including solar radiation, ambient temperature, humidity, and wind speed. Additionally, this chapter outlines methodologies for evaluating the RC material structure's effectiveness in passive cooling applications and its potential for water harvesting. Through comprehensive testing protocols, this section aims to

provide valuable insights into the practical applicability and performance of RC technology in real-world scenarios.

**Chapter 7 (Conclusion and future work)** summarizes the main research components, their contributions, and the overarching challenge addressed. It discusses innovative solutions proposed for efficient cooling and broader implications for energy consumption reduction and greenhouse gas mitigation. It also suggests future research directions and applications of RC technology.

# Chapter 2

## 2. Radiative cooling technology

### 2.1. Introduction

Radiative coolers (RCs) function by radiating thermal energy to outer space. There is a substantial difference between the temperature of terrestrial objects on Earth (~ 300 K) and outer space (~2 K). To harness this temperature difference, there must be a free exchange of radiation between terrestrial objects and outer space. Fortunately, the Earth's atmosphere is highly transparent over the atmospheric window with wavelengths ranging from 8 to 13 μm [24][25][26][27]. As depicted in Figure 2.1, this wavelength range aligns with the peak emissions of thermal radiation from terrestrial objects at typical ambient temperatures. Consequently, the significant temperature differential between the Earth's surface (approximately 300 K) and outer space (around 2.7 K) presents a remarkable opportunity for effective RC [28].

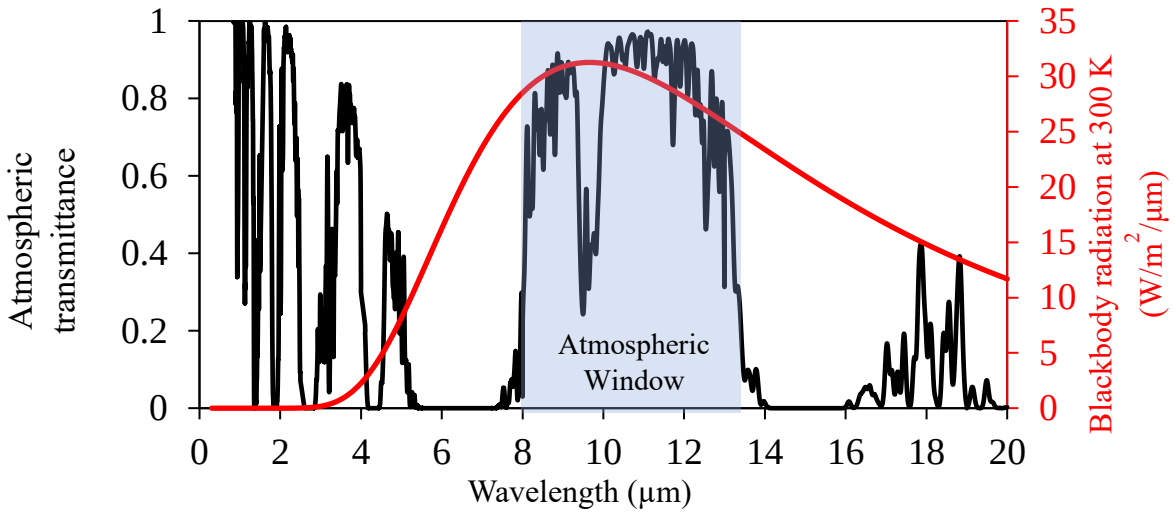


*Figure 2.1. Atmospheric spectral transmittance obtained from ATRAN and the blackbody spectral radiation at 300 K.*

## 2.2. Fundamental principles of radiative cooling

The net cooling power of a daytime radiative cooler can be affected by four main heat exchange processes [29][30]: i) heat exchange via RC ($P_{RC}$), ii) heating by absorbing atmospheric radiation ($P_{atm}$), iii) heat exchange with the surrounding environment via convection and conduction ($P_{Nonrad.}$), and iv) heating due to absorption of solar radiation ($P_{Solar}$). Note that $P_{Nonrad}$ is considered to be positive when heat is transferred from the surroundings to the RC system, which is the case for sub-ambient cooling. These heat exchange processes are illustrated in Figure 2.2.

The theoretical models used to define these thermal exchange factors are provided in the literature [22][31][1][2][32][19][20][33]. To increase the cooling power of a radiative cooler, the effect of the three parameters $P_{atm}$, $P_{Nonrad}$, and $P_{Solar}$ should be minimized to ensure the radiated output power exceeds the net absorbed power. To achieve this, first, a RC material structure should have a selective emitter having maximal emissivity over the spectral range form 8-13 μm (to increase $P_{RC}$) while having low emissivity in other wavelength regions (to decrease $P_{atm}$). Secondly, if operating under sunlight RC material structures should be highly reflective to solar radiation (to reduce $P_{Solar}$). Finally, to minimize non-radiative heat gains from the surrounding environment ($P_{Nonrad}$), the radiative cooler can be sheltered by encapsulating it in an air/vacuum media or by

using convection/conduction shields. More details about these heat exchange processes are discussed in the following sections.

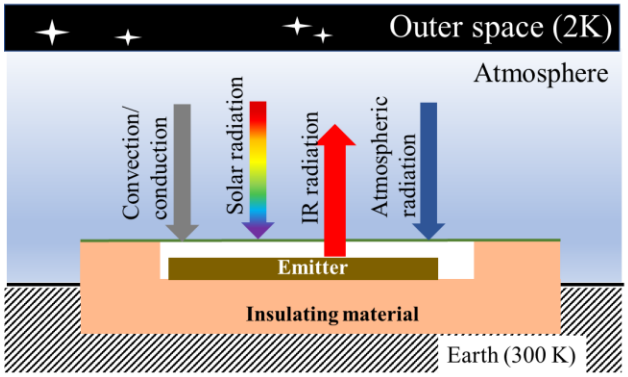


*Figure 2.2. Schematic of a RC panel showing its four main heat exchange processes.*

### *2.2.1. Convective heat exchange with the surrounding environment*

If the operating temperature of the radiative cooler is higher than the ambient temperature, then an RC material structure loses heat to its surroundings and $P_{Nonrad}$ is negative, which increases the overall cooling power that can be achieved. However, when cooling to sub-ambient temperatures, $P_{Nonrad}$ is positive and reduces the net cooling power [2]. For sub-ambient cooling approaches, the convective heat transfer is typically responsible for the greatest loss in cooling power. There are two major solutions for reducing unwanted effects of convective heat transfer during sub-ambient RC. The first solution is to encapsulate the radiator with a medium that has low thermal conductivity such as air or vacuum and surround this medium with insulative structures to suppress convective heat transfer [34][35]. The second solution, which is more robust and scalable, is to use an infrared-transparent cover or a wind shield to restrict the ambient airflow across the radiator [36][37]. Generally, convection or wind covers are utilized to suppress the non-radiative heat exchange. For example, low-/high-density polyethylene (L/H-DPE), pigmented polyethylene (PE) foils, zinc selenide (ZnSe), zinc sulfide (ZnS), and CdS, Si, or Ge windows can be placed above the radiator due to their high transmittance within the atmospheric window [38][1]. PE films with their high transparency in the atmospheric region of 8–13 μm are considered as a cost-effective candidate with excellent results for insulating applications. Leroy *et al.* [39] designed solar reflecting, IR transparent, low thermal conductivity films using PE aerogels (PEAs) that can be

integrated with LWIR radiators to form a high-performance sub ambient RC design. Using this design in an experimental setup they reported a daytime ambient temperature cooling power of 96 $W \cdot m^{-2}$ and passive cooling up to 13˚C below ambient temperature at noon time. Another material suggested as a convection cover with high IR transparency and mechanical strength is zinc sulphide (ZnS). Bathgate *et al*. [40] measured the average 8-13 μm transmittance of ZnS and reported a value of 64% for a 4 mm thick film of this material. Although zinc sulphide has better durability than PE, its high manufacturing costs present a challenge and its IR transmittance (64% for a 4 mm thick film) is lower than that of a 100 μm thick PE film, which has an IR transmittance of 73%. ZnSe is another candidate to be used as a convection shield, which has been reported by Chen *et al*. [38]. In this study a vacuum chamber equipped with a double-side anti-reflection coated ZnSe window is used to minimize parasitic heat losses caused by the air conduction and convection. Generally, the thin layers of PE ages fast due to the adverse effects of ultraviolet radiation. On the other hand, although ZnS and ZnSe layers possess the high strength, a low solar transmissivity and high costs restrict their utilization in building applications [19]. Liu *et al*. [41] thoroughly reviewed the available wind cover materials and reported that only thin low-density polyethylene (LDPE) and high-density polyethylene (HDPE) films can be efficiently implemented for daytime RC. ZnS and ZnSe layers can also be used to protect the vacuum chambers from non-radiative heat exchange. They also collected non-radiative heat exchange coefficients of structures with and without the wind cover reported in the RC studies.

### *2.2.2. Heating due to the solar irradiance*

The total solar radiation that reaches the top of the Earth's atmosphere, known as the solar constant, has a value of 1,354 $W \cdot m^{-2}$. However, parts of the insolation are reflected, transmitted, or absorbed and reradiated while passing through the Earth's atmosphere and the amount that reaches the planet's surface varies from 0 to about 1050 $W \cdot m^{-2}$. On average about half of the solar energy incident onto the top of the atmosphere reaches Earth's surface, of which 21% is received as direct radiation and about 29% is received as scattered or diffuse radiation. For daytime RC applications, it is important to reflect both the diffuse and direct parts of the solar irradiance. For instance, a RC module with a solar absorption of 5-10%, under a solar irradiance of 800 $W \cdot m^{-2}$, absorbs 40–80 $W \cdot m^{-2}$, approaching or even exceeding the output cooling potential of the radiator [2]. To minimize the adverse effect of solar radiation different techniques can be utilized such as using solar

reflective structures that are transparent for thermal radiation or structures that can reflect solar radiation while providing LWIR emissivity. Furthermore, sunshades can also be utilized to confine the solar flux and decrease the absorption of the direct solar irradiance. For example, Chen *et al.* [38] used a combination of a sunshade and a mirror-cone in a RC design to mitigate the effects of the direct and indirect solar irradiance onto the emitter. This design is used to ensure that the selective emitter is exposed to only diffuse sunlight when the structure is under the direct sunlight. The cone also restricts the high-intensity low-angle incoming atmospheric radiation by confining the angular range of the apparatus to directions close to the zenith where the sky is most transparent.

### *2.2.3. The effects of atmospheric conditions*

The atmosphere is comprised of many constituents including carbon dioxide, water vapor, ozone, nitrogen oxides and hydrocarbons, which cause significant absorption bands in the IR wavelength range from 3 - 50 μm. To evaluate the performance of RC material structures it is crucial to use an accurate radiative model to calculate the spectral and directional emittance of the sky under different conditions. Such models take into consideration the temperature, atmospheric water vapor distribution and other meteorological parameters, such as dew point temperatures. Specific tools such as a pyrgeometer or modified infrared thermometer can also be used to measure the spectral and directional emittance of the sky [1][2][38]. Comprehensive reviews on different correlations for infrared atmospheric radiation have been provided in the literature [22][2][32][11]. The amount of water content in the atmosphere is a crucial factor in determining the transparency of the sky in the atmospheric window, and this must be taken into consideration when designing RC material structures. Figure 2.3 shows the modeled atmospheric transmittance for two different locations in Australia during summer (January 2015), Perth and Brisbane, which had different ambient temperatures and relative humidity (*RH*) values [1]. The strong effects of *RH* on atmospheric transparency are apparent when comparing the transmittance plots in Figure 2.3, which differ significantly despite the fact that the temperatures used in the model for Perth and Brisbane are comparable. Similarly, the existence of clouds in the sky promotes the incoming infrared atmospheric radiation compared to clear sky conditions. This happens as clouds close the transparency of the sky in the atmospheric window region [32].

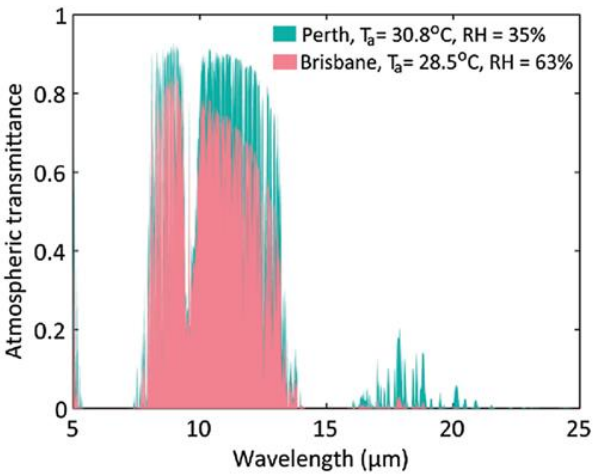


*Figure 2.3. Modeled atmospheric transmittance profile for two locations of Perth and Brisbane with different atmospheric conditions. Reproduced under the terms of the Creative Commons License CC BY 4.0.* [1] *Copyright 2016, The Authors, published by WILEY-VCH Verlag GmbH & Co.*

### *2.2.4. Spectral selectivity of the radiators*

According to the target cooling temperature of the RC material structures relative to the ambient temperature, the applications of this technology are dived into two categories of below-ambient or above-ambient. In general, the desired spectral emittance profile of the radiators in a RC system is influenced by the target temperature to be below ambient or above-ambient after cooling. In below-ambient cooling applications, when the ambient temperature ($T_{amb}$) is higher than the temperature of the radiator ($T_{RC}$), $T_{RC} < T_{amb}$, thermal radiation outside the atmospheric window region, 8-13 μm, from the ambient heats up the radiator which causes a reduction in cooling power. Therefore, a spectral selective radiator with an emissivity close to one over the atmospheric window and zero emissivity outside this spectral region can reduce this undesirable absorption of thermal radiation from the ambient and maximize cooling power.

On the contrary, for above-ambient cooling applications, an ideal spectrally broadband radiator should have an emittance close to one throughout the whole IR spectrum, and small absorptance in the solar spectrum for daytime cooling. The reason is that when $T_{RC}$ is higher than $T_{amb}$, $T_{RC} > T_{amb}$, having a high emissivity from 3 μm to ∞ and thermal radiation outside the atmospheric window would become beneficial to increase the thermal heat radiated from the radiator to the ambient, thus reaching a higher achievable net cooling power. To summarize, a selective radiative

cooler is beneficial for below-ambient cooling, while a broadband radiative cooler is needed for above-ambient cooling applications [2][42].

## 2.3. Radiative cooling materials and structures

According to the operating time, RC techniques can be classified into two categories of daytime (diurnal) RC and nighttime (nocturnal) RC [18]. The applications of nocturnal RC are well developed, and several studies have been conducted based on this category of RC technique [2][43][44][45]. To date, efficient nocturnal radiative coolers have been introduced and implemented in a wide variety of applications such as energy-efficient buildings [14], photovoltaic-thermal collectors [2][46], solar collector walls [47], and evaporative cooling systems [48][3]. However, there is still a huge challenge in designing highly efficient diurnal radiative coolers due to the intense effect of the solar radiation which is greater than the radiation emitted by the radiative cooler. Effective diurnal RC depends on using materials that are highly reflective towards solar radiation, and highly emissive in the atmospheric window. To date, numerous kinds of RC material structures have been either computationally or experimentally investigated.

### *2.3.1. Polymeric structures*

Polymer-based structures have been utilized in different daytime and nighttime cooling systems. Initially, polymer materials including polyvinyl chloride (PVC), polyvinyl fluoride (PVF/Tedler) and polymethyl pentene (TPX) were utilized as radiators in RC material structures. Granqvist *et al*. [49] conducted experiments to compare these polymers (a l00 μm-thick PVC film, a 12.5 μm-thick PVF/Tedler film, and a 340 μm-thick TPX film) and concluded that although these polymeric films exhibit a high emittance over the spectral range from 8-13 μm, they are strongly absorbing over a broad range outside the atmospheric window which increases $P_a$ and reduces their cooling potential.

In recent studies, other types of polymers such as polyvinyl difluoride (PVDF) [50][51], polymethyl methacrylate (PMMA) [52], polydimethylsiloxane (PDMS) [53][54][55][56][57], and polyethylene terephthalate (PET) [58] [59] were employed for RC technology. Hu *et al*. [59] covered a layer of PE terephthalate (PET) on a Ti-based solar selective absorber to design a

combined diurnal solar heating and nocturnal RC system acting as a solar heating system in the daytime and as a RC system in the nighttime. In this study, a 30 μm-thick layer of PET with high emissivity in the atmospheric window was covered on the Ti-based solar absorbing coating to give a nocturnal RC ability to the solar heating system. Two circulation loops with flow rates of about 0.016 kg. $s^{-1}$ and 0.012 kg. $s^{-1}$ were applied for the diurnal collector testing mode (solar heating system) and for the nocturnal collector testing mode (RC system), respectively. They performed different experiments with different weather conditions by changing the inlet water temperature of the collector to assess the thermal performance of the two collectors at both daytime and nighttime conditions. When tested on a clear night this nocturnal collector achieved a net RC power of 50.3 $W \cdot m^{-2}$. Recently, S.Y.Jeong *et al*. [53] applied a naturally-inspired thermoregulatory prismatic structure to a PDMS polymer with high emissivity within the atmospheric window to create a selective thermal emitter. Their results showed an average emissivity within the 8–13 μm wavelength range of 0.98 and an average solar reflectivity in the visible and near-infrared spectrum of 0.95. Generally, other advantages of polymer-based RC structures are their low-cost and scalability for mass-production and commercial applications.

### *2.3.2. Pigmented paints*

At the earlier stages of RC technology, researchers also used pigmented white paints to achieve RC [2]. For example, Orel et. al. [60] compared two white pigmented RC material structures, $TiO_2/BaSO_4$ and $TiO_2$/ZnS, and concluded that RC can be enhanced to a greater extent through the addition of $BaSO_4$ rather than ZnS. The reason is that the absorption of the $TiO_2/BaSO_4$ paint is high in the atmospheric window due to the vibrational stretching modes of $SO_4$ within $BaSO_4$ over the spectral range from 8-13 μm. On the contrary, $TiO_2$/ZnS samples displayed higher absorptance in the spectral range outside of the atmospheric window. In another study on pigmented paints, Andretta *et al*. [61] designed a material structure comprised of an IR transparent PE film doped with titanium dioxide ($TiO_2$) white pigments and carbon black particles as a daytime radiative cooler. Although the pigmented PE films showed a high transparency in the IR wavelengths, these structures did not achieve high reflectivity towards solar radiation. In another study, Nilsson *et al*. [62] employed pigmented PE foils with different pigments of ZnS, ZnSe, $TiO_2$, $ZrO_2$ and ZnO. A 400 μm thick PE film pigmented with 15% ZnS exhibited a solar reflectivity of 84.9%. Recently, Chae *et al*. [63] fabricated a scalable and paint-format RC coating

which consisted of $Al_2O_3$ and $SiO_2$ microparticles filtered in dipenta-erythritol penta-/hexa-acrylate (DPHA) and acrylate binder (acrylate). This RC paint displayed a high solar reflectivity of 94% and an emissivity of 93.5% in the atmospheric transparency window, resulting in a cooling power of about 100 $W \cdot m^{-2}$ and an average temperature drop of −7.9 ˚C and −5.1 ˚C for surface cooling and water cooling, respectively.

### *2.3.3. Multilayered and photonic structures*

With recent progress on the design and fabrication of advanced photonic structures, they have been widely developed for RC, especially sub-ambient diurnal radiation cooling [33][64][65][66][4][67]. 1D photonic crystals are multilayered structures consisting of alternating layers of materials with different refractive indices that can be utilized as radiators and solar reflectors for RC applications [1]. Raman *et al*. [4] for the first time experimentally developed a RC material structure using a multilayer film for sub-ambient diurnal cooling under direct solar irradiance. In this work, seven alternating layers of hafnium dioxide ($HfO_2$) and $SiO_2$ with different thicknesses deposited on an Al-coated Si wafer formed a RC material structure that reflected 97% of the solar irradiance and emitted thermal radiation over the spectral region from 8-13 μm. The top three layers, which were relatively thick, mainly contributed to the IR emissivity and the four thinner bottom layers served as a solar reflector. Outdoor experiments resulted in a temperature reduction of 5 ˚C below the ambient temperature with a net cooling power of approximately 40.1 $W \cdot m^{-2}$ under the direct solar radiation. In another multilayered structure composed of $SiO_2/Si_3N_4$ layers, Ma *et al*. [66] designed a high-performance RC material structure which was highly reflective towards solar radiation and had a broadband emissivity within the atmospheric window. This photonic RC material structure displayed a temperature reduction of 8 ˚C under a hot and humid climate. Chae *et al*. [64] proposed and fabricated a multilayer structure comprised of $Al_2O_3$, $Si_3N_4$, and $SiO_2$ deposited on Ag- and Cr-coated Si substrates. By adjusting the stacking sequence and thickness of the layers, this RC material structure showed an average emissivity of 87% in the 8-13 μm spectral region.

Patterned surfaces, or a combination of patterned surfaces and multilayer films, have also been developed for efficient diurnal RC [68][69][70][71][72][73][74]. For example, Hossain *et al*. [68] utilized an anisotropic and conical-shaped metamaterial structure to achieve a highly enhanced,

and broadband infrared (IR) emission, which is selectively spanned over the entire atmospheric window. This structure consists of an array of symmetrically shaped conical metamaterial pillars comprising alternating layers of aluminum (Al) and germanium (Ge) and showed a near blackbody emissivity in the atmospheric window. Zhang *et al*. [75] also designed a biologically inspired photonic structure consisting of a micropyramid-arrayed polymer matrix (PDMS) with random ceramic particles (e.g., $Al_2O_3$, $TiO_2$, and ZnO). This 500-μm-thick bioinspired RC material structure with embedded $Al_2O_3$ nanoparticles reflected ~95% of solar irradiance and exhibited an infrared emissivity of 96% with an effective cooling power of ~90.8 $W \cdot m^{-2}$ and a temperature decrease of up to 5.1 ˚C under direct sunlight.

### *2.3.4. Metamaterials*

Utilizing of metamaterials in RC has become feasible due to the vast development of technology in nanofabrication and detailed structures. Integrating metamaterials into RC material structures presents a promising avenue for enhancing the performance and efficiency in this technology. Metamaterials, engineered to exhibit unique electromagnetic properties not found in natural materials, offer unprecedented control over light-matter interactions, particularly in manipulating thermal radiation. By strategically designing metamaterial architectures at the micro and nano scales, it becomes feasible to tailor the emissivity and reflectivity properties of surfaces with precision. This capability enables the creation of surfaces that can effectively reflect sunlight while simultaneously emitting thermal radiation in the atmospheric transparency window, facilitating efficient passive cooling. Moreover, metamaterials can be designed to exhibit selective spectral properties, enabling them to emit thermal radiation at specific wavelengths while suppressing emission at others, thus optimizing the cooling process. Therefore, a variety of nanophotonic configurations, including but not limited to metal–dielectric multilayer conical pillar arrays [68], metal–dielectric multilayered nonconical column arrays [76], metal-loaded dielectric resonator metasurfaces [77], metal–dielectric–metal resonators [78][79][80], multilayered pyramidal nanostructures [71],[73] metafabric, and other metastructures [81][82][83], exhibit notable reflectivity across the solar spectrum and heightened emissivity within the atmospheric window.

In a study proposed by Hossain *et al*. a highly efficient RC using a metal–dielectric multilayer conical metamaterial emitter. This emitter consists of an array of symmetrically shaped conical

metamaterial (CMM) pillars. CMM pillars are composed of 14 alternating layers of 30 nm thick of Al and 110 nm Ge, with gradually decreasing the diameters of the layers from bottom to top, on an Al film coated Si substrate. The designed emitter exhibits an excellent spectral selectivity in the wavelength range of 8 to 13 μm, with peak emission of 90%. However, the designed emitter needs to be integrated with solar reflective structures for daytime applications. In another study reported by Sun *et al*. [80] a metasurface based on Al-doped zinc oxide (AZO) transparent conducting oxides (TCOs) is designed and investigated. This sub-micrometer thicknessed metasurface is comprised of a stack of three layers including the metal back-reflector, the dielectric spacer layer, and the TCOs layer achieving a high absorption of electromagnetic radiation in the mid-infrared range resulting in a thermal emissivity of 79% and a solar absorptance of 16%.

However, challenges regarding the broad applications of metamaterial-based structures in RC lies in optimizing the detailed design and complicated fabrication processes to achieve the desired spectral properties. Also, maintaining durability and stability of the metamaterial structures over time, especially in outdoor environments where they may be exposed to varying weather conditions and environmental stresses, is another constraint in utilizing this type of structures.

### *2.3.5. Porous structures*

Porous RC material structures demonstrate a promising path in the pursuit of passive thermal management solutions. These structures typically comprise networks of size-controlled voids and pores within a solid material, designed to offer efficient radiative heat exchange with the surrounding environment. By leveraging the principles of optimizing LWIR emission and solar irradiance reflection, porous RC material structures can effectively boost RC efficiency and hold immense potential in addressing the challenges in implementation of before-mentioned structures. This combination of properties enables porous RC material structures to achieve substantial cooling effects, even under direct sunlight and in warm ambient conditions. Moreover, their scalability, durability, cost efficiency, and compatibility with various materials make them suitable for diverse applications, ranging from building rooftops and urban heat island mitigation to electronics cooling and thermal comfort enhancement in clothing and textiles. Porous RC material structures can be constructed from a diversity of materials, including polymers, ceramics, metals,

and composites. The choice of material can influence factors such as mechanical strength, durability, and compatibility with specific applications.

When polymers transitions from a dense solid structure to a porous one their physical and thermal properties change significantly. These changes directly impact performance in RC applications. The presence of nano- and micro-pores decreases the bulk material content per unit volume, as the pores are primarily filled with air. The effective specific heat capacity reduces because air has a much lower specific heat than the polymer. The density significantly decreases too as the pores replace portions of the solid material. It reduces the overall weight of the material, which is advantageous for lightweight RC systems. Also, porosity lowers thermal conductivity because air trapped in the pores has a much lower conductivity than the polymer. Lower thermal conductivity minimizes heat transfer through conduction, enhancing insulation properties and enabling the material to maintain a cooler surface temperature. However, porosity reduces mechanical strength due to the decrease in solid material content. While the material may become less robust, it is still suitable for RC applications where mechanical stresses are minimal. This can be mitigated by layering or reinforcing the material.

In many studies polymeric structures have been designed in the form of porous configurations for daytime RC applications. For example, Mandal *et al*. [50] investigated hierarchically porous poly (vinylidene fluoride-co-hexafluoropropene) [P(VdF-HFP)] coatings for passive daytime RC. P(VdF-HFP) possesses a negligible extinction coefficient over the entire solar spectrum, and has multiple extinction peaks within the atmospheric window, over 8-13 μm, which makes it a suitable material for daytime RC applications. They utilized a phase inversion–based process to fabricate hierarchically porous polymer coatings. As this fabrication technique is done at room-temperature, and is solution based, the porous polymer coatings can be applied by conventional approaches such as painting which makes it a simple, scalable, and inexpensive passive cooling approach. It has been shown that P(VdF-HFP) with hierarchically porous structures comprising micro- and nano-pores with 50% porosity and 300 μm thickness have a high solar reflection of 0.96 and LWIR emissivity of 0.97. The high LWIR emissivity of their RC material structure is attributed to the open, porous surface and the effective optical properties of the nano pores in the hierarchically porous P(VdF-HFP) coatings. They declared that a combination of these two features resulted in a gradual transition of the refractive index across polymer-air boundaries, which increased the emissivity of the structure. Similarly, Wang *et al*. [52] reported on hierarchically porous PMMA

films with a micropore array combined with random nanopores for highly efficient day- and nighttime passive RC. In this study, they experimentally compared optical properties of their hierarchical porous structure with three other types of PMMA films: nanoporous PMMA, microporous PMMA and pristine PMMA. They concluded that the hierarchical porous film shows the highest average solar reflectance. This hierarchically porous PMMA structure, with 60% porosity and 160 μm thickness, exhibited a high solar reflection of 95% and an excellent LWIR emissivity of 98%. In another survey, Zhou *et al*. [84] investigated a nanoporous polymer matrix composite (PMC) as a RC material structure. In this study they developed a PMC structure comprising nanoporous PE as the polymer matrix and randomly distributed silicon dioxide ($SiO_2$) particles as the fillers. PE is intrinsically transparent for both the solar and LWIR regions, and they made the PE reflective towards solar radiation by introducing air pores in nanoscale sizes inside the PE matrix to scatter incident sunlight. $SiO_2$ particles were added to modify the LWIR emissivity of the composite. The resulting nanoporous PMC coating showed a high solar reflectance of 96.2% and infrared emissivity of 90%, resulting in a sub-ambient temperature drop of 6.1 ˚C and cooling power of 85 $W.m^{-2}$ under direct sunlight. In a recent innovative study, a bilayer RC material structure comprising a bottom layer of hygroscopic hydrogel and a top layer of porous radiative polymer was designed by Feng *et al*. [85]. In this design, the bottom layer, a Li-PAAm hydrogel, dissipates heat through water evaporation at high temperature and restores itself by absorbing the surrounding moisture when the temperature decreases. The top layer, a porous P(VdF-HFP), reflects the solar irradiance while emitting LWIR radiation to outer space to achieve passive RC. When tested in an outdoor environment, a cooling power of ~150 $W{\cdot}m^{-2}$ and a sub-ambient temperature drop of ~7 ˚C under direct sunlight was achieved.

Table 2.1 provides a summary of the optical properties and cooling performance of RC material structures reported in the literature.

*Table 2.1. Optical properties and cooling performance of some of RC material structures reported in literature.*

| RC structure | LWIR emissivity (%) | Solar reflectivity (%) | Temperature reduction (˚C) | Cooling power ($W{\cdot}m^{-2}$) | Measurement location | Ref. |
|---|---|---|---|---|---|---|

| | | | | | | |
|---|---|---|---|---|---|---|
| Seven alternating layers of hafnium oxide ($HfO_2$) and $SiO_2$ deposited on Al-coated Si wafer | 65 | 97 | 5 | 40.1 | California, U.S.A. | Raman *et al.* [4] |
| Randomly distributed $SiO_2$ microparticles in a polymethylpentene (TPX) matrix | 93 | 97 | ---- | 93 | Cave Creek, Arizona | Zhai *et al*. [81] |
| 8 μm PDMS triangular array deposited on Ag coated $SiO_2$ substrate | 98 | 97 | 6.2 | 20 | Hong Kong | Jeong *et al.* [53] |
| PDMS/$SiO_2$ bilayer coated with Ag as a solar reflector | 92 | 97 | 8.2 | 127 | Pasadena, California | Kou *et al*. [86] |
| A hierarchically structured PE oxide (PEO) nanofibre-based film | 78 | 96 | 5 | 110 | Nanjing, China | Li *et al*. [87] |
| Hierarchically porous poly (vinylidene fluoride-co-hexafluoropropene) [$P(VDF\text{-}HFP)_{HP}$] coatings | 97 | 96 | 6 | 69 | Phoenix, Arizona | Mandal *et al*. [50] |
| A hierarchically porous array PMMA film | 98 | 95 | 5.5 | 85 | Shanghai, China | Wang *et al.* [52] |
| A dual-layer of a polytetrafluoroethylene (PTFE) sheet on top of a silver film | 9 | 99 | ---- | ---- | ---- | Yang *et al*. [88] |
| A hybrid membrane comprising nanoporous polyvinylidene fluoride/tetraethyl orthosilicate (PVDF/TEOS) fibers with $SiO_2$ microspheres across the surface | 96 | 97 | 6 | 61 | Shanghai, China | Wang *et al.* [89] |
| A multilayer structure of $Al_2O_3$, $Si_3N_4$, $SiO_2$, Ag and Cr deposited on a Si substrate | 87 | 5% solar absorptivity | 6.2 | 66 | Seoul, South Korea | Chae *et al*. [64] |
| Seven alternating layers of $SiO_2$ and $Si_3N_4$ on Ag-coated Si substrate | 75 | 97 | 8 | 87 | Suzhou, China | Ma *et al*. [66] |
| A double-layered RC material structure of dipentaerythritol penta-hexa-acrylate (DPHA) with $Al_2O_3$ nanoparticles (NPs) on top and a metallic Ag bottom layer | 92 | 95 | 10 | 106 | Seoul, South Korea | Liu *et al*. [90] |

| | | | | | | |
|---|---|---|---|---|---|---|
| A hybrid coating of $ZrO_2$/PDMS, zirconia ($ZrO_2$) embedded polydimethylsiloxane (PDMS) | 92 | 94 | 10.9 | 895 | Yichang, China | Zhang *et al*. [54] |
| A thin silica layer coated on porous anodic aluminum oxide | 96 | 86 | 6.1 | 178 | Seoul, South Korea | Lee *et al.* [91] |
| A self-cleaning RC multilayer film consisting of a top layer of PDMS and $SiO_2$ particles and a bottom layer of the PDMS and Al composite film | 93 | - | 2.1 | 59.04 | Shanghai Electric Power University | Zhai *et al.* [92] |
| Porous anodic aluminum oxide (AAO) membranes | 98 | 5% solar absorptivity | 2.6 | 64 | Hangzhou, China | Fu *et al.* [93] |
| A bilayer film consisting of a bottom layer of Li-PAAm hydrogel and a top porous P(VdF-HFP) layer | 96 | 96 | 7 | 150 | Yinchuan, China | Feng *et al.* [85] |
| 300 μm-thick films of cellulose (acetate) with a disordered network morphology | 95 | 93 | 7-8 | 70 | Barcelona, Spain | Jaramillo-Fernandez *et al*. [94] |
| a double-layer RC material structure with an upper layer of a fluorocarbon resin (FEVE) and a bottom layer of silver | 93 | 94 | 5 | 128 | Tianjin, China | Dong *et al*. [95] |

The bibliometric study presented in Figure 2.4 highlights the increasing global research interest in RC technologies. Figure 2.4 (a) demonstrates a steady growth in the number of published RC papers from 1948 to 2022, with a sharp rise in recent years, reflecting the growing demand for sustainable and energy-efficient cooling solutions in the context of climate change. Figure 2.4 (b) compares the focus of research on different RC configurations, including paints, photonic crystals and multilayered structures, and porous materials. The analysis reveals that porous materials have garnered the most attention due to their simplicity, cost-effectiveness, and scalability for large-scale applications. In contrast, while photonic crystals and multilayered structures are valued for their advanced optical properties, their fabrication complexity and higher costs limit their widespread adoption. Paints, though simpler, are less studied compared to porous structures, further emphasizing the practical advantages of porous materials in RC research and development.

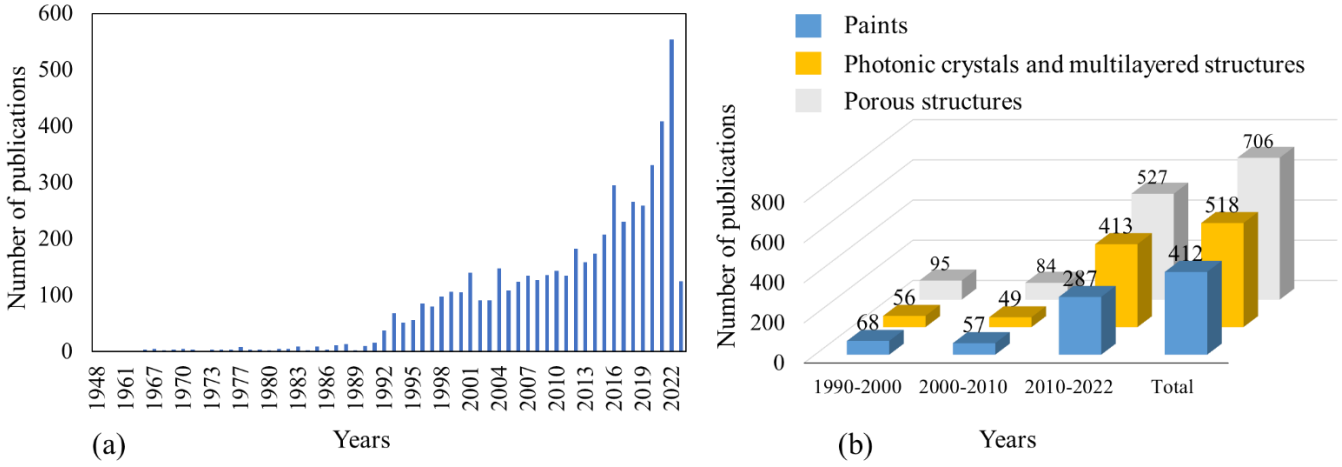


*Figure 2.4. Bibliometric study of (a) the published RC papers from 1947 to January 10, 2022; (b) Published research articles studying paints, photonic crystal and multilayered structures, and porous structures as RC configurations (Sources: www.webofscience.com and www.sciencedirect.com, Keywords: "Radiative cooling", paints, photonic crystals, multilayered, porous).*

## 2.4. Porous structure fabrication techniques

A variety of fabrication techniques can be implemented for creation of porous structures. Herein, an array of methodologies is explored to illuminate their suitability for RC applications. These techniques include diverse approaches, each offering distinct advantages and challenges.

### *2.4.1. Template-based method*

This method involves creating a porous structure by embedding a sacrificial template in the material matrix, which is later removed to leave behind a network of interconnected pores. Template-based methods are versatile and widely-used fabrication techniques for creating porous structures tailored for RC applications. These methods offer adaptable means to precisely control the porosity of the resulting films with precise pore sizes.

In the Medium Embedding-Extracting template method, a media embedding approach can be utilized to manufacture porous films. This method typically involves embedding a specialized medium within the film matrix, followed by its subsequent extraction. The process requires mixing the matrix material with the inserted medium, coating the resulting mixture onto a substrate to

form a film, and subsequently extracting the embedded medium to leave behind pores within the film structure. Wang *et al*. [52] developed a hierarchically porous PMMA film by drop casting a 200 nm $SiO_2$ nanospheres-acetone-PMMA on a monolayer template consisting of close-packed microspheres of $SiO_2$. After subtraction of the $SiO_2$ template and nanospheres with 2-5 vol% hydrofluoric acid aqueous solution, a hierarchically porous PMMA can be obtained, resulting in a high solar reflectance of 95% and a superior infrared emittance of 98%. Yang *et al*. [96] utilized styrene-butadiene-styrene block copolymer (SBS) and styrene-ethylene-propylene-styrene block copolymer (SEPS) as the soluble polymeric template and inserted medium to prepare porous polypropylene (PP) film, which can be extracted using tetrahydrofuran. The resulting porous PP showed a high solar reflectance of 97% and thermal emissivity of 67%–81%. Zhang *et al*. [97] developed an ordered porous poly (methyl methacrylate) (PMMA) film using a sacrificial template method that resulted in a material with a combination of three-dimensional (3D) ordered micropores and highly interconnected nanopores. In this study, 3 μm $SiO_2$ microspheres were self-assembled into a closely packed template using a horizontal deposition method and heat treatment. The PMMA-toluene solution was then infiltrated into the voids between the $SiO_2$ spheres, and after the toluene evaporated, the template was removed using hydrofluoric acid, creating an inverse opal PMMA (IO-PMMA) structure with ordered porous features. The heat treatment time was crucial, as extended heating (over 24 hours at 200 ˚C) allowed the microspheres to form tightly packed, interconnected pores. This ordered porous structure significantly enhanced the material's optical and thermal properties for RC. This method allowed for precise control over the film's porosity, leading to a structure with enhanced optical and thermal properties. It exhibited a prominent solar reflectance of 94%, long-wave infrared LWIR thermal emissivity of 95%, and low thermal conductivity of 0.044 $W \cdot m^{-1} \cdot K^{-1}$).

### *2.4.2. Electrospinning method*

The electrospinning method involves applying a high-voltage electrostatic field on a polymer solution to produce nanofibers with a large specific surface area and highly porous structures with diameters ranging from nanometers to micrometers. In this method an electrostatic field is utilized to offer fine-tuned control over fiber dimensions and shapes by optimizing parameters and utilizing specialized spinnerets and collectors. Typically, this procedure employs a simple setup comprising four primary components of a high-voltage power source, a syringe pump, a spinneret, and a fiber collector. In this method, a polymer is dissolved in a highly volatile solvent and dispensed from a

syringe at a consistent or adjustable rate via the syringe pump. Under the influence of the applied electrostatic force, a separation of positive and negative charges occurs within the liquid. Charges of the same polarity as the needle's charge migrate towards its surface, leading to the formation of a charged polymer droplet at the tip of the needle [98]. Electrospinning produces ultrafine fibers (micrometers to nanometers) with film structures influenced by material factors (viscosity, concentration, conductivity, surface tension), environmental factors (temperature, humidity), and process factors (applied voltage, feeding rate, tip-to-collector distance) [99].

Zhang *et al*. [100] developed a hierarchically hollow-microfibrous cooling structure based on PVDF and poly(vinyl alcohol) (PVA) using a scalable, coaxial electrospinning method. The prepared porous cooling fibers exhibited a high solar reflection of 94% and a mid-infrared emission of 94%. Kim *et al*. [101] introduced electrospun polyacrylonitrile (PAN) nanofibers featuring spherical, ellipsoidal, and cylindrical morphologies as IR transparent films to be integrated with LWIR emitters. The porous films showed a solar reflectance of 95% and a high infrared transmittance of about 70%. Zhang *et al*. [102] employed electrospinning to create a RC fabric made of PVDF-HFP nanofibers and $SiO_2$ nanoparticles. The resulting fabric demonstrated high solar reflectivity of 97% and strong emissivity of 94% within the atmospheric window, making it highly effective for passive cooling applications.

### *2.4.3. Gas foaming method*

Gas dissolution foaming, particularly using carbon dioxide, is one of the promising techniques to foam polymers. $CO_2$ is an exceptional choice of gas for this technique because of its outstanding diffusion characteristics in the supercritical state of 31 ˚C and 7.3 MPa. Additionally, $CO_2$ can be diffused out of the polymer without leaving any residues or pollutants. The $CO_2$-based dissolution foaming process includes three stages of saturation, depressurization, and foaming. In the saturation stage, a sample is introduced in a pressure vessel at specific conditions of pressure and temperature. At the specific conditions of pressure and temperature, $CO_2$ diffuses into the sample and is dissolved. The amount of gas dissolved depends on the type of the polymer, temperature, and pressure of the gas. While dissolving $CO_2$ into the polymer, the polymer is plasticized and its glass transition temperature ($\boldsymbol{T_g}$) drops, which is known as effective ($\boldsymbol{T_g}$ (($\boldsymbol{T_{g,eff}}$). After saturating the polymer with $CO_2$, the pressure is released, and the sample is supersaturated; that is, the amount of gas dissolved into the polymer is much higher than the equilibrium concentration at room

temperature and pressure conditions. The third stage is when foaming takes place. If the saturation temperature is higher than $\boldsymbol{T_{g,eff}}$ the polymer is in a rubbery state with low viscosity, and therefore the foaming process occurs during the depressurization. This process is called one-step gas dissolution foaming. Otherwise, foaming is performed by heating the sample in a thermal bath at a temperature above $\boldsymbol{T_{g,eff}}$. This process is called two-step gas dissolution foaming [103][104].

Zhao *et al*. [105] for the first-time created micro and nano-layered alternating structures consisting of poly(carbonate) (PC) and PMMA utilizing a gas foaming technique with $CO_2$ as a blowing agent. By foaming samples ranging from 1 to 513 layers at 20 MPa and temperatures between 70˚C and 150˚C they could achieve a high solar radiation reflection of 93.5% and strong infrared emissivity of 91.2% in the atmospheric transparent window.

### *2.4.4. Phase inversion method*

Throughout the phase inversion process, a polymer solution undergoes a controlled transition from liquid to solid, achieving thermodynamic stability. This transformation involves a phenomenon known as liquid-liquid demixing, wherein the solution segregates into regions of differing polymer concentration. Over time, one phase becomes enriched with polymer content and initiates solidification through processes like gelation, vitrification, or crystallization. Simultaneously, the phase with lower polymer concentration creates pores within the solidified material, while the polymer-enriched phase forms the solid membrane matrix. Various conditions of introduction of demixing can be applied including [106]:

*i.* *Immersion precipitation (non-solvent induced phase separation - NIPS):* achieved by immersing the solution in a nonsolvent bath. The polymer solution is cast onto a substrate and then immersed in a nonsolvent bath, causing the solvent to diffuse out of the polymer matrix and the nonsolvent to diffuse into the matrix. This diffusion triggers phase separation, forming a porous material structure. Factors affecting this process include the solvent-nonsolvent interaction, polymer concentration, and temperature of the nonsolvent bath.

*ii.* *Vapor-induced phase separation (VIPS):* The polymer film is exposed to a vapor phase that induces phase separation. The vapor, often water or alcohol, diffuses into the polymer solution, causing the solvent to evaporate and phase separation to occur.

i. *Thermally-induced phase separation (TIPS):* In this process, the polymer solution is cooled to induce phase separation. Initially, the polymer is dissolved at high temperatures, and upon cooling, phase separation occurs, forming a solid matrix with pores. The cooling rate and polymer-solvent system strongly affect pore formation and structure.

ii. *Evaporation-induced phase separation (EIPS):* Phase inversion occurs due to solvent evaporation from the polymer solution, which causes the solution to become thermodynamically unstable, leading to phase separation. Factors like evaporation rate, ambient temperature, and humidity are critical to controlling the morphology and porosity.

#### *2.4.4.1. Factors affecting phase inversion: understanding key parameters*

Generally, the speed at which the solvent diffuses out of a cast film and the nonsolvent diffuses into the film from the coagulation bath controls the size of pores and the overall porosity of a membrane. These rates of diffusion are modifiable by adjusting the composition of the casting solution, casting parameters, and/or precipitation conditions. There a many experimental factors influencing the final morphology and the performance of the radiative coolers fabricated via phase inversion method including composition of the casting solution (such as polymer concentration and molecular weight, the type of solvent and nonsolvent, the ratio of solvent, nonsolvent, and polymer), the type of the substrate material (glass, polymer, and metal), the thickness of the cast polymer film, the speed of casting, temperature of casting, controlled air flow, the time and temperature of the evaporation prior to immersion, relative humidity while casting and during the applied evaporation time.

##### *2.4.4.1.1. Solvent and nonsolvent selection*

The choice of solvent/nonsolvent system in the phase inversion method has a substantial influence on porous structure morphology, mechanical properties, interfacial characteristics, and separation performance. The porosity of membranes can vary depending on the affinity between the solvent and nonsolvent, resulting in the formation of either more porous or denser porous materials. The polymer must be soluble or easily dispersible in the chosen solvent, and the solvent and nonsolvent must be miscible. The interaction between the solvent, nonsolvent, and polymer greatly affects the

rate of phase separation. A strong affinity between the solvent and nonsolvent leads to rapid exchange, causing fast phase separation and the formation of larger pores. Poor solvent-nonsolvent miscibility results in slower phase separation, which produces smaller pores and reduced porosity.

*2.4.4.1.2. Temperature*

Temperature influences the viscosity of the casting solution, which in turn impacts the exchange rate of solvent and nonsolvent during phase inversion. Temperature in fact affects the diffusion rates of the solvent and nonsolvent, as well as the polymer's solubility. Higher temperatures generally speed up the phase inversion process, promoting the formation of larger pores because the solvent diffuses out more quickly. Lower temperatures slow down the process, producing smaller pores and a denser polymer matrix.

*2.4.4.1.3. Immersion time (mostly applied to NIPS)*

The immersion time in the nonsolvent bath controls the rate of solvent exchange. A longer immersion time typically results in larger, more interconnected pores and higher overall porosity due to extended diffusion of the nonsolvent into the polymer film. A shorter immersion time produces smaller pores and a denser membrane, as the polymer solution has less time to phase-separate before solidifying. Long immersion times favor the formation of macrovoids and finger-like pores, while shorter times lead to a more homogeneous and compact morphology.

*2.4.4.1.4. Solvent evaporation (mostly applied to EIPS)*

The rate of solvent evaporation plays a critical role in pore formation. Fast evaporation leaves less time for phase separation, resulting in a denser membrane with smaller pores. Slow evaporation allows more phase separation, resulting in larger pores and greater porosity. Rapid solvent evaporation tends to create dense, skin-like layers on the surface, which can lead to asymmetric structures. Slow evaporation, on the other hand, promotes more uniform pore formation throughout the membrane, leading to symmetric and sponge-like morphologies.

*2.4.4.1.5. Additives*

Additives such as surfactants, plasticizers, or pore-forming agents can modify the pore size and distribution. For example, surfactants can reduce surface tension, leading to larger and more

uniform pores. Pore-forming agents that dissolve in the nonsolvent create additional porosity by leaving voids once they are removed. Additives can alter the final membrane structure by modifying the phase separation dynamics. Surfactants can enhance the formation of interconnected pore networks, while plasticizers can soften the polymer matrix and lead to more flexible, porous structures.

*2.4.4.1.6. Environmental factors (temperature and humidity in EIPS or VIPS)*

Environmental factors such as ambient temperature and humidity can influence the evaporation rate of the solvent. High humidity can slow down evaporation, leading to larger pores and higher porosity, while low humidity can speed up the process, resulting in smaller pores. Similarly, higher ambient temperatures increase solvent evaporation, leading to smaller pores, while cooler environments slow the evaporation process and promote larger pore formation. High humidity environments often result in membranes with thicker skin layers and dense structures due to slower evaporation. Low humidity accelerates evaporation, leading to more open, porous morphologies.

*2.4.4.1.7. Polymer-solvent interaction parameters*

The thermodynamic interaction between the polymer and solvent, controls the miscibility of the polymer in the solvent. Strong polymer-solvent interactions result in delayed phase separation, leading to smaller pores, while weak interactions cause faster demixing and the formation of larger pores. A well-balanced polymer-solvent interaction results in more homogeneous phase separation, while a poor interaction leads to asymmetric membranes with dense top layers and larger pores in the bulk.

*2.4.4.1.8. Polymer concentration*

The polymer type and structure play a crucial role in influencing structure hydrophilicity, and the thermal and chemical stability of the it. The polymer concentration also stands as one of the most thoroughly influential parameters. Typically, increasing the initial polymer concentration in the casting solution leads to the formation of membranes with thicker and denser skin-layers matrix with smaller pores and lower porosity. This effect arises from the higher polymer concentration at the polymer/nonsolvent interface, which causes an increased viscosity of the casting solution, thereby slowing down the out-diffusion of solvent. As the polymer solution becomes more

concentrated, phase separation is less pronounced, leading to tighter packing of polymer chains and fewer voids. In contrast, lower polymer concentrations promote the formation of larger pores with higher porosity because there is more solvent relative to polymer, allowing for greater solvent removal and pore formation [107][106][108][109][110].

## 2.5. Radiative cooling applications in buildings

The RC method, with its outstanding passive cooling potential, can greatly contribute to energy-efficiency in buildings. This section presents the integration of RC technologies into building cooling systems. Figure 2.7 of this section also provides a bibliometric analysis of the number of papers published on different applications of RC from 1990 to January 10, 2022. The dominance of hybrid RC research suggests that combining RC with other systems is seen as a promising approach to overcoming limitations of standalone RC technologies.

### *2.5.1. Air- and water-based cooling systems*

In air-based cooling systems that consist of a thermal radiator, the cooled air is either circulated artificially by a fan or by a natural process due to the buoyancy effect (Figure 2.5 (a)). That is, in these systems air is used as the heat exchange media that is directly heated by the interior environment and cooled by the thermal radiator. Similarly, in water-based cooling systems, water is utilized as a medium to transfer heat (Figure 2.5 (b)). These systems normally consist of a thermal radiator, insulated water tank, heat exchanger, and water pump. Water is cooled by the thermal radiator at night and then stored in an insulated water tank. During the day the cooled water is circulated with the help of a water pump through the heat exchanger to provide space cooling [2].

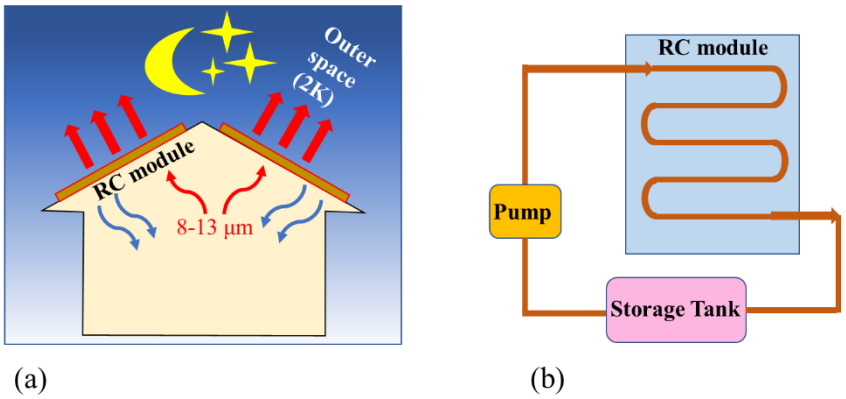


*Figure 2.5. A schematic demonstration of (a) an air-based cooling system (b) a water-based cooling system reported in* [2].

### *2.5.2. Integrated cooling systems*

RC can also be integrated with a variety of energy-related systems such as solar collectors [111], photovoltaics, thermophotovoltaics, and air-conditioners [112]. One of the most promising applications of RC modules is to integrate them with air-conditioning systems to enhance their operating efficiency. To date, different studies based on integration of either nocturnal or diurnal RC material structures with HVAC or other cooling systems have been performed. In these hybrid systems, chilled water provided by a radiative cooler is utilized for the cooling coils in an air-conditioning system to enhance the system efficiency [2]. Jeong *et al*. [113] reported a design of integrated RC-HVAC system comprising two types of cooling coils of conventional and RC-supplied. In this proposed cooling design, conventional chiller systems used in the refrigeration cycle are replaced by an RC material structure. The proposed cooling system can provide a potential saving in energy consumption of 35% by assisting the conventional space cooling system. In another study on RC-assisted HVAC systems, Zhang *et al*. [6] added a cold-water storage tank to stock cooling energy from a RC. Furthermore, nocturnal radiative coolers can also be combined with evaporative cooling systems to provide pre-cooling and strengthen systematic cooling efficiencies as shown in Figure 2.6. In this design, the radiative cooler produces cold water during the night and during the daytime the cold-water flows through the cooling coils to precool the hot outdoor air before going through a direct evaporative cooling procedure [3].

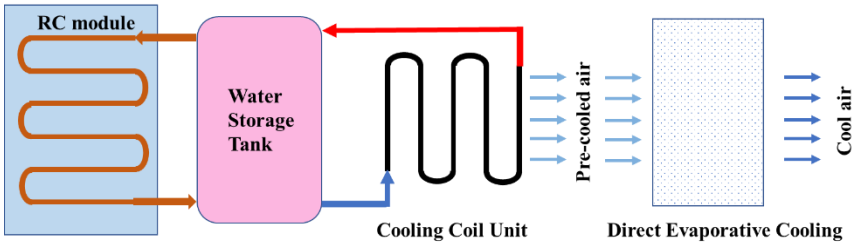


*Figure 2.6. A schematic illustration of an evaporative cooling system integrated with RC module reported in* [3].

### *2.5.3. Cool roofs*

The cool roof is the most direct and mature application of RC technology which is directly applied as the building roof. During the hot months, the cooling load of a building can be substantially reduced using cool roofs that can reflect most of the incident solar radiation, while having thermal emittance [11]. Many studies have evaluated buildings cooling energy savings using solar reflectivity of cool roofs [114][115][116][117][118][119][120]. Romeo and Zinzi [116] evaluated the benefits of a cool roof application with solar reflectance of 86% and thermal emittance of 88% on the energy and comfort performance in a non-residential building with a 700 $m^2$ roof in Trapani, Sicily. A roof surface temperature reduction of up to 20 ˚C was obtained. Zhang *et al*. [115] predicted the performance of cool roofs in tropical regions of Singapore using the Complex Finite Fourier Transform method and validated their results by a field experiment on residential roofs in Singapore. Based on the predictions, they also studied the cost-efficiency of implementing cool paint and roof ventilation on concrete roofs using life cycle analysis of cool roofs and reported annual cooling energy savings of 33-57 USD·$m^{-2}$. The payback periods were obtained to be less than 6 or 2 months for the roofs with or without ventilation. Developing an improved Roof Thermal Transfer Value model, Fang *et al*. [12] evaluated a metamaterial film-based cool roof. They showed the metamaterial RC material structure named RadiCold could dissipate about 137.6–268.7 kWh·$m^{-2}$·$yr^{-1}$ of heat from the buildings to the outdoor environment. In contrast, buildings with shingle and Thermoplastic Polyolefin cool roof exhibited lower cooling load reduction. Integrated with an air conditioning system with COP of 3, the RadiCold module would further save the cooling electricity by more than 88 kWh·$m^{-2}$·$yr^{-1}$ due to its cooling load reduction.

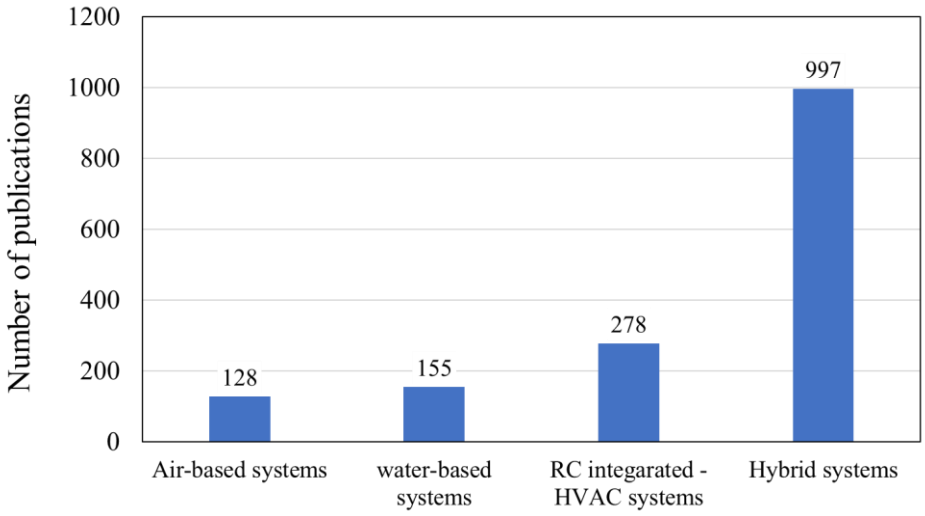


*Figure 2.7. Bibliometric study of the number of published papers studying different RC applications from 1990 to January 10, 2022 (Source: www.sciencedirect.com, Keywords: "Radiative cooling", Air-based, Water-based, HVAC, Hybrid).*

## 2.6. Energy savings and cost analysis

In this section, the energy and cost savings achieved when using some of the proposed RC material structures are presented.

### *2.6.1. An integrated photonic solar reflector and thermal radiator system*

Here, an energy saving assessment provided by Raman *et al*. [4] based on their design of a photonic RC material structure is presented. Figure 2.8 shows their photonic radiative cooler which consists of seven alternating layers of hafnium dioxide ($HfO_2$) and silicon dioxide ($SiO_2$) of varying thicknesses, on top of a 200 nm layer of silver (Ag), deposited on top of a 200-mm silicon wafer.

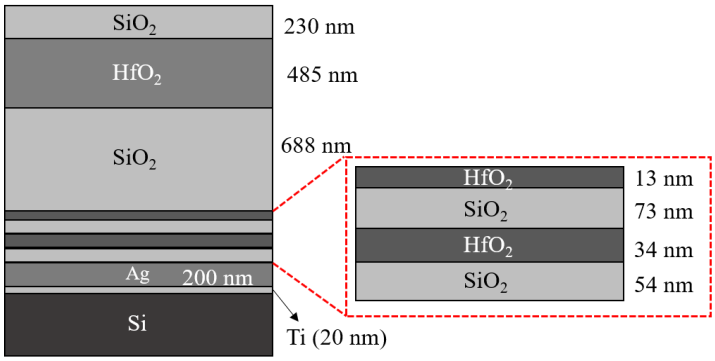


*Figure 2.8. A schematic of the radiative cooler structure comprised of alternating layers of $SiO_2$ and $HfO_2$ designed by Raman et al.* [4].

In this energy savings assessment, it is considered that the roof of a typical commercial building is covered by the proposed photonic RC material structure. It is also assumed that while a part of the heat load is transferred to the RC module on the roof, an air conditioning (HVAC) system is used to ensure the cooling requirements are met. In this work, EnergyPlus software is used to perform simulations to determine the cooling load on an hourly basis over a year in Phoenix, Arizona, USA for a three-story medium-sized commercial benchmark building with a rooftop area of 1,600 $m^2$. The interior temperature of the building is assumed to be maintained at $T_{interior}$ = 24 ˚C at all hours. An air-conditioning system with a coefficient of performance (COP) of 2.8 is assumed to provide cooling for the remaining heat load. Their results for saving energy on a monthly basis by using the proposed RC module are provided in Table 2.2. Utilization of the RC module resulted in an estimated annual electricity savings of about $1.185 \times 10^5$ kWh.

*Table 2.2. Energy saved by using a RC module to reduce the cooling load in a building in Phoenix, Arizona* [4].

| **Month** | **Jan** | **Feb** | **Mar** | **Apr** | **May** | **Jun** | **Jul** | **Aug** | **Sep** | **Oct** | **Nov** | **Dec** |
|---|---|---|---|---|---|---|---|---|---|---|---|---|
| **Electricity saved (kWh)** | 2853 | 4439 | 8073 | 10487 | 11853 | 13975 | 15365 | 15756 | 13292 | 11341 | 7609 | 3121 |

Raman *et al*. [4] also performed a cost analysis to roughly estimate the monetary value of the energy savings achieved using a photonic RC module. It was estimated that the RC module had a twenty-year lifespan, and the following assumptions were made: the cost of grid electricity is $0.10

$kWh^{-1}$, the fixed operating costs are \$0.8 $m^{-2}$, the discount rate is 5%, and the installed costs ranged between \$20 $m^{-2}$ and \$70 $m^{-2}$. Under these assumptions the cost of the energy saved ranges from \$0.03 $kWh^{-1}$ to \$0.09 $kWh^{-1}$. This rough cost analysis suggests that RC technologies can provide an economical solution for providing building cooling with minimal environmental impacts.

### *2.6.2. A hybrid radiative cooler and HVAC system for single-family houses in the USA*

Recently, Zhang *et al*. [6] proposed a hybrid Radiative-Cooled Cold storage cooling ($RadiCold_{hc}$) system for single family houses. The $RadiCold_{hc}$ system includes two major components of: 1) a cold energy collector subsystem (i.e., RadiCold modules, Figure 2.9) laminated with an RC material structure (a glass-polymer metamaterial coated with silver with a cooling power of 110 $W \cdot m^{-2}$), and 2) a reduced-size split air conditioner (RSAC) to provide complimentary cooling capacity.

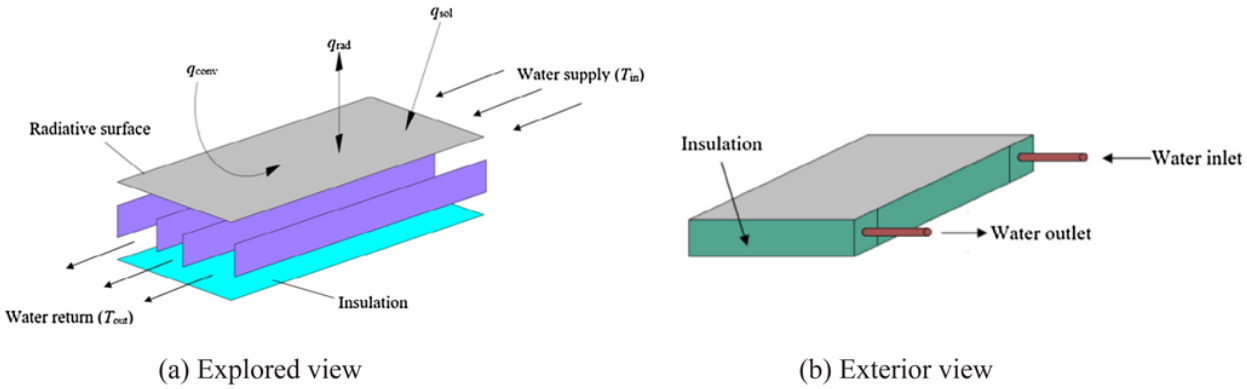


*Figure 2.9. A schematic of the RadiCold subsystem used in* [6]*: (a) explored view and (b) exterior view. Reproduced with permission. Copyright 2018, Elsevier. A schematic of the RadiCold subsystem used in* [6]*: (a) explored view and (b) exterior view. Reproduced with permission. Copyright 2018, Elsevier.*

In this work, for evaluation of the performance of the $RadiCold_{hc}$ system, a typical two-floor single-family house, with floor area of 204 $m^2$ and roof area of 118 $m^2$ is modeled. The parallel water channels inside the RadiCold module are assumed to be made of polycarbonate. The dimension of the RadiCold module is assumed to be 1.0 $m^2$ (1.0 m ×1.0 m) with an average cooling capacity of approximately 0.1 kW. The interior temperature is maintained at 24 ˚C. The simple payback period (SPP) is calculated using the following equation:

$$SPP = \frac{C_{Radi} + C_{RSAC} - C_{SACL}}{(E_{SACL} - E_{Radi_{hc}})P_E} \quad (2.1)$$

where $C_{Radi}$ is the cost of the RadiCold subsystem, which includes the cost of RadiCold module, pump, tank (1.3 $m^3$ for 26 RadiCold modules), cooling coil, and pipe network; $C_{RSAC}$ is the cost of RSAC in their hybrid system; $C_{SACL}$ is the cost of the split air conditioner lonely (SACL), working without any support from the RC module; $E_{SACL}$ is the annual cooling electricity consumption of the SACL system; $E_{Radi\text{-}hc}$ is the annual cooling electricity consumption of the hybrid RC system; and $P_E$ is the electricity price. It follows that "$C_{Radi}$ + $C_{RSAC}$" is the total cost of the hybrid RC system and "$C_{SACL}$" indicates the total cost of a typical air conditioning system in single-family houses. Therefore, "$C_{Radi}$ + $C_{RSAC}$ - $C_{SACL}$" in the numerator of the equation is the incremental cost of the $RadiCold_{hc}$ system compared to the SACL case. The SPP was determined based on the cooling performance of their hybrid system in Orlando using EnergyPlus software for differing numbers of RadiCold modules. The cost of the RadiCold module in this work is comprised of the cost of the radiative film and the polycarbonate panel which is generally estimated to be \$25 $m^{-2}$. The cost of the major components in the $RadiCold_{hc}$ system are listed in Table 2.3. The electricity price is considered to be \$0.12 $kWh^{-1}$ for Orlando. The calculated results revealed that using 26 RadiCold modules with an area of 1.0 $m^2$ results in a SPP of about 8 years.

*Table 2.3. Cost of the major components in the $RadiCold_{hc}$ system, other than the RadiCold module* [6].

| **Component** | Tank | Pipe network | Plastics pump | Cooling coil | Split air conditioner |
|---|---|---|---|---|---|
| **Average cost** | \$134 $m^{-3}$ | \$2.5 $m^{-1}$ | \$1.7 $W^{-1}$ | \$83.2 $kW^{-1}$ | \$404.5 $kW^{-1}$ |

### *2.6.3. An integrated system using a photonic RC for cooling an office building*

Wang *et al*. [5] developed a system to integrate a one-dimensional photonic RC material structure (which was presented in ref Wang *et al*. [5] developed a system to integrate a one-dimensional photonic RC material structure (which was presented in ref [4] and briefly described in section 5.1 of this paper) into a medium-sized office building with a total floor area of 5000 $m^2$ and evaluated its energy saving performance. In this study it was assumed that 60% of the roof area of the building is adopted for the RC modules. This photonic-based RC system comprises two hydronic

loops of a water-based RC loop and a space-cooling loop. Water is circulated through the RC loop installed in the roof by means of a pump before being stored in a tank (Figure 2.10). The second loop, which is the space-cooling loop, uses the cold water in the storage tank and a supplementary chiller to provide cooling to radiant slab surfaces.

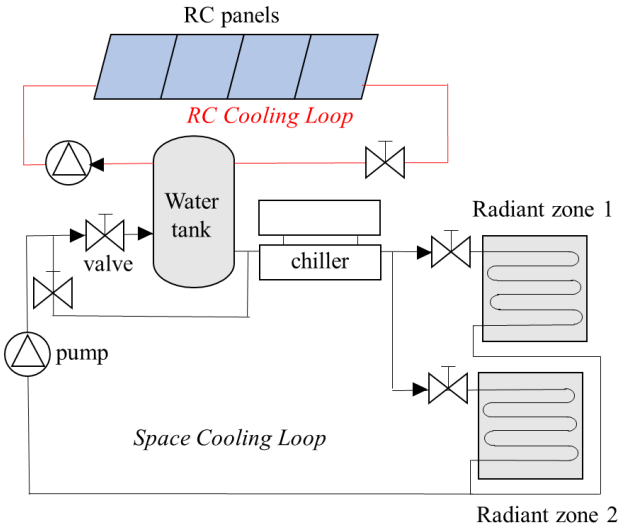


*Figure 2.10. A schematic of the RC integrated-cooling system proposed in* [5].*. A schematic of the RC integrated-cooling system proposed in* [5].

Simulation results demonstrated that the photonic RC system saved between 45% and 68% of the electricity required for cooling when compared to a variable-air-volume (VAV) system and between 9% and 23% relative to a nocturnal RC system.

## 2.7. Radiative cooling limitations

RC surfaces can face several practical limitations that may hinder their performance and long-term durability. These include environmental factors, material aging, and the interaction of the material with external conditions such as dust accumulation, atmospheric particulates, UV exposure, and moisture. Below is a detailed discussion of these challenges and potential mitigation strategies:

### *2.7.1. Dust Accumulation and Atmospheric Particulates*

Dust and particulate matter accumulating on RC surfaces can significantly reduce their optical performance by diminishing solar reflectance and LWIR emissivity. This issue is particularly severe in densely populated regions with high levels of air pollution. Hydrophobic or

superhydrophobic self cleaning coatings can prevent dust adherence and facilitate easy cleaning by rain or manual washing. Surfaces engineered with nanostructures can also reduce the adherence of dust and particles.

### *2.7.2. Material Aging and Texture Degradation*

Over time, RC materials may experience changes in texture or optical properties due to environmental exposure, including UV radiation, temperature fluctuations, and chemical reactions. Materials with excellent UV resistance and long-term durability can be chosen to mitigate this problem. Transparent, UV-resistant coatings can also shield the RC material from direct exposure, preserving its properties over time.

### *2.7.3. Hydrophobicity and Interaction with Water*

Exposure to water may alter the material's optical properties, especially if the material is hydrophilic and absorbs moisture. This can lead to swelling, reduced emissivity, or optical degradation. Using hydrophobic materials ensures minimal water absorption and maintains performance even in humid or wet environments.

# Chapter 3

## 3. Environnemental implications of RC technologies

### 3.1. Introduction

Global warming continues to increase and is causing a rapid rise in energy demands for cooling [121]. According to the International Energy Agency (IEA), the global energy demand from air conditioning systems is estimated to triple by 2050, which will further contribute to global warming [122] considering the significant amounts of greenhouse gases they emit [9][123][123][8]. According to the International Panel on Climate Change (IPPC), global warming due to human activities has caused Earth's temperature to increase by about 1 °C as compared to pre-industrial levels. If the current rate of increase continues, Earth's temperature is likely to increase by 1.5°C between 2030 and 2050 due to global warming [124]. The Earth's temperature is influenced by a complex exchange of radiant energy, wherein the atmosphere and surface absorb incoming solar radiation and emits thermal radiation in the infrared spectrum to outer space. The increasing severity of climate change has brought the concept of radiative forcing (RF) to the forefront of environmental science. RF, which measures the change in energy balance in the Earth's atmosphere, has been a critical indicator of how human activities are driving global warming. According to recent scientific reports, the rise in RF is directly linked to significant alterations in the Earth's climate, leading to more frequent extreme weather events, rising sea levels, and

disruptions to ecosystems. RF, measured in $W \cdot m^{-2}$, represents the difference between incoming and outgoing radiant energy. Ramaswamy et al. [125] defined RF as "*the change in net (down minus up) irradiance (solar plus longwave; in $W \cdot m^{-2}$) at the tropopause after allowing for stratospheric temperature to readjust to radiative equilibrium, but with surface and tropospheric temperatures and state held fixed at the unperturbed values*". RF increases when atmospheric greenhouse gases absorb outgoing radiation, leading to higher climatic temperatures [126][127].

The Paris Agreement, adopted in 2015 and coming into force in 2016, is a legally obligatory international agreement intended to combat climate change. Its main objective is to limit global temperature increases to well below 2 °C above pre-industrial levels, while pursuing efforts to limit the increase to 1.5 °C. The agreement encompasses various measures including cutting global greenhouse gas emissions, promoting adaptation, and enhancing transparency and support mechanisms for climate action [128]. Eliminating emissions and removing carbon dioxide from the atmosphere, collectively referred to as 'mitigation,' along with reducing damage by adapting to climate risks and impacts, are currently recognized strategies for combating global warming and its effects. Climate change mitigation strategies can be broadly categorized into two approaches: emission reduction and geoengineering. Emission reduction focuses on minimizing the release of greenhouse gases, primarily through renewable energy adoption, energy efficiency improvements, and reforestation efforts. These methods aim to tackle the root cause of climate change by reducing the concentration of greenhouse gases in the atmosphere. Conventional mitigation efforts focus on decarbonization strategies that reduce $CO_2$ emissions, such as using renewable energy, fuel switching, efficiency improvements, and nuclear power. On the other hand, geoengineering strategies directly intervene in the Earth's climate system to counteract the effects of climate change. In geoengineering approaches such as Solar Radiation Management (SRM), which is also known as solar engineering, a portion of the Sun's energy is reflected back into space. Techniques in this category used to manage RF include stratospheric aerosol injection, marine cloud brightening, cirrus cloud thinning, space-based mirrors, surface-based brightening, and various other radiation management strategies [129][130][131][132]. Despite the help of SRM in mitigating the climate risk and minimizing ecosystem degradation, it does not tackle the underlying causes of global warming, nor does it fully reverse all the climate changes induced by greenhouse gases. This means that if SRM efforts were to cease, temperatures could rapidly rebound, potentially causing more harm [130]. Carbon Dioxide Removal (CDR) is another

geoengineering strategy that refers to any practice that includes removing and restoring $CO_2$. It is proposed for $CO_2$ to be captured directly from the atmosphere using negative emissions technologies (NETs) or carbon dioxide removal methods. These methods include bioenergy with carbon capture and storage (BECCS), biochar production, enhanced weathering, direct air capture, ocean fertilization, ocean alkalinity enhancement, soil carbon sequestration, afforestation and reforestation, wetland restoration, mineral carbonation, and using biomass in construction [131][132]. However, while CDR technologies like direct air capture are theoretically scalable, the infrastructure required to remove significant amounts of $CO_2$ from the atmosphere is immense and costly. Current CDR methods are expensive and scaling them to the necessary level may not be economically feasible in the short term. Similar to SRM, there is a concern that the prospect of CDR could lead to complacency in reducing emissions. Policymakers and industries might rely too heavily on future CDR technologies rather than implementing immediate emission reductions. Therefore, despite these mitigation efforts, global warming due to increasing RF levels remains a significant and pressing challenge. Furthermore, global warming rates are expected to increase as global energy consumption and emissions continue to rise. For example, the International Energy Agency (IEA) projects the global energy demand for air conditioning systems will triple by 2050, significantly contributing to global warming due to the substantial greenhouse gas emissions these systems produce [122][9][123][123][8].

In recent years, RC has emerged as a promising geoengineering approach. Unlike SRM and CDR, RC leverages the natural ability to emit infrared radiation into space, cooling surfaces passively and without additional energy input. Advanced materials designed for RC can reflect solar radiation while efficiently emitting thermal radiation, potentially mitigating the warming effects associated with RF. That is, RC technology cools terrestrial objects by emitting radiation to outer space over a spectral region where the atmosphere is highly transparent (from ~8 to 13 μm). This process can be implemented on a large scale as a geoengineering method to alleviate global warming while reducing energy consumption and emissions associated with cooling loads [12][13][14][15][16][28][27]. RC technology addresses global warming through two key mechanisms: (1) as a passive cooling method, it conserves electricity by lowering the cooling load in buildings, which indirectly reduces $CO_2$ emissions from electricity production, and (2) by enhancing the radiative heat flow from Earth to outer space, thereby decreasing radiative forcing

(RF) and potentially achieving negative RF [28]. Despite its potential, the environmental implications and life cycle assessment (LCA) of RC have not been thoroughly investigated.

RC technology reduces the cooling load in buildings by radiating heat into space through infrared radiation, thereby decreasing electricity consumption and its associated $CO_2$ emissions. Kolokotroni *et al*. [133] demonstrated the potential for RC to mitigate global warming by studying the benefits of installing RC roofs on single-story houses in Jamaica, Ghana, and Brazil. The cool paint used in the study had a solar reflectance of 82% and a thermal emittance of 90%. The cooling load required to maintain a constant temperature of 24 ˚C was simulated both with and without the use of RC roofs. The results showed significant energy savings: 188 $kWh \cdot m^{-2} \cdot yr^{-1}$ in Jamaica, 191 $kWh \cdot m^{-2} \cdot yr^{-1}$ in Ghana, and 195 $kWh \cdot m^{-2} \cdot yr^{-1}$ in Brazil. The study also calculated the potential reduction in $CO_2$ emissions, assuming a Coefficient of Performance (COP) of 3 for air-conditioning systems. The $CO_2$ emissions reductions were estimated based on local electricity production emissions factors: 0.2147 kg $CO_2 \cdot kWh^{-1}$ for Ghana, 0.7961 kg $CO_2 \cdot kWh^{-1}$ for Jamaica, and 0.0926 kg $CO_2 \cdot kWh^{-1}$ for Brazil [134]. The calculated $CO_2$ savings were 13.5 kg $CO_2 \cdot m^{-2} \cdot yr^{-1}$ in Ghana, 50 kg $CO_2 \cdot m^{-2} \cdot yr^{-1}$ in Jamaica, and 6 kg $CO_2 \cdot m^{-2} \cdot yr^{-1}$ in Brazil. Despite the similar energy savings across the countries, Jamaica showed the greatest environmental benefit due to its higher $CO_2$ emissions from electricity generation. This study highlights the significant potential of RC in reducing energy consumption and $CO_2$ emissions, particularly in regions with high electricity-related emissions.

This chapter explores the LCA methods used to evaluate the environmental impact, sustainability, and feasibility of RC in comparison to other common materials. This chapter specifically compares RC materials from studies by Pirvaram *et al*. [135] (Sample 1-8-1.25; a detailed description of the preparation and characterization of this sample is provided in Chapter 5), Wang *et al*. [52], and Li *et al*. [87], alongside common construction materials like white cement paste, road asphalt, concrete, and grey cement. Also, common roofing materials, including roofing shingle, ceramic roofing tile, and PVC roofing material, as well as natural surfaces like forests and oceans are analyzed. To further contextualize of this work’s analysis, idealized cases such as perfect RC, perfect reflector, and blackbody are referenced. This study investigates the impact of covering 1% of the Earth's surface with the materials provided in Table 3.2. This investigation aims to determine the effect of such replacements on the terrestrial RF balance. By substituting portions of the Earth's

surface with specified materials with the provided $\bar{R}_{solar}$ and $\bar{\varepsilon}_{LWIR}$ values in Table 3.2, this chapter seeks to elucidate potential alterations in the radiative balance and assess the implications for global warming. This investigation contributes to a deeper understanding of how surface modifications may influence radiative forcing, thereby informing discussions surrounding climate mitigation strategies and land use planning. By analyzing these strategies, it is aimed to provide a comprehensive overview of their potential role in mitigating climate change and reducing RF on a global scale.

## 3.2. Methods

### *3.2.1. Determining the net cooling power and radiative forcing*

The net cooling power, $P_{net\ cooling}$, is a critical metric for evaluating the performance of RC materials and systems. It is determined by the balance between the cooling power provided by thermal radiation and the heat gains from solar absorption, and convection. The net cooling power is calculated using Equation 3.1 [136]:

$$P_{\text{net},Cooling}(T_{RC}) = P_{RC}(T_{RC}) - P_{atm}(T_{amb}) - P_{Solar} - P_{Conv.}(T_{RC}, T_{amb}) \quad (3.1)$$

Where $P_{RC}$ is the radiative heat transfer from RC to outer space, $P_{atm}$ is the atmospheric downward thermal radiation received by the RC, $P_{solar}$ is the solar irradiance absorbed by the RC, and $P_{Conv.}$ is the convective heat transferred from the surroundings, respectively. Furthermore, $T_{RC}$ and $T_{amb}$ are the RC sample and ambient temperatures, respectively.

A schematic diagram utilizing data reported by NASA depicting the global mean energy balance of the Earth is presented in Figure 1. The radiative heat transfer values presented in Figure 1 are used in conjunction with Equation 1 to examine how the surface albedo and emissivity of different materials influence the energy balance between Earth and outer space [137][138]. The numerical values in Figure 1 denote the best estimates for the magnitudes of the globally averaged incoming and outgoing radiant energy. As shown in Figure 1, the average incident solar energy per square meter at the top of the atmosphere (TOA) is approximately 340.4 W·m$^{-2}$, with 186.2 W·m$^{-2}$ reaching the Earth's surface, $P_{SolarToEarth}$. Out of the solar irradiance reaching the Earth's surface, 163.3 W·m$^{-2}$ is absorbed by the surface, while 22.9 W·m$^{-2}$ is reflected back into space. The

absorbed radiation is converted into heat energy. The Earth's surface emits longer wavelength infrared radiation. As a rough approximation, an average emissivity for Earth's surface, $\bar{\varepsilon}_{Earth}$, is about 95%, owing to the prevalence of natural land and water surfaces with relatively high emissivity values. This results in a thermal outgoing flux at the TOA of approximately 239.9 $W \cdot m^{-2}$. In general, the incoming solar flux is 340.4 $W/m^2$, with 77.9 $W/m^2$ reflected by the atmosphere and 22.9 $W/m^2$ by the Earth's surface, while a total of 239.9 $W/m^2$ is radiated out. Accordingly, there is an imbalance of 0.6 $W \cdot m^{-2}$ in the incoming and outgoing radiation at the TOA causing the Earth's temperature to increase. Notably, in comparison, Johnson et. al.[139] have estimated the imbalance of the radiative forcing to be 0.71 $W \cdot m^{-2}$.

The optical properties of materials at the Earth's surface effects its radiative energy balance with outer space. The effects of different surfaces on the radiative forcing can be determined considering Equations 2 and 3. Radiative Forcing (RF) is defined as the difference between the total incoming power (solar radiation) absorbed by the Earth and the total outgoing thermal radiation emitted by the Earth back into space at the TOA. The equation for calculating the radiative forcing ($RF$) is given by:

$$RF = \sum P_{Incoming,TOA} - \sum P_{Outgoing,TOA} = P_{Solar-} P_{ReflectedSolar-} P_{TotalEmitted} \quad (3.2)$$

where $P_{Incoming,TOA}$ is the incoming thermal radiation at the TOA, $P_{Outgoing,TOA}$ is the outgoing thermal radiation emitted by the Earth at the TOA, $P_{Solar}$ is the total incoming solar radiation, $P_{ReflectedSolar}$ is the total reflected solar radiation by the atmosphere and Earth's surface, and $P_{TotalEmitted}$ is the total radiation emitted by the atmosphere and the Earth's surface. As shown in Figure 1 the average incoming solar radiation at the TOA is 340.4 $W \cdot m^{-2}$, the total outgoing radiation at the TOA is 239.9 $W \cdot m^{-2}$ (and the imbalance is 0.6 $W \cdot m^{-2}$).

The RF that would occur if different materials were placed on top of the Earth's surface can be estimated by incorporating the average surface albedo ($\bar{R}_{solar}$) and the average long wavelength infrared emissivity ($\bar{\varepsilon}_{LWIR}$) into the balance for RF, as shown in as shown in Equation 3.3:

$$RF_i = P_{Solar} - (\bar{R}_{solar} \times P_{SolarToEarth}) - \left(P_{ReflectedSolar\_Atm}\right) - \left(\left(\frac{\bar{\varepsilon}_{LWIR}}{\bar{\varepsilon}_{Earth}}\right) \times P_{Emitted\_AW} + P_{Emitted\_Atm} + P_{Emitted\_Clouds}\right)\right) \quad (3.3)$$

where $P_{Emitted\_AW}$, $P_{Emitted\_Atm}$, and $P_{Emitted\_Clouds}$ are the thermal radiation emitted by Earth's surface and passing through atmospheric window (40.1 W·m$^{-2}$), emitted by the atmosphere (169.9 W·m$^{-2}$), and emitted by the clouds (29.9 W·m$^{-2}$), respectively.

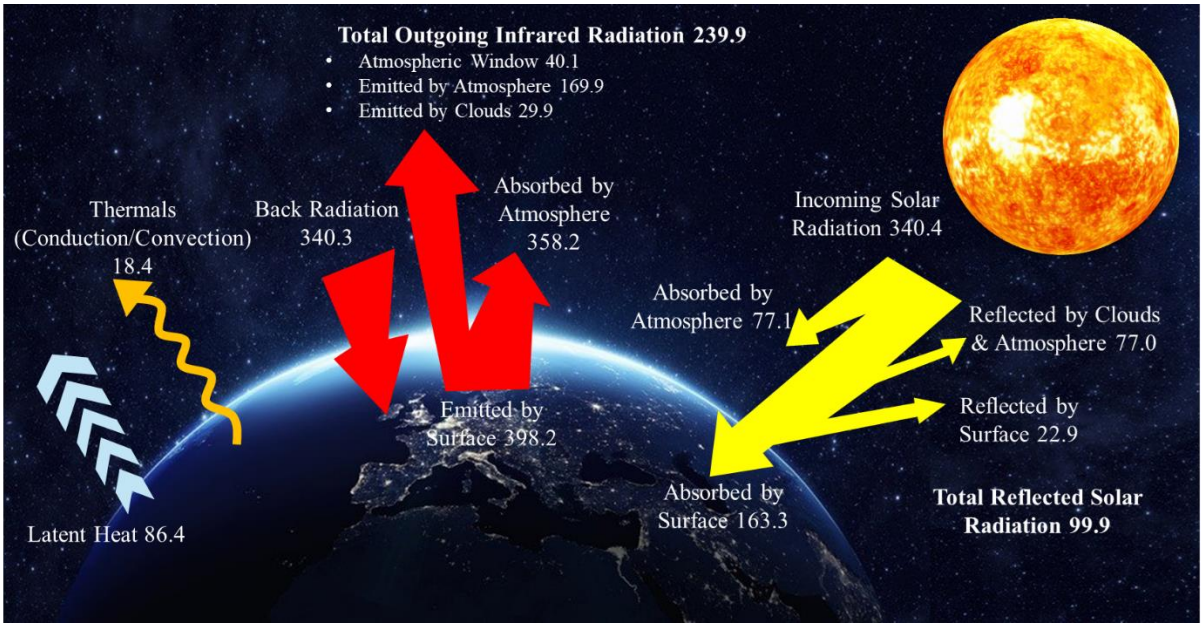


*Figure 3.1. Global energy balance. Numerical values indicate the magnitudes of individual energy fluxes, measured in W·m$^{-2}$ as reported by NASA* [137][138].

### *3.2.2. Determining the global warming potential using the net cooling power of different materials*

The Global Warming Potential (*GWP*) is a metric used to compare the impact of the emissions of a particular gas on RF to that of $CO_2$ over a specific time horizon. The *GWP* for a given substance can be expressed as follows: [126]:

$$GWP_i(H) = \frac{AGWP_i(H)}{AGWP_{CO_2}(H)} = \frac{\int_0^H RF_i(t)dt}{\int_0^H RF_{CO_2}(t)dt} \quad (3.4)$$

Where $AGWP_i(H)$ is the absolute global warming potential for substance *i*, and $AGWP_{CO_2}(H)$ is the absolute global warming potential for $CO_2$. In essence, the *GWP* of a substance is determined by comparing the time-integrated global radiative forcing caused by a pulse emission of that substance to that of an equivalent mass of $CO_2$ over the specified time horizon of *H*. GWP is measured in carbon dioxide equivalents ($CO_{2eq}$) and varies with the time horizon because different substances decay at different rates in the atmosphere. For instance, methane ($CH_4$) has a *GWP* of 84-87 $kgCO_{2\text{-}eq}$ over a 20-year horizon and 28-36 $kgCO_{2\text{-}eq}$ over a 100-year horizon [140].

The absolute global warming potential for a substance, assuming its removal from the atmosphere follows exponential decay, can be approximated using Equation 3.5:

$$AGWP_i(H) = A_i\tau_i\left(1 - \exp\left(-\frac{H}{\tau_i}\right)\right) \tag{3.5}$$

Where $A_i$ and $\tau_i$ are the radiative efficiency (RE) and the atmospheric lifetime of substance *i*, respectively. The expression for *AGWP* $CO_{2\text{-}eq}$ is more complex due to the absorption and transport processes in the ocean over different timescales. An exponential decay model does not accurately represent the atmospheric concentration caused by a $CO_2$ pulse emission. Forster *et al*. approximated the *AGWP* of $CO_2$ using Equation 3.6:

$$AGWP_{CO_2}(H) = A_{CO_2}\left\{a_o H + \sum_{i=1}^{3} a_i\alpha_i\left(1 - \exp\left(-\frac{H}{\alpha_i}\right)\right)\right\} \tag{3.6}$$

Where $A_{CO_2}$ is the RE of $CO_2$, $a_0 = 0.217$, $a_1 = 0.259$, $a_2 = 0.338$, $a_3 = 0.186$, $\alpha_1 = 172.9$ years, $\alpha_2 = 18.51$ years and $\alpha_3 = 1.186$ years. According to Equation 6, the AGWP of $CO_2$ for 20 and 100 years are $2.49 \times 10^{-14}$ $W{\cdot}m^{-2}{\cdot}yr{\cdot}kg^{-1}$ and $9.17 \times 10^{-14}$ $W{\cdot}m^{-2}{\cdot}yr{\cdot}kg^{-1}$, respectively [127].

If the net cooling power of a given RC material structure is known, the AGWP can be approximated using Equation 3.7 [28]:

$$AGWP_{RC_i}(H) = -\int_0^H \frac{P_{net\ cooling,i}}{A_{RC_i}}\left(\frac{1}{A_{tropopause}}\right)dt \tag{3.7}$$

Where $RC_i$ represents RC material structure $i$, $P_{net\ cooling,i}$ is the cooling power for $RC_i$, , $A_{RCi}$ is the projected area of $RC_i$ on the horizontal plane, and $A_{tropopause}$ is the area of the tropopause. The negative sign ensures that the $AGWP$ is negative when an RC material structure has a positive net cooling effect. The $AGWP$ for an RC material structure is normalized to the area of the tropopause by the $(1/A_{tropopause})$ term in Equation 7, allowing the global warming potential of the RC material structure to be calculated in terms of $CO_{2eq}$. Thus, the global warming potential of an RC material structure can be approximated using Equation 3.8:

$$GWP_{RC_i}(H) = \frac{AGWP_{RC_i}(H)}{AGWP_{CO_2}(H)} = \frac{-\int_0^H \frac{P_{net\ cooling,i}}{A_{RC_i}}\left(\frac{1}{A_{tropopause}}\right)dt}{A_{CO_2}\left\{a_o H + \sum_{i=1}^{3} a_i\alpha_i\left(1-\exp\left(-\frac{H}{\alpha_i}\right)\right)\right\}} \quad (3.8)$$

The units on the $GWP_{RCi}\,(H)$ values are in $kgCO_{2\text{-}eq}\cdot m^{-2}$ which, when multiplied by the area of the RC material structure or panel, gives the desired units of $kgCO_{2\text{-}eq}$. The $GWP_{RCi}$ values can be used in calculating the total GWP of RC technologies in life cycle assessment studies. The negative $GWP_{RCi}$ values act as a credit that offsets $CO_{2\text{-}eq}$ emissions from other factors, such as emissions released during the manufacturing of RC panels or the generation of the base cooling load.

### *3.2.3. Estimating the global warming potential for a RC case study when conducting a life-cycle assessment*

The system boundaries included in this study comprise the amount of $CO_{2\text{-}eq}$ per kg emitted by producing the raw materials used in fabricating a commercialized cool roof used in ref. [134]. This section provides an estimate of the net change in GWP that occurs when the rooftops of the houses in Jamaica, Ghana, and Brazil (described in the previous section) are coated with the cool paint used in ref. [134]. This estimate considers the increase in GWP due to emissions that occur when manufacturing the cool paint. The estimate also considers the decrease in GWP that occurs due to the reduced building cooling load and due to the change in radiative forcing that occurs when the cool paint is applied to the rooftops. The system boundaries included in this study comprise the amount of $CO_{2\text{-}eq}$ per kg emitted by producing the raw materials used in fabricating a commercialized cool roof used in ref. [134]. This section provides an estimate of the net change in GWP that occurs when the rooftops of the houses in Jamaica, Ghana, and Brazil (described in

the previous section) are coated with the cool paint used in ref. [134]. This estimate considers the increase in GWP due to emissions that occur when manufacturing the cool paint. The estimate also considers the decrease in GWP that occurs due to the reduced building cooling load and due to the change in radiative forcing that occurs when the cool paint is applied to the rooftops.

To determine the GWP associated with the production of the cool paint it is first noted that three layers of paint are used for each rooftop. The weight of 1 L of cool paint is ~ 3 kg and it is assumed that 7.5 L are needed to cover a roof area of 36 $m^2$. Thus, for a three-layer coating of paint on a roof with an area of 36 $m^2$, 67.5 kg of cool paint are required. For a roof with an area of 90 $m^2$, 171 kg of cool paint is required to apply three layers. The ingredients used in the cool roof paint and their potential $CO_{2\text{-eq}}$ emissions are shown in Table 3.1.

*Table 3.1. The ingredients used in a cool roof and their global warming potential* [141].

| Ingredients | Weight (%) | GWP factor (kg $CO_{2\text{-eq}}$/kg of substance) |
|---|---|---|
| **Aqua ammonia** | ~1 | 2.11 [142] |
| **Propylene glycol** | ~5 | 4.14 [142] |
| **Acrylic polymer (PMMA*)** | ~25 | 3.75 [143] |
| **$CaCO_3$** | ~30 | 0.01 [142] |
| **ZnO** | ~5 | 2.91 [142] |
| **$TiO_2$** | ~5 | 1.43 [144] |
| **Water** | ~30 | 0.03 [142] |

* PMMA is considered as the acrylic polymer for the calculations.

Using the information provided in Table 3.1, the $CO_{2\text{-eq}}$ emissions associated with 171 kg and 67.5 kg of cool paint are 239 kg $CO_{2\text{-eq}}$ and 94 kg $CO_{2\text{-eq}}$, respectively. Also, it is assumed the cool roofs have a lifetime of 20 years, which is equivalent to the average service life of white reflective coatings [145]. Using the information provided in Table 3.1, the $CO_{2\text{-eq}}$ emissions associated with 171 kg and 67.5 kg of cool paint are 239 kg $CO_{2\text{-eq}}$ and 94 kg $CO_{2\text{-eq}}$, respectively. Also, it is assumed the cool roofs have a lifetime of 20 years, which is equivalent to the average service life of white reflective coatings [145].

Using the $CO_2$ emission factors for electricity production provided in [134], the $CO_2$ emission reductions due to the reduction in electric power consumption that is achieved when the cool roof is in operation were mentioned in Section 3.1, which are 13.5, 50, and 6 kg $CO_2 \cdot m^{-2} \cdot yr^{-1}$ in Ghana, Jamaica, and Brazil, respectively. Considering a 20-year period the total emissions saved for the houses in Jamaica, Ghana, and Brazil are estimated to be 36,000 kg $CO_{2\text{-eq}}$, 9,626 kg $CO_{2\text{-eq}}$, and 10,800 kg $CO_{2\text{-eq}}$, respectively. Using the $CO_2$ emission factors for electricity production provided in [134], the $CO_2$ emission reductions due to the reduction in electric power consumption that is achieved when the cool roof is in operation are 13.5, 50, and 6 kg $CO_2 \cdot m^{-2} \cdot yr^{-1}$ in Ghana, Jamaica, and Brazil, respectively. Considering a 20-year period the total emissions saved for the houses in Jamaica, Ghana, and Brazil are estimated to be 36,000 kg $CO_{2\text{-eq}}$, 9,626 kg $CO_{2\text{-eq}}$, and 10,800 kg $CO_{2\text{-eq}}$, respectively.

To determine the decrease in GWP due to LWIR emission from the cool paint (and the associated decrease in radiative forcing) it is assumed, for simplicity, that the addition of the cool paint increases the cooling power of the rooftops by 80 $W \cdot m^{-2}$. Equations 3.4 – 3.8 in Section 3.2.2 are used to calculate AGWP and GWP due to radiative forcing.

### *3.2.4. Determining the global warming impact when covering 1% of the Earth's surface with RC materials*

The materials are evaluated based on their $\bar{R}_{solar}$, $\bar{\varepsilon}_{LWIR}$, net outgoing power, RF, and GWP over 20 and 100 years. It is assumed that 1% of the Earth's surface is covered by the listed materials in Table 3.2 which reflect $\bar{R}_{solar}$ of the solar radiation of (163.3+22.9) $W \cdot m^{-2}$ incident on the Earth's surface and emit $\bar{\varepsilon}_{LWIR}$/95% of the radiation emitted to space through the atmospheric window (which is 40.1 $W \cdot m^{-2}$ as shown in Figure1). The remaining 99% of the Earth's surface remains the same and is assumed to have a radiative balance with outer space as depicted in Figure 1 (with RF = 0.6 $W \cdot m^{-2}$).

The equation for calculating the $RF$ at TOA when 1% of the Earth's surface is covered with material $i$ (herein defined as $RF_{i(1\%)}$) in this scenario is given by:

$$RF_{i(1\%)} = 1\% \times RF_i + 99\% \times RF_{Earth} \quad (3.9)$$

In this study, Equations 3.4 – 3.8 are utilized to calculate of $AGWP_{RCi}$ *(20)* $W \cdot m^{-2} \cdot yr \cdot kg^{-1}$, $AGWP_{RCi}$ *(100)* $W \cdot m^{-2} \cdot yr \cdot kg^{-1}$, $GWP_{RCi}$ *(20)* $W \cdot m^{-2} \cdot yr \cdot kg^{-1}$, and $GWP_{RCi}$ *(100)* $W \cdot m^{-2} \cdot yr \cdot kg^{-1}$.

*Table 3.2. Classification of the materials examined and their* $\bar{R}_{solar}$ *and* $\bar{\varepsilon}_{LWIR}$ *values.*

| | ***Structure*** | $\bar{R}_{solar}$ ***(%)*** | $\bar{\varepsilon}_{LWIR}$ ***(%)*** |
|---|---|---|---|
| **ID** | **RC Structures in Literature** | | |
| **I** | Pirvaram *et al*. [135] | 98.2 | 98.5 |
| **II** | Wang *et al*. [52] | 95 | 98 |
| **III** | Li *et al*. [87] | 96 | 78 |
| | **Common Construction Materials** | | |
| **IV** | White cement paste [146] | 66 | 93 |
| **V** | Road asphalt (ID A001) [147] | 21 | 96 |
| **VI** | Concrete (ID C002) [147] | 21 | 92 |
| **VII** | Grey cement (ID C005) [147] | 41 | 95 |
| | **Common Roofing Materials** | | |
| **VIII** | Roofing shingle (ID L003) [147] | 6 | 95 |
| **IX** | Ceramic roofing tile (ID R010) [147] | 19 | 95 |
| **X** | PVC roofing material (ID V002) [147] | 43 | 93 |
| | **Natural Surfaces** | | |
| **XI** | Forests [148] | 15 | 97 |
| **XII** | Oceans | 10 [149] | 98 [150] |
| | **Reference Cases** | | |
| **XIII** | Perfect RC | 100 | 100 |
| **XIV** | Perfect reflector | 100 | 0 |
| **XV** | Blackbody | 0 | 100 |

## 3.3. Results and discussion

### *3.3.1. Estimating the global warming potential for a RC case study when conducting a life-cycle assessment*

The AGWP and GWP due to radiative forcing, determined using the methods described in Section 3.2.1 and Section 3.2.2, are provided in Table 3.3.

*Table 3.3. Effects of using the cool paint on decreasing the radiative forcing.*

| Case study | | Jamaica (36 $m^2$) | Ghana (36 $m^2$) | Brazil (90 $m^2$) |
|---|---|---|---|---|
| **AGWP** | 20 years | $-1.12\times10^{-10}$ | $-1.12\times10^{-10}$ | $-2.8\times10^{-10}$ |
| ($W\cdot m^{-2}\cdot yr$) | 100 years | $-5.7\times10^{-10}$ | $-5.7\times10^{-10}$ | $-1.4\times10^{-9}$ |
| **GWP** | 20 years | -4,500 | -4,500 | -11,250 |
| ($kg_{CO2\text{-}eq}$) | 100 years | -6,264 | -6,264 | -31,140 |

Table 3.4 summarizes the change in GWP due to the addition of the cool paint to the rooftops for the case studies in Jamaica, Ghana, and Brazil.

*Table 3.4. The change in GWP due to the addition of cool paint for the three case studies in Jamaica, Ghana, and Brazil.*

| **Case study** | **Jamaica (36 $m^2$)** | **Ghana (36 $m^2$)** | **Brazil (90 $m^2$)** |
|---|---|---|---|
| **ΔGWP due to cool paint production** (kg $CO_{2\text{-}eq}$) | +94* | +94 | +239 |
| **ΔGWP due to reduced building cooling load** (kg $CO_{2\text{-}eq}$) | -36,000* | -9,626 | -10,800 |
| **ΔGWP due to change in radiative forcing** (kg $CO_{2\text{-}eq}$) | -4,500 | -4,500 | -11,250 |
| **Net ΔGWP** (kg $CO_{2\text{-}eq}$) | -40,406 | -14,032 | -21,811 |

* Signs of + and – show the emission and reduction of $CO_2$, respectively.

As shown by the estimates in Table 3.4, the GWP caused by cooling the house in Jamaica over a 20-year timeframe is reduced by ~ 40,000 kg $CO_{2\text{-}eq}$ by applying cool paint to the rooftop.

Likewise, the GWP for cooling the houses in Ghana and Brazil over a 20-year period are reduced by ~14,000 kg $CO_{2\text{-eq}}$ and ~22,000 kg $CO_{2\text{-eq}}$, respectively, by applying the cool paint. For the houses in Jamaica and Ghana the largest change in GWP achieved by the addition of the cool paint is due to the reduced building cooling load, whereas for the house in Brazil the largest change in GWP is due to the change in radiative forcing. This can be attributed to the fact that the $CO_2$ emission factor associated with electricity production in Brazil is low because hydropower comprises a large portion of the electric generation capacity in this region. This suggests that as electric power generation shifts towards cleaner production methods the change in GWP due to radiative forcing becomes the main contributor towards GWP reductions using RC technologies.

### *3.3.2. Analysis of net cooling power of RC materials and their associated global warming potential*

Figure 3.2 illustrates the Global Warming Potential relative to the net cooling power, $P_{net\ cooling,}$ of a surface, which provides valuable insights into the environmental benefits of using RC technologies to mitigate climate change impacts. The $GWP_{RCi}$ values plotted in the figure represent the Global Warming Potential per square meter of RC panel area over 20 years ($GWP_{RCi}\ (20)$) and 100 years ($GWP_{RCi}\ (100)$). The negative values of $GWP_{RCi}$ indicate a net reduction in $CO_{2eq}$ emissions. Starting from zero at zero cooling power, the $GWP_{RCi}$ values decrease linearly as cooling power increases. For example, a RC material structure of porous Poly (vinylidene fluoride-co-hexafluoropropylene) (PVDF-HFP) developed in reference [135] exhibits a solar reflectivity of $\bar{R}_{solar}$ = 98.2% and a long-wavelength infrared emissivity of $\bar{\varepsilon}_{LWIR}$ = 98.5%. Using the information obtained from Figure 3.1 and Equation 3.3, the $P_{net\ cooling}$, which is qual to - $RF_i$, is calculated 160.8 $W \cdot m^{-2}$ which leads to $GWP_{RCi}\ (20)$ = -252 $kgCO_{2\text{-eq}} \cdot m^{-2}$ and $GWP_{RCi}\ (100)$ = -333 $kgCO_{2\text{-eq}} \cdot m^{-2}$ using Equations 3.4 - Equations 3.8. The negative values of implies that 252 kg and 333 Kg of $CO_2$ emissions are offset by the cooling achieved by 1 $m^2$ of a surface with this cooling power over 20-year and 100-year timeframes, respectively.

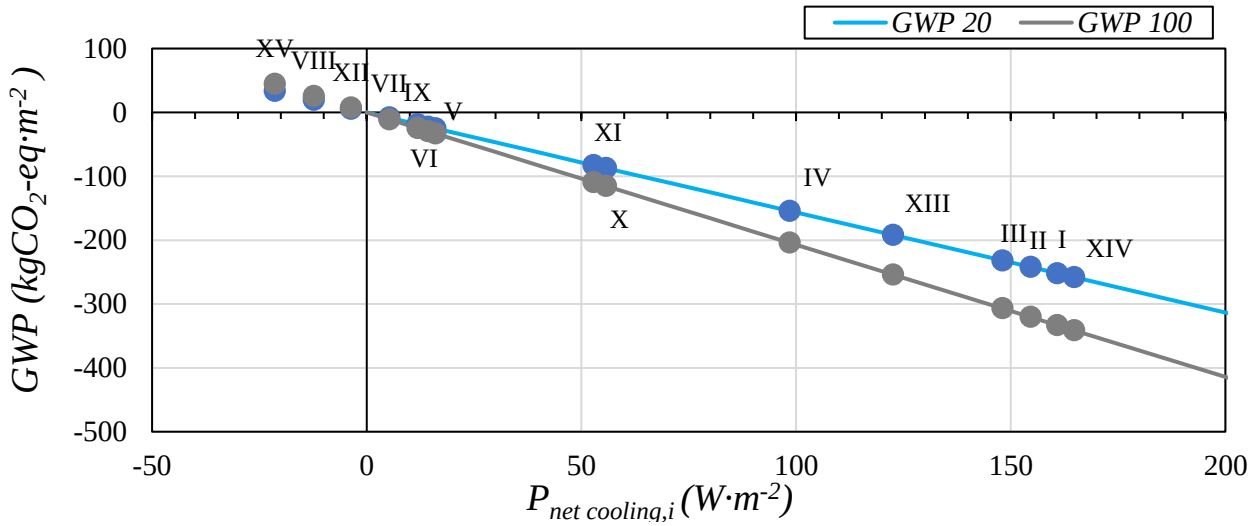


*Figure 3.2. Global warming potential as a function of cooling power for the materials listed in Table 1 with IDs: I = Pirvaram et al.* [135], *II = Wang et al.*[52], *III = Li et al.*[87], *IV = White cement paste, V = Road asphalt (ID A001), VI = Concrete (ID C002), VII = Grey cement (ID C005), VIII = Roofing shingle (ID L003), IX = Ceramic roofing tile (ID R010), X = PVC roofing material (ID V002), XI = Forests, XII = Oceans, XIII = Perfect RC, XIV = Perfect reflector, and XV = Blackbody .*

### *3.3.3. The global warming impact when covering 1% of the Earth's surface with a RC material.*

This section evaluates the environmental impact of substituting 1% of Earth's surface with the materials specified in Table 3.2. The optical properties of the materials outlined in Table 3.2 are used to calculate net outgoing power, RF, and GWP over 20 and 100 years, with the results summarized in Table 3.5 and displayed in Figure 3.3.

*Table 3.5. Net cooling power, global warming potential and radiative forcing associated with materials in Table 3.2.*

| ***Structure*** | $\bar{R}_{solar}$ ***(%)*** | $\bar{\varepsilon}_{LWIR}$ ***(%)*** | $P_{net,Cooling}$ ***(W·m$^{-2}$)*** | $GWP_{RCi}$ ***(20) kg$_{CO2\text{-}eq}$·m$^{-2}$*** | $GWP_{RCi}$ ***(100) kg$_{CO2\text{-}eq}$·m$^{-2}$*** | $RF_{1\%\_TOA}^{*}$ ***(W·m$^{-2}$)*** | $\Delta RF_{1\%\_TOA}^{**}$ ***(W·m$^{-2}$)*** |
|---|---|---|---|---|---|---|---|
| **Earth** | 12.3*** | 95 | -0.6 | 9.40E-01 | 1.24E+00 | 0.6 | 0 |
| **RC Structures in Literature** | | | | | | | |

| | | | | | | | |
|---|---|---|---|---|---|---|---|
| Pirvaram et al. [135] | 98.2 | 98.5 | 160.8 | -2.52E+02 | -3.33E+02 | -1.01 | -1.61 |
| Wang et al. [52] | 95 | 98 | 154.6 | -2.42E+02 | -3.20E+02 | -0.95 | -1.55 |
| Li et al. [87] | 96 | 78 | 148 | -2.32E+02 | -3.07E+02 | -0.89 | -1.49 |
| **Common Construction Materials** | | | | | | | |
| White cement paste [146] | 66 | 93 | 98.5 | -1.54E+02 | -2.04E+02 | -0.39 | -0.99 |
| Road asphalt (ID A001) [147] | 21 | 96 | 16 | -2.51E+01 | -3.32E+01 | 0.43 | -0.17 |
| Concrete (ID C002) [147] | 21 | 92 | 14.3 | -2.25E+01 | -2.97E+01 | 0.45 | -0.15 |
| Grey cement (ID C005) [147] | 41 | 95 | 52 | -8.28E+01 | -1.09E+02 | 0.066 | -0.534 |
| **Common Roofing Materials** | | | | | | | |
| Roofing shingle (ID L003) [147] | 6 | 95 | -12.3 | 1.93E+01 | 2.55E+01 | 0.72 | +0.12 |
| Ceramic roofing tile (ID R010) [147] | 19 | 95 | 11.9 | -1.86E+01 | -2.46E+01 | 0.48 | -0.12 |
| PVC roofing material (ID V002) [147] | 43 | 93 | 55.7 | -8.73E+01 | -1.15E+02 | 0.037 | -0.563 |
| **Natural Surfaces** | | | | | | | |
| Forests [148] | 15 | 97 | 5.3 | -8.26E+00 | -1.09E+01 | 0.54 | -0.06 |
| Oceans | 10 [149] | 98 [150] | -3.6 | 5.66E+00 | 7.49E+00 | 0.63 | +0.03 |
| **Reference Cases** | | | | | | | |
| Perfect RC | 100 | 100 | 164.8 | -2.58E+02 | -3.41E+02 | -1.05 | -1.65 |

| | | | | | | | |
|---|---|---|---|---|---|---|---|
| Perfect reflector | 100 | 0 | 122.6 | -1.92E+02 | -2.54E+02 | -0.63 | -1.23 |
| Blackbody | 0 | 100 | -21.4 | 3.35E+01 | 4.43E+01 | 0.81 | +0.21 |

* RF at TOA when 1% of the Earth's surface is covered with the material.

** $\Delta RF_{1\%} = RF_{1\%} - RF_{Earth}$ where $RF_{Earth}$ = 0.6 W·m$^{-2}$ at TOA.

*** The average surface albedo of the Erath is 22.9/186.2 = 12.3%

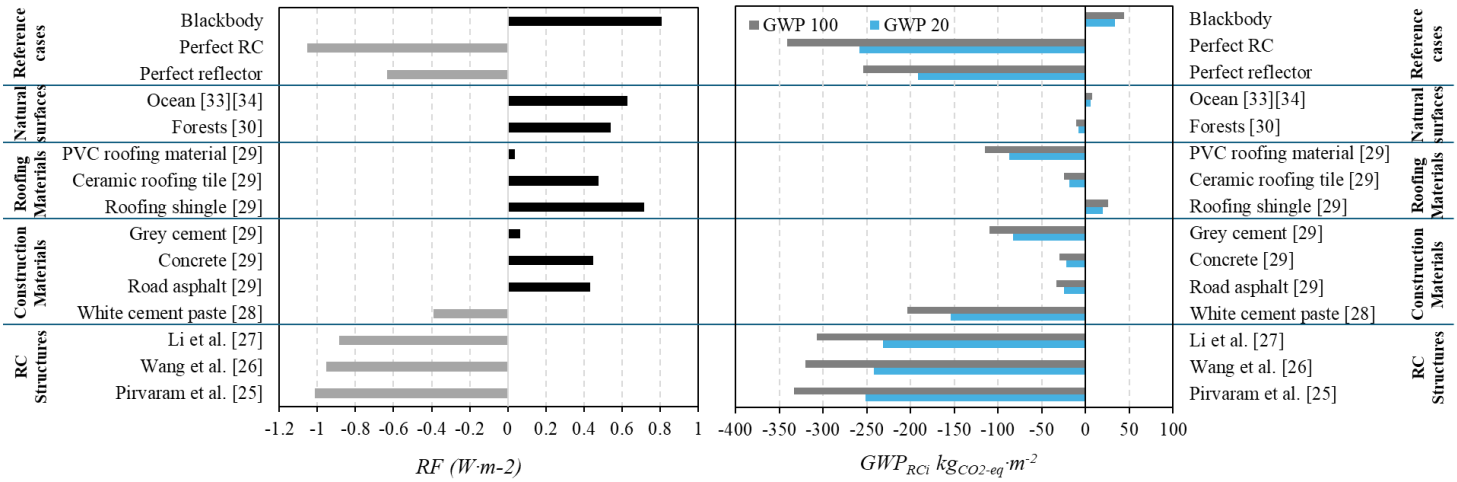


*Figure 3.3. Comparison of Radiative Forcing Values for Various Materials. Red bars indicate positive radiative forcing (RF) values, while sky blue bars represent negative RF values. The black dashed line ('Blackbody') signifies the upper limit, and the blue dashed line ('Perfect RC') denotes the lower limit.*

Of all surfaces considered the hypothetical case of the black body has the highest GWP values of GWP(20) = 33.5 $kgCO_{2\text{-}eq}\cdot m^{-2}$ and GWP(100) = 44.3 $kgCO_{2\text{-}eq}\cdot m^{-2}$. Although a blackbody emits the maximum amount of radiation over the atmospheric window, it also absorbs 100% of the incident solar radiation, which results in substantial heating overall. Indeed, as shown in Table 3.5, if 1% of the Earth's surface were covered with a material that had the properties of a black body, the RF at the TOA would increase from 0.6 to 0.81.

Notably, as shown in Table 3.5, only three types of surfaces would increase the GWP if they covered 1% of the Earth: Oceans, roofing shingles, and the hypothetical case of the blackbody. (Here, covering the Earth's surface with oceans refers to covering an area the size of 1 % of Earth's surface that has the average solar reflectance of 12.3% and long-wave infrared emissivity of 95%).

Ocean surfaces contribute to a slightly higher RF value than that for the average terrestrial surface. For roofing shingles GWP(100) = 25.5 $kgCO_{2\text{-}eq}\cdot m^{-2}$, where as for the average terrestrial surface GWP(100) = 1.24 $kgCO_{2\text{-}eq}\cdot m^{-2}$. It follows that on average GWP(100) increases by 24.3 $kgCO_{2\text{-}eq}\cdot m^{-2}$ when roofing shingles are used. If 1% of the Earth were to be covered with roofing shingles the corresponding increase in GWP(100) would be ~124 Gt $CO_{2\text{-}eq}$, which is more than thee times the amount of $CO_2$ emitted annually. Fortunately, as shown in Table 3.5, most construction and roofing materials have a positive net cooling effect and decrease GWP. Of the construction and roofing materials listed in Table 3.5 white cement paste is the best cooling material with $P_{net,cooling}$ = 98.5 $W\cdot m^{-2}$ and GWP(100) = -204 $kgCO_{2\text{-}eq}\cdot m^{-2}$. If 1% of the Earth's surface were to be replaced with white cement paste the RF at the TOA would decrease from 0.6 $W\cdot m^{-2}$ to -0.39 $W\cdot m^{-2}$, implying the Earth would experience global cooling.

The upper limit on the amount of cooling that could be achieved is set by the perfect RC material with $\bar{R}_{solar}$ = 100% and $\bar{\varepsilon}_{solar}$ = 100%. The net cooling power for this ideal material is 164.8 $W\cdot m^{-2}$ and if 1% of the Earth's surface were to be covered with a perfect RC the RF would decrease from 0.6 to -1.05. Remarkably, engineered RC materials with net cooling abilities very close to that of the perfect RC have been fabricated. Pirvaram et al. [25], Wang et al. [26], and Li et al. [27] fabricated porous polymeric RC films exhibiting cooling values of $P_{net,cooling}$ = 160.8 $W/m^2$, $P_{net,cooling}$ = 154.6 $W/m^2$ , and $P_{net,cooling}$ = 148 $W/m^2$, respectively. Covering 1% of the Earths surface with these materials would decrease the RF at the TOA to as low as -1.01 $W\cdot m^{-2}$.

Reducing GWP by changing the albedo of surfaces and using RC materials over large areas has been reported in the literature. Akbari et al. [151] investigated the effects of changing the albedo of surfaces of urban areas on a reduction in radiative forcing. They reported the emitted $CO_2$ offset for increasing roof albedo by 25% is equal to −64 $kgCO_{2\text{-}eq}\cdot m^{-2}$ of roof area. Similarly, for cool pavements with a proposed albedo difference of 0.15, the emitted $CO_2$ offset is equal to −38 $kgCO_{2\text{-}eq}\cdot m^{-2}$ of pavement area. Therefore, 16 $m^2$ of cool roof areas and 26 $m^2$ of cool paved areas are needed to offset 1 tonne of $CO_2$ emissions. Munday [152] suggested that if $5 \times 10^6$ $km^2$ in desert areas were to be covered with RC materials the terrestrial RF would be decreased by almost 1 $W\cdot m^{-2}$. In comparison, the GWP associated with the RC material fabricated by Pirvaram et al. [135] is -333 $kgCO_{2\text{-}eq}\cdot m^{-2}$, and if 1% of Earth's surface (which is ~ $5.1 \times 10^6$ $km^2$) were to be covered with this material the RF would decrease by 1.61 $W\cdot m^{-2}$ (from 0.6 to -1.01 $W\cdot m^{-2}$).

Achieving such a low RF value shows the potential for using these RC materials for practical applications in reducing urban heat island effects and lowering energy consumption in buildings. Notably, it has been reported that the global urbanized land area is ~ 3% of Earth's total land area [153].

RC materials can be applied in various areas across the Earth to cover 1% of its surface area. These areas can be generally categorized into urban, rural, industrial, and natural environments, each with unique potential for applying RC materials to make a positive environmental impact. Urban areas are prime locations for RC applications due to their high population density, extensive infrastructure, and significant contribution to urban heat islands. Rooftops of residential, commercial, and industrial buildings can be coated with RC materials to reduce cooling energy demands. Building walls and vertical surfaces in urban areas could also supplement horizontal rooftops. Coating walls would expand the application area in dense cities with limited roof space. The global rooftop area is estimated to be around 0.25 million $km^2$ in 2020 out of the total human-made built-up surface area of 1.46 million $km^2$ [154]. This equates to about 0.05% of Erath's surface area. Another potential location to apply the cooling materials and RC is roadways and pavements. The total global pavements and roadways area is estimated to be 21 million $km^2$ which is calculated to be 4.1% of the Earth's surface area. Some reflective films and RC materials can also be floated on reservoirs, lakes, or ocean surfaces to supplement land coverage. Deserts and arid areas are another strategy to be vastly used for this purpose due to the low risk of land use conflicts.

One limitation of this study is the calculations were carried out using surface albedo and emissivity values measured at normal incidence. While these measurements provide useful insights, they do not account for the full angular dependence of radiative properties. It is important to note that these values may not fully capture the angular dependence of radiative properties. The solar reflectance (albedo) and long-wave IR emissivity can both vary significantly with the angle of incidence. As the angle between incident solar radiation and the normal to a surface increases, solar reflectance generally increases, leading to less absorption of solar energy. On the other hand, long-wave IR emissivity may also exhibit angular dependence, with emissivity often increasing as the angle of emission approaches the normal direction [155]. For a more detailed analysis, future work could

consider hemispherical optical properties measured at different angles. This would provide a broader understanding of how surface reflectivity and emissivity vary, though the current results still offer valuable insights.

Another limitation is that the use of RC materials cannot be a permanent solution to greenhouse gas emissions. Similarly to SRM technologies, geoengineering via widespread RC can contribute to mitigating global warming and minimizing damage to ecosystems but will not address the underlying causes of global warming. Largescale RC will not be able to offset increases in global warming if greenhouse gas emissions continue to rise. Nevertheless, RC can play an important role in alleviating the effects of global warming while solutions that address the root causes of global warming are developed. To address global warming nations are transitioning to clean energy sources and developing carbon capture technologies [156][157][158]. However, almost half of the $CO_2$ that has already been emitted will stay in the atmosphere for centuries and will contribute to global warming over extended time periods [159][160]. RC technologies can play a vital role in "buying time" by offsetting radiative forcing caused by greenhouse gas emissions while permanent solutions for global warming are being developed and implemented.

## 3.4. Conclusion

This chapter analyses RC materials in comparison with conventional construction and roofing materials and highlights their significant potential in mitigating global warming. The study reveals that RC materials with high solar reflectivity and long-wavelength infrared emissivity can notably reduce radiative forcing and global warming potential. Among the materials evaluated, those developed by Pirvaram et al. [135], Wang et al. [52], and Li et al. [87] exhibit notable cooling efficiencies and significant reductions in radiative forcing. The results suggest that covering 1% of the Earth's surface with high-performance RC materials could offset a considerable amount of anthropogenic $CO_2$ emissions, offering a practical approach to climate change mitigation. For example, the RC material developed by Pirvaram et al. demonstrates exceptional performance with a $\bar{R}_{solar}$ of 98.2% and a $\bar{\varepsilon}_{LWIR}$ of 98.5%. This material achieves a net cooling power of 160.8 $W \cdot m^{-2}$, leading to a GWP of -252 $kgCO_2\text{-}eq \cdot m^{-2}$ over 20 years and -333 $kgCO_2\text{-}eq \cdot m^{-2}$ over 100 years. Its RF value is -1.01s $W \cdot m^{-2}$ when covering 1% of the Earth's surface, indicating a

substantial reduction in radiative forcing compared to conventional materials. These results are closely comparable with the perfect RC as the benchmark for performance (with $\bar{R}_{solar}$= $\bar{\varepsilon}_{LWIR}$= 100%), which shows a net outgoing power of 164.8 W·m$^{-2}$ and achieves the highest reduction in radiative forcing (RF = -1.05 W·m$^{-2}$). On the other hand, roofing shingles (ID L003 [147] with $\bar{R}_{solar}$ of 6% and $\bar{\varepsilon}_{LWIR}$ of 95%) shows the least favorable environmental impact among the materials analyzed. It sets a net cooling power of -12.3 W·m$^{-2}$ and a GWP of 193 kg$CO_2$-eq·m$^{-2}$ over 20 years and 255 kg$CO_2$-eq·m$^{-2}$ over 100 years. The RF value for roofing shingle (ID L003) [147] is 0.72 W·m$^{-2}$ when 1% of the Earth's surface is covered, indicating a positive contribution to radiative forcing and increasing global temperatures. The results emphasize that engineered RC materials offer superior cooling efficiency and potential for global warming mitigation, closely approaching the ideal perfect RC benchmark. In contrast, roofing shingles, along with other conventional materials like concrete and road asphalt, contributes positively to radiative forcing, highlighting their environmental drawbacks. The findings of this work underscore the importance of incorporating RC materials into sustainable building practices and climate mitigation strategies.

# Chapter 4

## 4. Utilizing underside reflectors in RC technology

### 4.1. Introduction

The atmospheric transmittance generally decreases with increasing zenith angle because the pathlength of light through the atmosphere increases with increasing zenith angle, resulting in increased atmospheric absorption [161]. Therefore, objects with surface areas that have their normal directions pointing straight upwards (e.g., a zenith angle of 0°) can be cooled to a greater extent. However, limited sky-facing area is one of the big challenges preventing widespread use of RCs for multistorey and high-rise buildings in cities [19]. Furthermore, research on RCs reported in the literature has primarily focused on RC from the top sky-facing surfaces of objects while cooling contributions from the other surfaces, especially the bottom surfaces, has mostly been neglected. This is because in most cases the underside of an object being cooled is insulated and radiatively inactive.

Recently, Peoples *et al*. [162] employed a RC combined with a mid-infrared (mid-IR) V-shaped reflector. In their study, a RC coated with a $BaSO_4$ paint is placed on a mid-IR reflector to emit radiation to outer space from both the top and bottom surfaces of the RC, simultaneously. The

results show the temperature reduction can be doubled when the RC was used with the IR reflector when compared to the standalone RC. In another study, Zhou *et al*. [163] used a RC configured as a vertically aligned emitter surrounded by a V-shaped spectrally selective mirror. These mirrors absorbed the incident solar radiation while reflecting thermal radiation from the RC. Using this RC structure, cooling to 14 ˚C below atmospheric temperature was achieved under standard atmospheric pressure.

In this chapter, the effects of placing perfectly specular reflectors (i.e., specular reflectance equals 1) on the performance of the RCs are numerically investigated. A disk-shaped RC, which radiates over the atmospheric window, is positioned atop six distinct underside surfaces (Figure 4.1). These comprise three flat surfaces: a surface with an infinite expanse that has the properties of a blackbody, a reflector with an infinite expanse, and a reflector with a 1 m diameter located above a surface with an infinite expanse and the properties of a blackbody. Additionally, there are three parabolic dishes, each with unique geometric characteristics. Parabolic structures enhance the cooling performance of the disk-shaped RC by directing the thermal radiation it emits towards the zenith angle, where atmospheric transmittance is the highest, while blocking atmospheric radiation at incident angles that are far from the zenith. The results show that among the configurations being investigated in this work, the highest cooling performance is achieved when the RC resides at the focal length of a parabolic dish that has an entrance aperture with a surface area of 0.13 $m^2$, the focal length of 0.016 m, and height of 0.625 m. For this case the RC temperature can be cooled to 229 K for the ideal case when the RC is a selective emitter and the convective heat transfer from the surrounding environment and incident solar radiation is zero. In comparison, if an infinitely wide flat plate is used as the underlying reflector instead of the parabolic dish, the temperature of the RC increases to 243 K. This work also presents a comprehensive study of the effects of the convective heat transfer coefficient, $h$, the absorbed solar radiation, $\alpha_{solar}$, and the atmospheric temperature, $T_{atm}$, on the performance of the RC. The results show that it is most important to increase the reflectivity of solar radiation to achieve effective diurnal cooling under practical conditions [136].

## 4.2. Methods

### *4.2.1. Description of the radiative cooling structures investigated*

In this study, numerical analysis is carried out in three dimensions to investigate the effects of using an underside reflector on the extent to which a RC is cooled. A point source RC is evaluated in six different configurations, as shown in Figure 4.1. In Case 1 (shown in Figure 4.1a) a flat surface with infinite width and the properties of a blackbody is located beneath the RC as a reference case. In Case 2 (Figure 4.1b) the RC is above a flat reflective surface that extends to infinity in the planar direction. For Case 3 (Figure 4.1c) a flat circular reflector with a width of 1 m resides at a distance of 0.1 m beneath the RC. For Cases 4, 5, and 6 (shown in Figures 4.1d, 4.1e, and 4.1f, respectively) the RC is situated at the focal length of a parabolic reflective dish whose surface can be described using the equation $z = (x^2 + y^2)/(4f)$, where $x$, $y$, $z$ and are labeled in Figures 4.1d-f and the focal length, $f$ , is given. For Case 4: -0.2 m < $x$ < 0.2 m, $f$ = 0.1 m, and the height (H) = 0.1 m. For Case 5: -0.5 m < $x$ < 0.5 m, $f$ = 0.1 m, $H$ = 0.625 m. For Case 6: -0.2 m < $x$ < 0.2 m, $f$ = 0.016 m, and H = 0.625 m. The reflective surfaces are considered to be perfectly specular reflectors (reflectivity $\rho$ = 1) for all wavelengths. For all cases two different emittance spectra are considered when determining the radiation emitted from the RC material structure and radiation received from the atmosphere, and these spectra are shown in Figure 4.2. The first emittance spectrum is that of an ideal top-hat selective radiator which has an emittance of 1 over the atmospheric window from 8 to 13 μm and an emittance of zero for wavelengths outside this range. The second emittance spectra considered, which is that of an ideal step-function broadband radiator, has an emittance of zero for wavelengths less than 4 μm and an emittance of one for wavelengths greater than 4 μm. Henceforth in this chapter, the investigated cases will be represented as follows: Case 1 will be referenced as Case 1 (Blackbody), Case 2 will adopt the notation of Case 2 (infinite flat), Case 3 will be indicated by Case 3 (1m flat), Case 4 will be denoted by the notation Case 4 (Para. $f$0.1 H0.1) possessing the focal point of 0.1 m and height of 0.1 m, Case 5 will be represented as Case 5 (Para. $f$0.1 H0.625), and Case 6 will be conveyed using the notation Case 6 (Para. $f$0.016 H0.625).

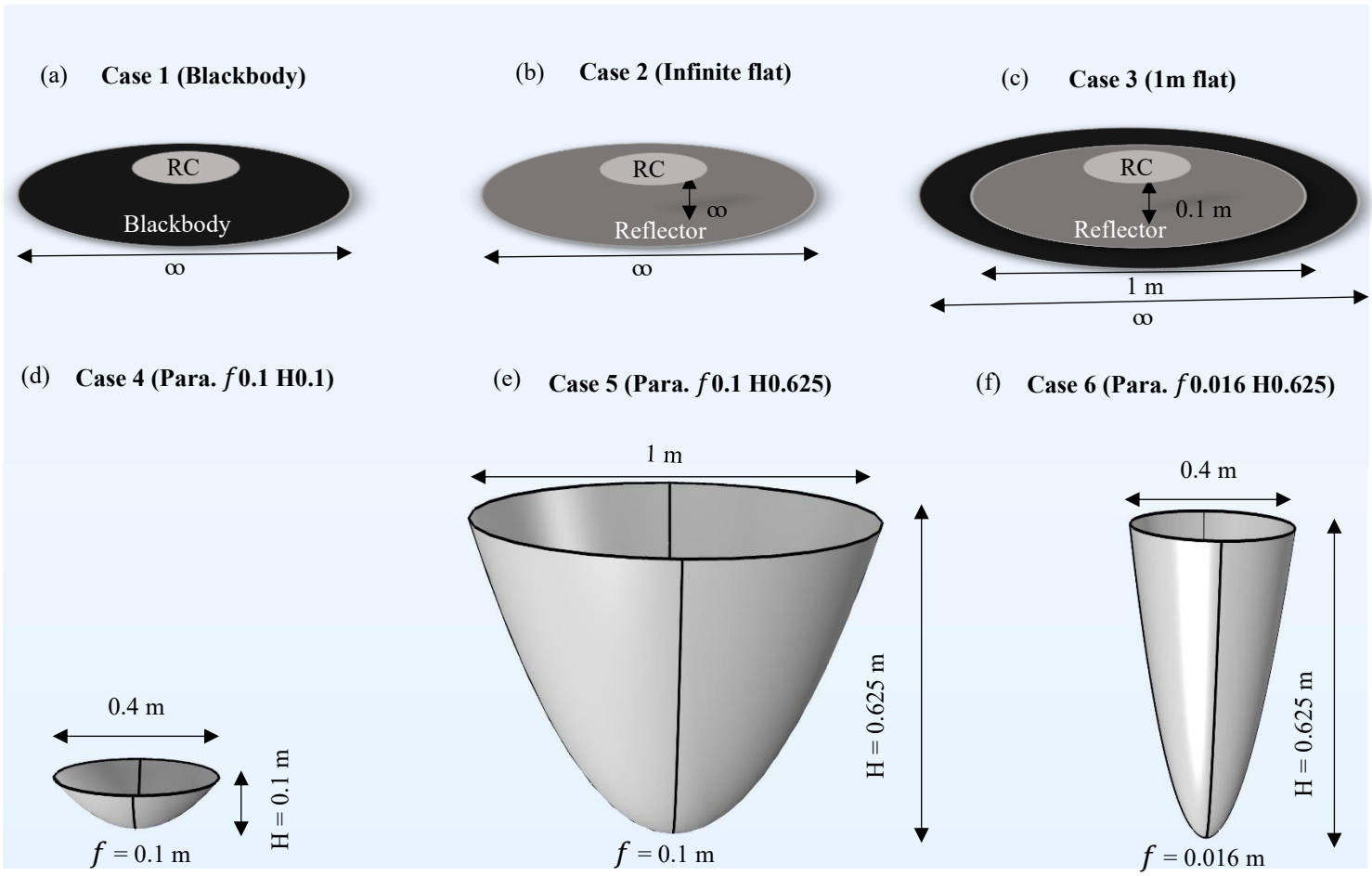


*Figure 4.1 Schematic of the RC with an underlying surface that is (a) Case 1 with a blackbody undersurface, (b) Case 2 using an infinite flat reflector, (c) Case 3 employing a reflector of 1 m width, (d) Case 4 (Para. f0.1 H0.1), (e) Case 5 (Para. f0.1 H0.625), and (f) Case 6 (Para. f0.016 H0.625) evaluated in this study.*

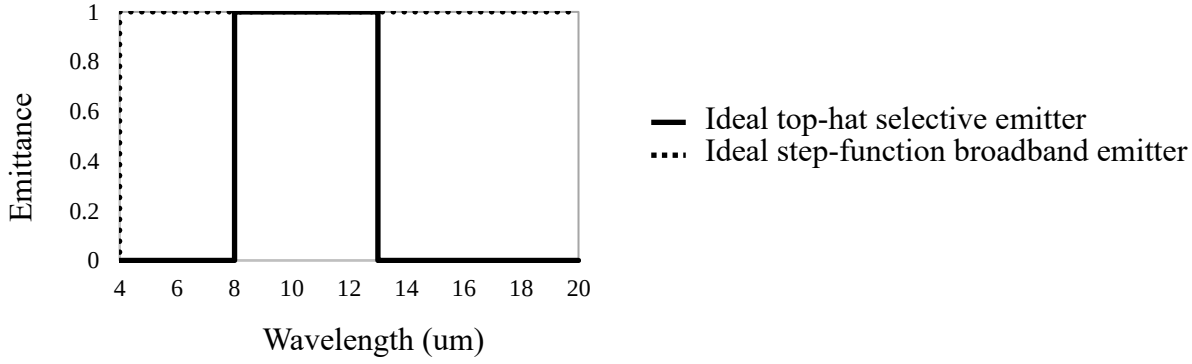

*Figure 4.2 Emittance spectra for an ideal top-hat selective emitter and for an ideal step-function broadband emitter.*

### *4.2.2. Monte Carlo Ray Tracing*

In the Monte Carlo simulation method developed in this work, 1,000,000 rays are generated randomly from different points on the RC surface. Each ray is assigned a specific direction based on the geometry of the system and the properties of the RC. The rays are then emitted in these directions and interact with surrounding surfaces. When a ray strikes the parabolic dish, which is 100% reflective, it is reflected towards the opening aperture area. Rays that reach the aperture are considered to be radiated into the sky. In some cases, rays are reflected back to the RC surface after interacting with the dish or other surrounding surfaces.

The interactions of the rays are tracked, and data is collected on the angles of emission and the angles at which they reach the aperture area. This data allows for the assessment of the radiative heat transfer and the distribution of emission angles. The number of rays that exit through the aperture area is recorded as a key indicator of the cooling performance, representing the amount of heat radiated away from the RC.

MATLAB is used to write the code for the simulation, enabling efficient tracking of the rays and their interactions. Statistical analysis is employed to ensure that the random nature of the ray propagation and interactions is accurately captured. The large number of rays used in the simulation provides a reliable estimate of the system's behavior over time, enabling the evaluation of the radiative cooling performance of the RC and parabolic dish configuration.

### *4.2.3. Cooling performance calculations*

For a planar sky-facing RC that is perfectly insulated at its bottom side (Figure 3a), the net cooling power ($P_{\text{Cooling}}$) can be calculated as a function of the temperature of the RC ($T_{RC}$) and the temperature of the atmosphere ($T_{atm}$) by using Equation 4.1 [164]:

$$P_{\text{Cooling}} = P_{RC}\,(T_{RC}) - P_{atm}(T_{atm}) - P_{\text{Solar}} - P_{Nonrad}\,(T_{RC}, T_{atm}) \tag{4.1}$$

Here, $P_{RC}$ is the outgoing power radiated by the RC, $P_{atm}$ is the incoming atmospheric radiation absorbed by the RC, $P_{\text{Solar}}$ represents the incoming absorbed solar irradiance, and $P_{Nonrad}$ is the nonradiative heat exchange (i.e. heat transferred via convection and conduction) with the surrounding environment. Note that $P_{Nonrad}$ is positive when heat is transferred from the surroundings to the RC system, which is the case for sub-ambient cooling. The following equations are used to obtain the parameters shown in Equation 4.1 [1], [2], [4][52]:

$$P_{RC}\,(T_{RC}) = A\,2\pi \int_0^{\frac{\pi}{2}} \sin\theta cos\theta \int_0^{\infty} I_{BB}(T_{RC},\lambda)\,\varepsilon_{RC}\,(\lambda)\,d\lambda\,d\theta \tag{4.2}$$

$$P_{atm}\,(T_{atm}) = A\,2\pi \int_0^{\frac{\pi}{2}} \sin\theta\, cos\theta \int_0^{\infty} I_{BB}(T_{atm},\lambda)\,\varepsilon_{RC}\,(\lambda)\,\varepsilon_{atm}\,(\lambda,\theta)d\lambda\,d\theta \tag{4.3}$$

$$P_{\text{Solar}} = A \int_0^{\infty} G_{AM1.5}\,\varepsilon_{RC}\,(\lambda)\,d\lambda \tag{4.4}$$

$$P_{Nonrad} = A\,h\,(T_{atm} - T_{RC}) \tag{4.5}$$

In these equations $A$ is the area of the top surface of the radiator, $\lambda$ represents the wavelength of radiation, and $I_{BB}$ is the spectral intensity of a blackbody, which can be obtained using Plank's law:

$$I_{BB}(T,\lambda) = \frac{2hc^2}{\lambda^5}\ \frac{1}{e^{h_p c/(\lambda k_B T)} - 1} \tag{4.6}$$

in which $h_p$ is Planck's constant, $k_B$ is the Boltzmann constant, and $c$ is the speed of light in vacuum. $\varepsilon_{RC}\,(\lambda)$ is the spectral emittance of the radiator which is considered to be independent of the direction. $\varepsilon_{atm}\,(\lambda,\theta)$ is the spectral directional emittance of the atmosphere and can be obtained as follows [52]:

$$\varepsilon_{atm}\,(\lambda,\theta) = 1 - \tau\,(\lambda)^{1/\cos\theta} \tag{4.7}$$

In which $\tau\,(\lambda)$ is the spectral atmospheric transmittance in the normal direction. In this work, the entire atmospheric layer, from ground to outer space, is modeled as a unified medium. Consequently, the ambient temperature is employed as a substitute for the variable temperature, which inherently fluctuates with altitude. $\tau\,(\lambda)$ is also obtained using ATRAN [165] (a software computing the spectral

transmittance of Earth's atmosphere in different locations) for Toronto, Canada. Also, the effects of radiation reflected from the atmosphere on the cooling performance of the RC are neglected.

$G_{AM1.5}$ is the solar air mass 1.5 (AM1.5) irradiance spectrum, however, in this work the solar irradiance is assumed to have a constant value of 1000 W·m$^{-2}$. $h$ represents the convective heat transfer coefficient.

For Cases 1, 2 and 3 the cooling performance is evaluated under the assumption that the RC is a point source. For Case 1 (Blackbody surface beneath the RC), in the angular range of $0 < \theta < \frac{\pi}{2}$ shown in Figure 4.3a, the RC radiates thermal energy towards sky while over $\frac{\pi}{2} < \theta < \pi$ the RC exchanges thermal emission with Earth (an underside object which is considered to have blackbody properties). Therefore, to facilitate the calculations, the outgoing radiative power from the RC is divided into two components:

$$P_{RC} = P_{RC-sky} + P_{RC-Earth} \tag{4.8}$$

In which, $P_{RC-sky}$ is the power radiated directly towards the sky and $P_{RC-Earth}$ is the radiative power exchange of the RC with the Earth, respectively, and can be obtained as below:

$$P_{RC-sky} = 2\pi A \int_0^{\frac{\pi}{2}} \sin\theta cos\theta \int_0^{\infty} (I_{BB}(T_{RC}, \lambda) - I_{sky}(T_{sky}, \lambda))\, \varepsilon_{RC}(\lambda)\, \varepsilon_{sky}(\lambda) d\lambda\, d\theta \tag{4.9}$$

And,

$$P_{RC-Earth} = 2\pi A \int_{\frac{\pi}{2}}^{\pi} \sin\theta cos\theta \int_0^{\infty} (I_{BB}(T_{RC}, \lambda) - I_{BB}(T_{Earth}, \lambda))\, \varepsilon_{RC}(\lambda)\, \varepsilon_{Earth}(\lambda) d\lambda\, d\theta \tag{4.10}$$

In light of $T_{sky}$ being approximately 2 K, the term $I_{sky}(T_{sky}, \lambda)$ is omitted from the equations, with $\varepsilon_{sky}(\lambda)$ assumed to be 1.

For Case 2, since the RC is located above a flat reflector that extends to infinity in the planar directions, the heat exchange with the surroundings from the bottom side is the same as that of the upper side. Therefore, the values attained from Equations 4.2 to 4 for $P_{RC}$, $P_{atm}$, $P_{solar}$, and $P_{nonrad}$, are doubled.

For Case 3, when using a disk-shaped underside reflector with radius, *r*, the amount of radiation emitted from the RC in the downwards direction that is reflected to the sky depends on the size of the reflector. That is, in addition to the radiation emitted from the upper surface of the RC to the sky over the range $0 < \theta < \frac{\pi}{2}$, radiation emitted from the bottom side of the RC over the range $\frac{\pi}{2} + \tan^{-1}\frac{d}{r} \cdot \frac{\pi}{180} < \theta < \pi$ is reflected towards the sky by the underlying reflector (see Figure 4.3c). Moreover, for Case 3, for directions over the range $\frac{\pi}{2} < \theta < \frac{\pi}{2} + \tan^{-1}\frac{d}{r} \cdot \frac{\pi}{180}$ the RC exchanges radiative heat with Earth which is considered to have the optical properties of a blackbody. In addition to reflecting radiation emitted from the bottom of the RC disk to the sky, the underlying reflector also reflects incoming radiation from the atmosphere onto the bottom side of the RC. Based on the dimensions of the reflector, the RC, and the distance between the two, atmospheric radiation incident from a certain angular range can be reflected to the bottom side of the RC. Therefore, the Equations for $P_{RC-sky}$, $P_{RC-Earth}$ and $P_{atm}$ are revised for Case 3 as shown below in Equations 4.11 through 4.13:

$$P_{RC-sky} = 2\pi A \left( \int_0^{\frac{\pi}{2}} \sin\theta cos\theta d\theta + \int_{\frac{\pi}{2}+\tan^{-1}\frac{d}{r}\cdot\frac{\pi}{180}}^{\pi} \sin\theta cos\theta d\theta \right) \int_0^{\infty} I_{BB}(T_{RC},\lambda)\, \varepsilon_{RC}(\lambda)\, d\lambda \tag{4.11}$$

$$P_{RC-Earth} = 2\pi A \int_{\frac{\pi}{2}}^{\frac{\pi}{2}+\tan^{-1}\frac{d}{r}\cdot\frac{\pi}{180}} \sin\theta cos\theta\, d\theta \int_0^{\infty} (I_{BB}(T_{RC},\lambda) - I_{BB}(T_{Earth},\lambda))\, \varepsilon_{RC}(\lambda)\, \varepsilon_{Earth}(\lambda)\, d\lambda \tag{4.12}$$

$$P_{atm} = 2\pi A \left( \int_0^{\frac{\pi}{2}} \sin\theta cos\theta d\theta \int_0^{\infty} I_{BB}(T_{atm},\lambda)\, \varepsilon_{RC}(\lambda)\, \varepsilon_{atm}(\lambda,\theta)\, d\lambda + \int_{\frac{\pi}{2}+\tan^{-1}\frac{d}{r}\cdot\frac{\pi}{180}}^{\pi} \sin\theta cos\theta d\theta \int_0^{\infty} I_{BB}(T_{atm},\lambda)\, \varepsilon_{RC}(\lambda)\, \varepsilon_{atm}(\lambda,\theta)\, d\lambda \right) \tag{4.13}$$

or Cases 4, 5, and 6, the RC resides at the focal length of a parabolic reflector (Figure 4.3d) and results are compared for when its radius is $r_{RC}$ = point source, $r_{RC}$ = 0.0125 m and $r_{RC}$ = 0.025 m. To attain the

results for when the RC is a point source in Cases 4, 5, and 6, $r_{RC}$ was set to a small value (0.001 m) and simulations were carried out to verify the results did not change significantly when $r_{RC}$ was set to lower values (for example the same results were attained when $r_{RC}$ = 0.001 m and when $r_{RC}$ = 0.0001 m). In parabolic dishes, an essential parameter is the rim angle, denoted as the angle formed between the parabolic axis and the line connecting its focal length to the entrance aperture edges. In this study, $\theta_s$ is introduced as the supplementary angle to the rim angle. This parameter, $\theta_s$, is employed to directionally assess the radiative heat exchange between the parabolic dishes and their environment. (Figure 4.3e). For Cases 4 to 6, over the angles $0 < \theta < \theta_s$ the RC directly exchanges radiation with the sky, however, over the range $\theta_s < \theta < \pi$, thermal radiation emitted by the RC is directed towards the sky after being reflected by the inner surface of the parabolic dishes. Furthermore, when the RC is not a point source, radiation emitted in the same direction but from different points on the RC disk will travel in slightly different directions after being reflected by the inner surface of the parabolic dish (see Figure 4.3f). Thus, radiation emitted from points on the RC that are offset from the focal length will be directed towards the atmosphere at an angle of $0 < \psi < \psi_d$, where $\psi_d$ is the maximum possible deviation from the zenith which occurs when radiation is emitted from the edge of the RC structure.

To determine the cooling power of the RC for Cases 4, 5, and 6, a MCRT code is developed to capture the angular distribution of rays emitted to the sky. This code captures both the radiation emitted directly form the RC at angles of $\theta$ and the rays travelling towards the sky at a zenith angle of $\psi$ after being reflected from the surface of the parabola. To determine the angular distribution 1,000,000 rays are emitted from random points on the RC into random directions and the trajectory of the rays are traced until they are absorbed or emitted to outer space. The RC material and the fictitious top surface of the entrance aperture which represents the sky are considered perfect absorbers with emittance ($\varepsilon$) of 1 and the reflectors are assumed to specularly reflect the rays without any losses. The fractions of diffuse rays leaving the RC and propagating into the sky with a zenith angle between δ and γ radians is denoted as ($F_{emit\delta-\gamma}$). That is, $F_{emit\delta-\gamma}$ accounts for all rays leaving the RC and reaching the sky (either directly or via any intervening specular reflections by the parabolic dish) for which the angle between the vertical direction and the direction the rays are propagating towards the sky in is greater than δ rad and less than γ rad. In this work the fraction of rays emitted for increments of the zenith angle of 10° ($\frac{\pi}{18}$ rad) are determined (e.g. $F_{emit0-\frac{\pi}{18}}$, $F_{emit\frac{\pi}{18}-\frac{\pi}{9}}$, …, $F_{emit\frac{17\pi}{18}-\pi}$) to calculate the radiative power emitted to the sky, $P_{RC-sky}$, for Cases 4, 5, and 6 using Equation 4.14:

$$P_{RC-sky} = 2\pi A \left( \frac{F_{emit 0-\frac{\pi}{18}}}{F_{R0-\frac{\pi}{18}}} \int_0^{\frac{\pi}{18}} \sin\theta cos\theta d\theta + \frac{F_{emit \frac{\pi}{18}-\frac{\pi}{9}}}{F_{R\frac{\pi}{18}-\frac{\pi}{9}}} \int_{\frac{\pi}{18}}^{\frac{\pi}{9}} \sin\theta cos\theta d\theta + \cdots + \frac{F_{emit \frac{17\pi}{18}-\pi}}{F_{R\frac{17\pi}{18}-\pi}} \int_{\frac{17\pi}{18}}^{\pi} \sin\theta cos\theta d\theta \right) \int_0^{\infty} I_{BB}(T_{RC}, \lambda)\, \varepsilon_{RC}(\lambda)\, d\lambda \quad (4.14)$$

where $F_{R\delta-\gamma}$ is the fraction of rays emitted from the RC and reaching the sky for the reference case when the parabolic dish is not present (e.g., Case 1 in Figure 4.1) in directions that have zenith angles between δ rad and γ rad.

Considering the reciprocity theorem, the angular distribution of rays emitted from the RC to the atmosphere is the same as the angular distribution of incoming radiation the RC receives from the atmosphere. Thus, the MCRT method described above to attain $P_{RC-sky}$ can also be used to calculate the amount of radiant power the RC receives from the atmosphere, and $P_{atm}$ is determined using Equation 4.15:

$$P_{atm} = 2\pi A \left( \frac{F_{refl 0-\frac{\pi}{18}}}{F_{R0-\frac{\pi}{18}}} \int_0^{\frac{\pi}{18}} \sin\theta cos\theta d\theta \int_0^{\infty} I_{BB}(T_{atm}, \lambda)\, \varepsilon_{RC}(\lambda)\, \varepsilon_{atm}(\lambda, \theta)\, d\lambda + \frac{F_{ref \frac{\pi}{18}-\frac{\pi}{9}}}{F_{R\frac{\pi}{18}-\frac{\pi}{9}}} \int_{\frac{\pi}{18}}^{\frac{\pi}{9}} \sin\theta cos\theta d\theta \right.$$
$$\left. \cdots + \frac{F_{ref \frac{17\pi}{18}-\pi}}{F_{R\frac{17\pi}{18}-\pi}} \int_{\frac{17\pi}{18}}^{\pi} \sin\theta cos\theta d\theta \int_0^{\infty} I_{BB}(T_{atm}, \lambda)\, \varepsilon_{RC}(\lambda)\, \varepsilon_{atm}(\lambda, \theta) d\lambda \right) \quad (4.15)$$

where $F_{refl 0-\frac{\pi}{18}}$ is the fraction of reflected rays from the parabolic reflectors towards the sky in the angle range of $0 - \frac{\pi}{18}$.

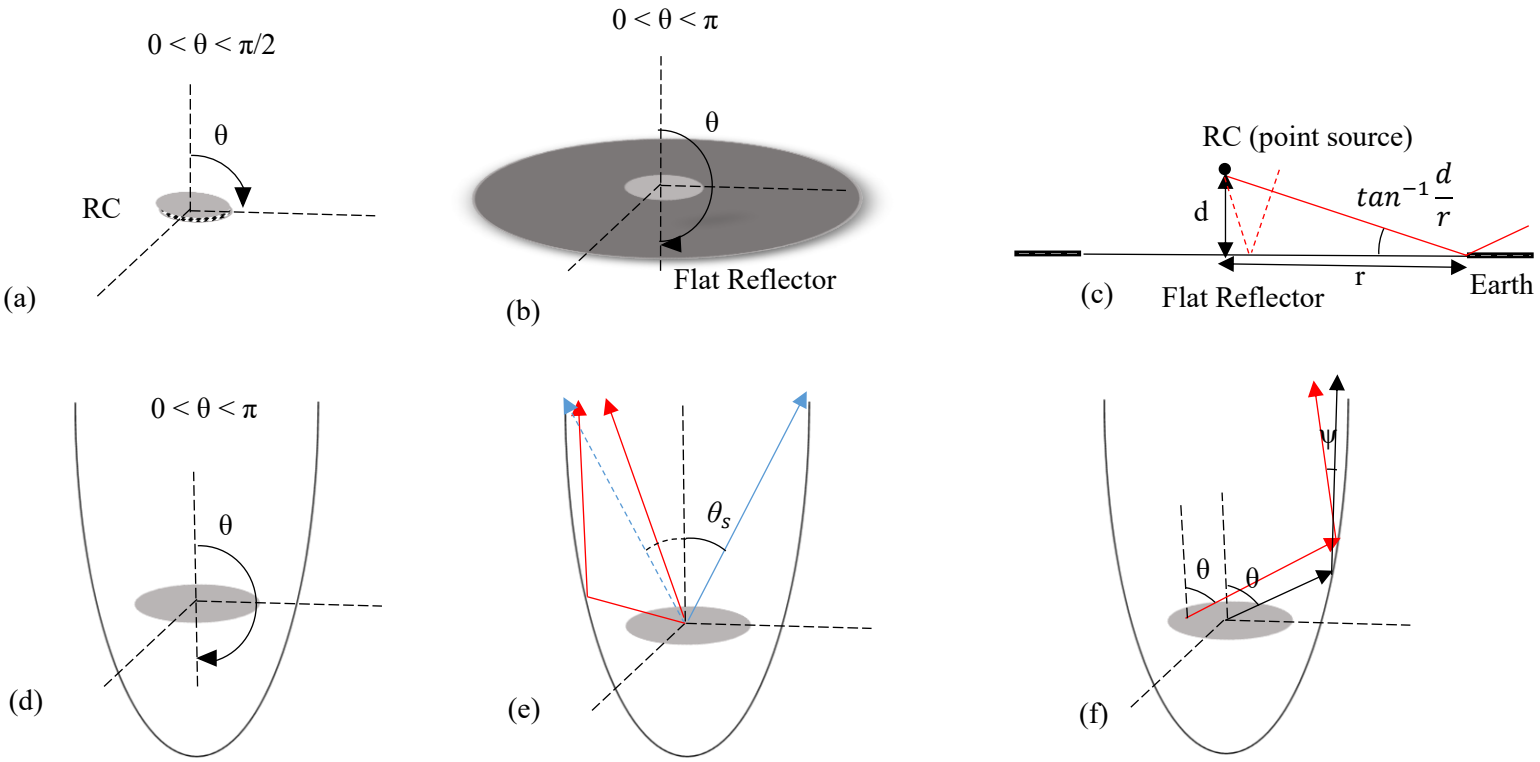


*Figure 4.3 (a) an insulated RC material from bottom side, (b) using a flat reflector undersurface to reflect the bottom side radiation to the sky, (c) geometrical features of a finite 1m flat reflector undersurface, (d) using a parabolic reflector to normally direct the radiation to the sky, (e) the supplementary angle to the rim angle, $\theta_s$, and (f) deviation of the reflected rays from the normal for a point located away from the focal length.*

## 4.3. Results and discussions

### *4.3.1. Cooling performance results*

Figure 4.4 shows a comparison between the cooling power, $P_{\text{Cooling}}$, for the six cases as a function of the temperature of the RC, $T_{RC}$, for two types of emittance spectra; the ideal selective emittance spectrum and the ideal broadband emittance spectrum shown in Figure 2. For the results shown in Figure 4.4 it is assumed the atmospheric temperature, $T_{atm}$, is 300 K and the RC is a point source. Furthermore, the heat transfer coefficient, $h$, and solar energy absorptance, $\alpha_{\text{Solar}}$, of the RC are assumed to be 0. For sub-ambient cooling an upper limit for the cooling power occurs when $h$ and $\alpha_{\text{Solar}}$ are zero; in practical applications $h$ and $\alpha_{\text{Solar}}$ will have nonzero values which will reduce the extent to which the structure can be radiatively cooled. The steady-state temperature of the RC

(which occurs when $P_{\text{Cooling}}$ = 0 W·m$^{-2}$) is provided in Table 4.1 for the six cases shown in Figure 4.4 for when the RC has either an ideal selective or ideal broadband emittance spectrum. As shown in Table 4.1, the RC can be cooled to considerably lower temperatures when it is located at the focal length of the parabolic reflector (Cases 4, 5, and 6) as compared to the cases wherein the parabolic reflector is not used. For example, considering the case when the RC has the ideal selective emittance spectrum, the steady-state temperature for Cases 4, 5, and 6 are about 237 K, 230 K, and 229 K, respectively, which are noticeably lower than that for Case 3 (1 m wide flat reflector), Case 2 (infinite flat reflector), and Case 1 (underlying blackbody) which are around 244 K, 243 K, and 276 K, respectively.

The RC reaches a lower steady state temperature for Cases 4, 5, and 6 because the parabolic reflectors shield the RC from a large amount of atmospheric radiation incident from large zenith angles. Moreover, a comparison between the cases wherein the RC resides at the focal length of a parabolic reflector shows that Cases 5 and 6 result in lower equilibrium temperatures compared with Case 4. This is because the height of the parabolic reflector and $f$ are the same in Case 4, whereas the height of the reflector is greater then the $f$ for Cases 5 and 6. That is, the sides of the parabolic reflector block atmospheric radiation incident from large zenith angles for Cases 5 and 6. Additionally, it can be seen that Cases 5 and 6 exhibit similar cooling results, however, the major difference between the two cases is the surface area the parabolic dishes occupy. That is, as the focal length of a parabola decreases, the parabola gets narrower, and its entrance aperture area decreases. For Case 5, wherein $f$ = 0.1 m, the entrance aperture area is 0.78 m$^2$, whereas for Case 6 $f$ = 0.016 m and surface area of the entrance aperture is 0.13 m$^2$. Thus, for example, one parabolic dish cooler can be used per square meter of installation area in Case 5, whereas almost 7 parabolic dish coolers could be used per square meter in Case 6.

Figure 4.4 also reveals that the RC has a lower equilibrium cooling temperature in all cases when it has an ideal selective emittance spectrum as compared to when it has an ideal broadband emittance spectrum. The narrower emittance spectrum of the selective RC compared to a broadband RC corresponds to a smaller radiative power, $P_{RC}$, emitted from the radiator. However, this narrower emissive spectrum also correlates to a higher reflection of incoming atmospheric radiation, $P_{atm}$, which ultimately results in lower steady state temperatures.

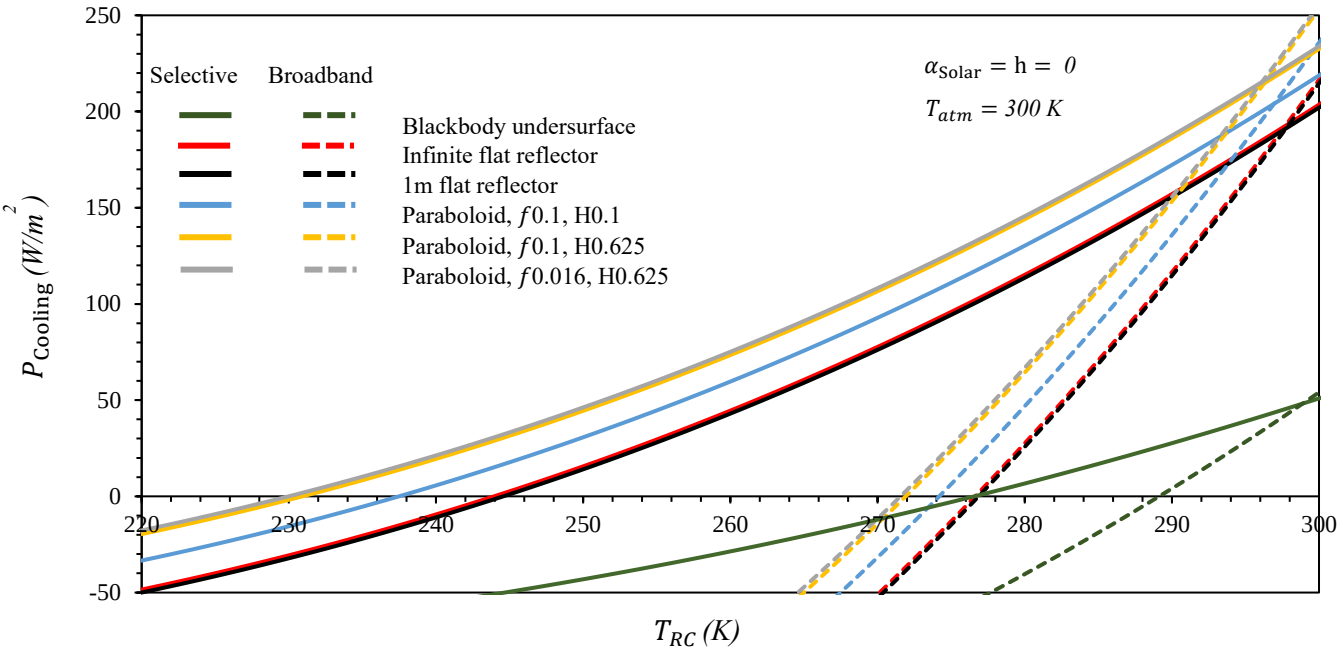


*Figure 4.4 Cooling power ($P_{Cooling}$) as a function of the RC temperature ($T_{RC}$) for the six cases considered in this work when the RC has either the ideal selective (solid lines) or broadband emittance spectra shown in Figure 4.2.*

*Table 4.1 Steady state cooling temperatures ($T_{RC-ss}$) of the six cases.*

| Radiator Type | Case 1 | Case 2 | Case 3 | Case 4 | Case 5 | Case 6 |
|---|---|---|---|---|---|---|
| Selective RC | 276.5 K | 243.9 K | 244.5 K | 237.4 K | 230.9 K | 229.9 K |
| Broadband RC | 289.1 K | 276.6 K | 276.8 K | 276.8 K | 271.9 K | 271.5 K |

Generally, when RC structures employ an underlying reflector to direct thermal radiation to the sky, as the size of the RC material structure increases the portion of radiation that is reflected back to the RC from the reflector also increases, which reduces the radiation emitted to the sky. Therefore, in this study, the temperature of the RCs centered at the focal length of the parabolic reflectors are investigated as a function of their sizes. Figure 4.5 shows $P_{\text{Cooling}}$ as a function of $T_{RC}$ for Cases 4, 5, and 6 when the RC is a point source, or a flat disk with a radius of 0.0125 m, and 0.025 m. The results shown in Figures 4.5a and 4.5b show that the radius of the RC has a negligible effect on its equilibrium temperature when $f$ = 0.1. We attribute this to the fact that both

$P_{RC}$ and $P_{atm}$ decrease as the radius of the RC increases, resulting in an insignificant change in the net cooling. As mentioned previously, $P_{RC}$ decreases because more radiation is reflected back to the RC as its size increases and $P_{atm}$ decreases because less atmospheric radiation is able to reach the bottom of the RC as its size increases. However, as noticed in Figure 4.5c, the RC size has substantial effects on the cooling power results for Case 6 compared to the other cases. This is attributed to the fact that for Case 6, the width of the parabolic dish at its focal length is considerably narrower than the other parabola cases. For Cases 4 and 5 the width of the parabolic dish at the focal length is 0.4 m, and when $r_{RC}$ increases from a point source to 0.025 m the distance between the edge of the RC and the parabolic dish decreases from 0.199 to 0.175 m. In comparison, for Case 6, the width of the parabolic dish at the focal length is 0.064 m, and when $r_{RC}$ increases from a point source to 0.025 m the distance between the edge of the RC and the parabolic dish decreases from 0.031 to 0.007 m. Thus, for Case 6, as $r_{RC}$ increases to the larger values considered in this study it significantly reduces the view factor and radiative exchange between the sky and points on the parabolic dish beneath the RC. The significant reduction of the parabola width at the focal length results in a corresponding increase in the effects of the RC size on the cooling results. For example, in Case 6, the ideal selective and broadband RC with $r_{RC}$ = point source exhibit

cooling powers of 234 W·m$^{-2}$ and 55 W·m$^{-2}$, respectively, while the cooling powers of 148 W·m$^{-2}$ and 162 W·m$^{-2}$ are obtained when $r_{RC}$ = 0.025 m.

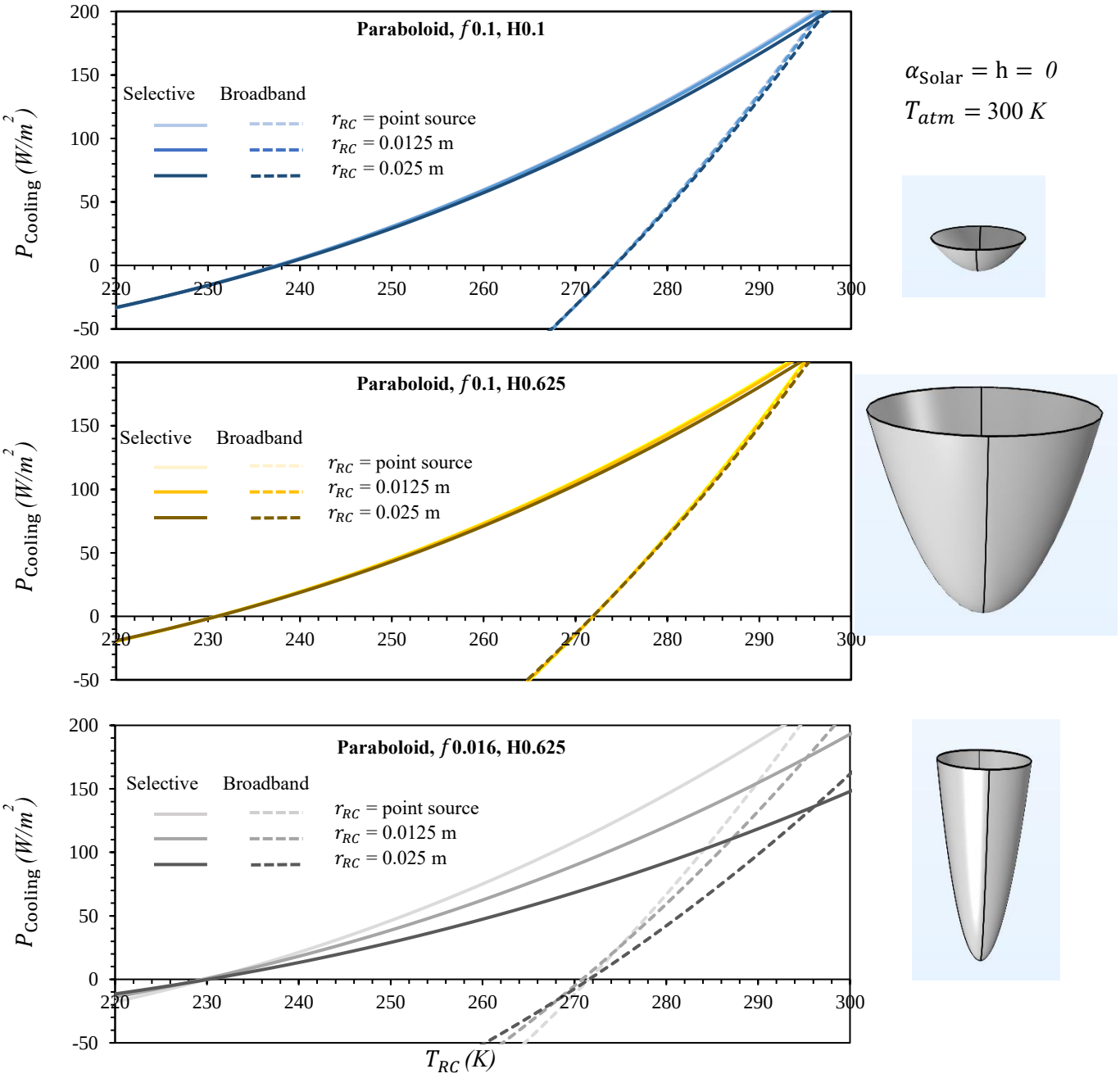


*Figure 4.5. $P_{Cooling}$ results as a function of $T_{RC}$ when RC materials with different sizes are employed in the parabola Cases 4, 5, and 6.*

The effects of changing the convective heat transfer coefficient, $h$, the incident solar radiation, $\alpha_{\text{Solar}}$, and the atmospheric temperature, $T_{atm}$, on the performance of the RC are shown in Figures 4.6 through 4.10. Most of the results presented in these figures are for Case 6, which had the lowest equilibrium cooling temperature in Figure 4.4. For all results presented in Figures 4.6 through 4.10 $r_{RC}$ = point source.

The effects of increasing the convective heat transfer coefficient on the steady state temperature of the RC, $T_{RC-ss}$, when it is an ideal selective emitter is shown in Figure 4.6a for all cases. The atmospheric temperature, $T_{atm}$, and solar absorptance, $\alpha_{\text{Solar}}$, are assumed to be 300 K and zero, respectively, for all results shown in Figure 4.6. As $h$ increases from zero in Figure 4.6a $T_{RC-ss}$ rapidly increases for all cases. For example, for Case 6 when the reflector has a selective surface, $T_{RC-ss}$ increases by about 40 K as $h$ increases from 0 to 2 $W \cdot m^{-2} \cdot K^{-1}$, indicating that non-radiative heat transfer has a strong effect on the cooling ability of the RC. As $h$ continues to increase the temperature of the RC increases monotonically, although to a lesser extent. The cooling power of the RC when it is an ideal selective emitter is plotted as a function of its temperature, $T_{RC}$, and $h$ for Case 6 in Figure 4.6b. As shown, for $P_{\text{Cooling}}$= 0 $W \cdot m^{-2}$ when $h$ = 0 $W \cdot m^{-2} \cdot K^{-1}$ a selective RC cools down to 229 K but as $h$ increases to 2 $W \cdot m^{-2} \cdot K^{-1}$ the RC the temperature of the RC reaches 271 K.

The relation between the steady state temperature of the RC, $T_{RC-ss}$, when it is a broadband emitter and $h$ is shown in Figure 4.6c for all cases. In comparing Figures 4.6a and 4.6c it can be seen that for low $h$ values $T_{RC-ss}$ is significantly lower when the RC is a selective emitter then when it is a broadband emitter. However, as h increases $T_{RC-ss}$ becomes comparable for when the RC is a selective or broadband emitter. The cooling power of the RC when it is a broadband emitter is plotted as a function of $T_{RC}$, and $h$ for Case 6 in Figure 4.6d. This figure shows that for $P_{\text{Cooling}}$= 0 $W \cdot m^{-2}$ when h = 0 $W \cdot m^{-2} \cdot K^{-1}$, the steady state temperate that a broadband RC reaches when $h$ = 0 $W \cdot m^{-2} \cdot K^{-1}$ is 271 K and the steady state temperature is 281 K when h increases to 2 $W \cdot m^{-2} \cdot K^{-1}$.

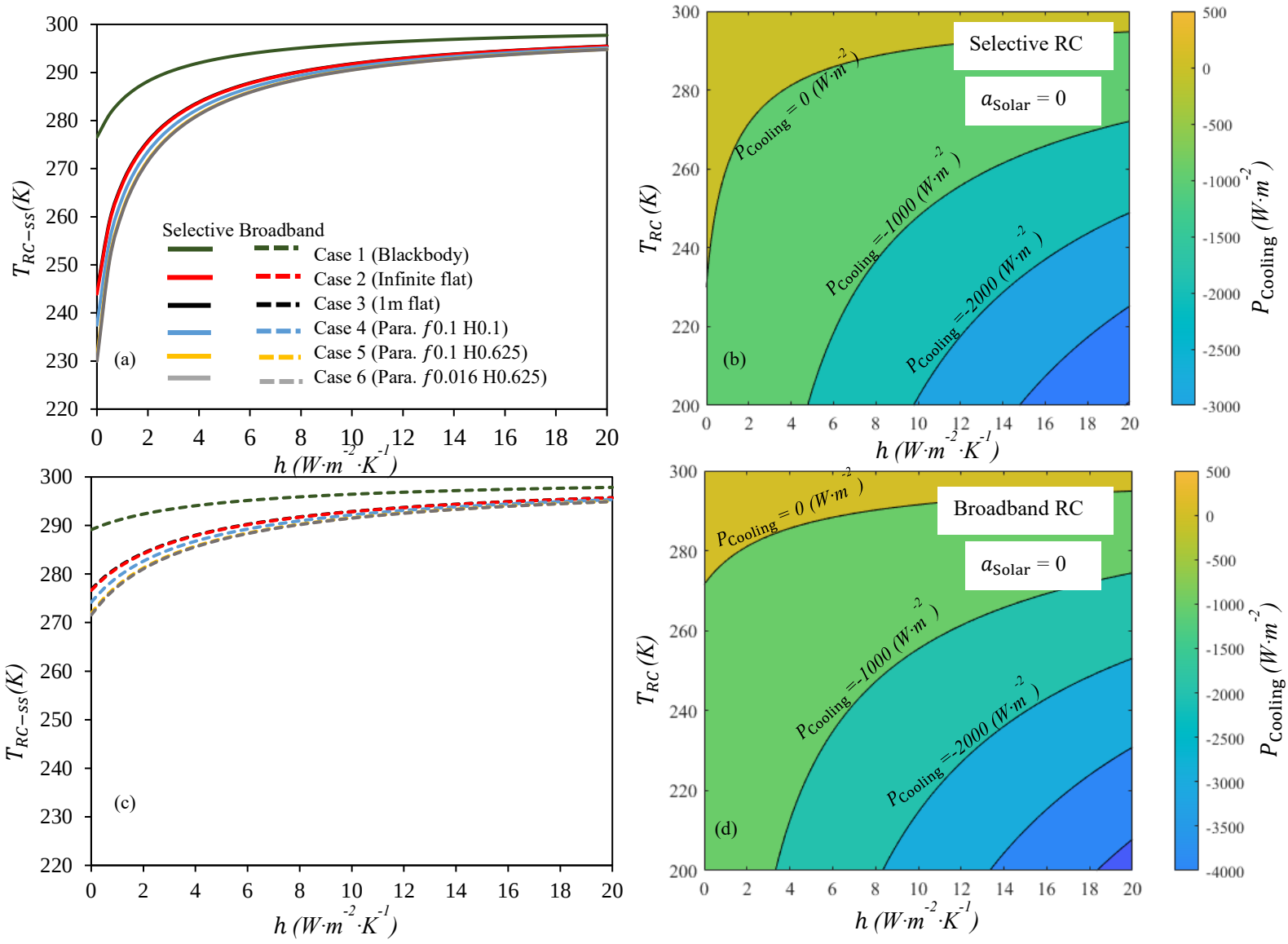


*Figure 4.6. The steady state cooling temperature for Case 6 as a function of the convective heat transfer coefficient (h) for the (a) selective and (c) broadband RC materials. The cooling power for Case 6 as a function of the convective heat transfer coefficient (h) and the RC temperature ($T_{RC}$) using the (b) selective and (d) broadband RC, respectively.*

The effects of increasing the solar absorptance, $\alpha_{\text{Solar}}$, on the cooling performance of the RCs are shown in Figure 4.7. For all results shown in Figure 4.7 the atmospheric temperature, $T_{atm}$, is 300 K and the convective heat transfer coefficient ($h$) is 0 W·m$^{-2}$·K$^{-1}$. The effects of increasing the

solar absorptance, $\alpha_{\text{Solar}}$, on the steady state temperature of the RC when it is a selective emitter are shown in Figure 4.7a for all cases. The solar absorptivity clearly has a strong effect on $T_{RC-ss}$. For example, for Case 1 $T_{RC-ss} = T_{atm}$ (indicating no cooling is occurring) when $\alpha_{\text{Solar}} = \sim 0.05$, and when $\alpha_{\text{Solar}}$ increases to ~0.1-0.12 $T_{RC-ss} = T_{atm}$ for all cases. These results show the importance of using RC materials that are highly reflective towards solar radiation for diurnal RC applications. The cooling power for Case 6 when the RC is a selective emitter is shown as a function of $T_{RC}$ and $\alpha_{\text{Solar}}$ in Figure 4.7b. The cooling power is the largest when $\alpha_{\text{Solar}}$ is low and when $T_{RC}$ is high, because the outgoing radiative heat loss term, $P_{RC}$, increases as $T_{RC}$ increases. The highest cooling power of 230 $W \cdot m^{-2} \cdot K^{-1}$ is achieved for the ideal selective structure when $T_{RC}$ = 300 K and $\alpha_{\text{Solar}} = 0$. The cooling power decreases to less than zero as $T_{RC}$ decreases and as $\alpha_{\text{Solar}}$ increases. For points on Figure 4.7b above the $P_{\text{Cooling}} = 0$ line the value of $P_{\text{Cooling}}$ is negative, which indicates the RC is gaining rather than losing heat.

The correlation between the steady state temperature of the RC, $T_{RC-ss}$, and the solar absorptivity, $\alpha_{solar}$, for when the RC is a broadband emitter is shown in Figure 4.7c. As indicated, for both selective and broadband RC there is an approximately linear increase in $T_{RC-ss}$ as $\alpha_{solar}$ rises. A comparison between Figures 4.7a and 4.7c shows that $T_{RC-ss}$ is significantly lower when the RC is a selective emitter as compared to when it is a broadband emitter for low values of $\alpha_{solar}$. However, as $\alpha_{\text{Solar}}$ increases the value of $T_{RC-ss}$ increases and becomes comparable for when the RC is a selective or broadband emitter. Moreover, as $\alpha_{\text{Solar}}$ increases beyond about 0.12 sub-ambient cooling does not occur for either emitter type. It follows that the $\alpha_{\text{Solar}}$ term is the most influential on the performance of the RC and must be kept to minimal values to achieve cooling whether the RC is an ideal or a broadband absorber. The cooling power for Case 6 when the RC is a broadband emitter is shown as a function of $T_{RC-ss}$ and $\alpha_{\text{Solar}}$ in Figure 4.7d. In comparing Figures 4.7b and 4.7d it can be noted that the $P_{\text{Cooling}} = 0$ line for the selective emitter is lower than that for the broadband emitter, which shows the selective emitter is a more resilient RC under solar radiation. This is because the selective emitter absorbs less atmospheric radiation than the broadband absorber, which helps compensate for a portion of the heat gains caused by incident solar radiation.

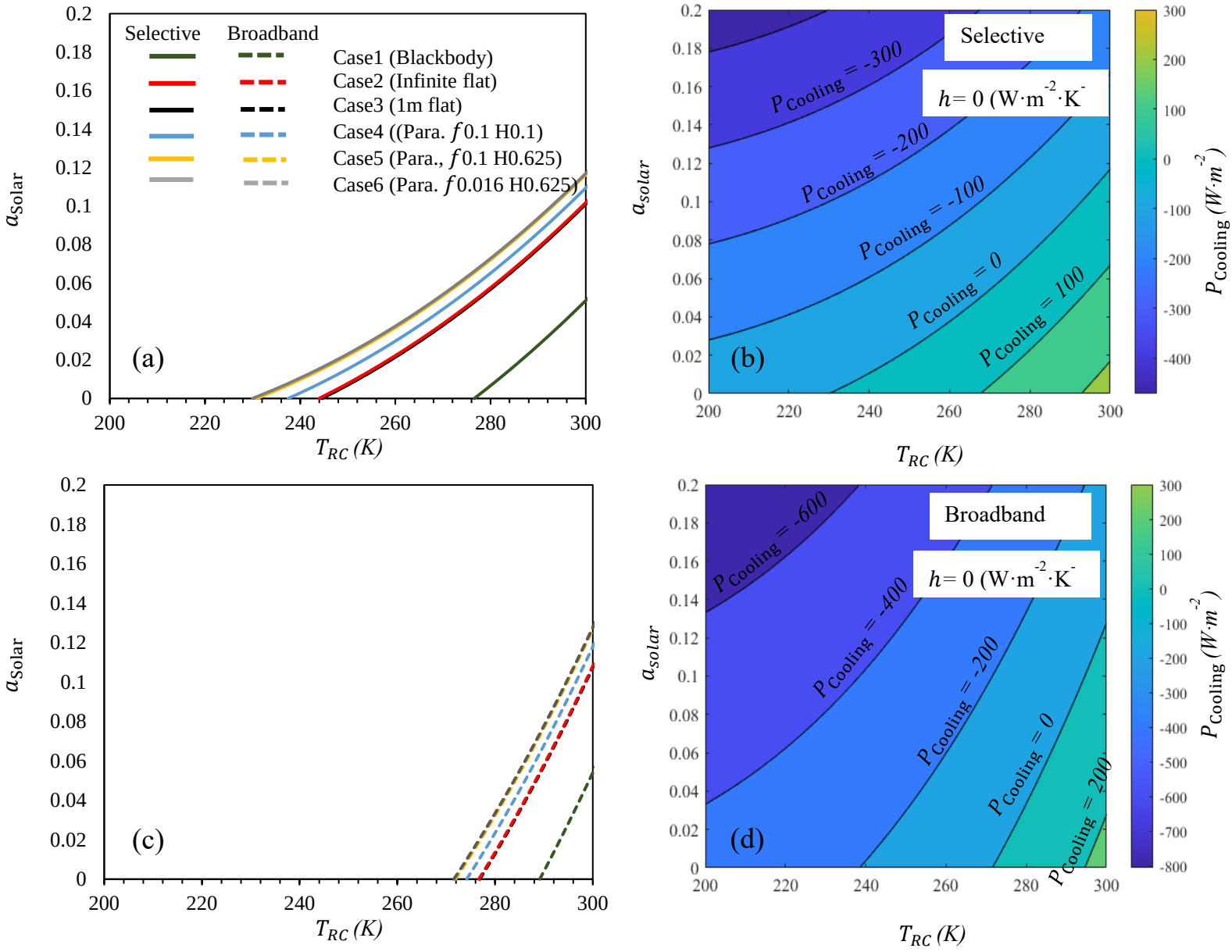


*Figure 4.7 (a) and (c) the steady state cooling temperature results for all cases as a function of the solar absorptance ($\alpha_{Solar}$) for the selective and broadband RC materials, respectively. The cooling power for Case 6 as a function of the solar absorptance ($\alpha_{Solar}$) and the RC temperature ($T_{RC}$) using the (b) selective and (d) broadband RC, respectively.*

The effects of the atmospheric temperature on the RC are shown in Figure 4.8. All results shown in Figure 4.8 are based on the assumptions that the convective heat transfer coefficient, $h$, and the solar absorptance, $\alpha_{\text{Solar}}$, are both zero. Figure 4.8a shows the steady state temperature of the RC increases almost linearly as the atmospheric temperature increases. Figure 4.8b shows the cooling power as a function of the atmospheric and RC temperatures for Case 6 when the RC has a selective emittance spectra. The cooling power decreases to less than zero as expected. It indicates that heating is occurring when the atmospheric temperature, $T_{atm}$, increases and the temperature of the radiative cooler, $T_{RC-ss}$, is sufficiently low. Figure 4.8c shows the steady state temperature of the RC increases almost linearly as the atmospheric temperature increases when the RC has a broadband emittance spectrum, which is similar to the trend observed in Figure 4.8a for the RC with the selective emittance spectrum. The cooling power of the RC is plotted with respect to the atmospheric and steady state temperatures in Figure 4.8d for Case 6 when the RC is a broadband emitter. Similar to the results shown in Figure 4.8b for when the RC is a selective emitter $T_{RC-ss}$ (which is $T_{RC}$ when $P_{\text{Cooling}}$= 0 W·m$^2$) increases as $T_{atm}$ increases. Notably, the temperature difference between $T_{atm}$ and $T_{RC-ss}$, which is known as the thermal reduction below ambient, also increases as $T_{atm}$ increases for the results shown Figures 4.8b and 4.8d. For example, when $T_{atm}$ = 250 K, $T_{RC-ss}$ is about 197 K and 228 K, for the selective and broadband RC, which correlates to temperature reductions of 53 K and 22 K, respectively. However, when $T_{atm}$ = 350 K, $T_{RC-ss}$ also rises to 261 K and 316 K for the selective and broadband RC structures, respectively. Thus, when the atmospheric temperature is 350 K the temperature reduction is 89 K and 34 K for the selective and broadband RCs, respectively. These results are consistent with those reported in the literature. For example, Minghao *et al*. [166] reported that in low humidity regions, higher atmospheric temperatures result in a larger difference between the radiator and the atmospheric temperatures. Feng *et al*. [167] also described that an increased atmospheric air temperature can enhance the cooling performance and larger sub-ambient temperature reduction of the surfaces.

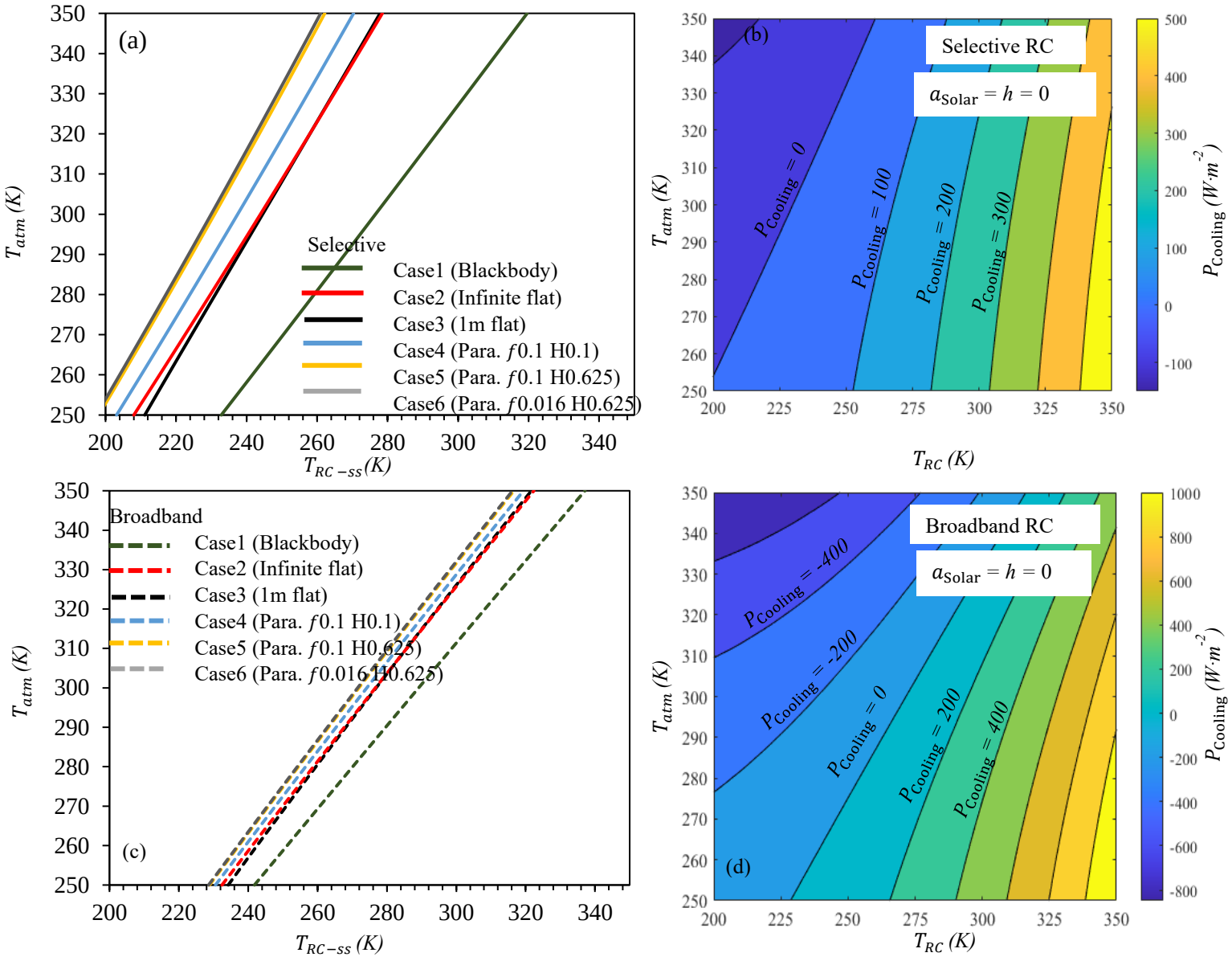


*Figure 4.8 (a) and (c) The steady state cooling temperature results for all cases as a function of the atmospheric temperature ($T_{atm}$) for the selective and broadband RC materials, respectively (b) and (d) cooling power results of the case 6 as a function of the solar absorptance ($T_{atm}$) and the RC temperature ($T_{RC}$) using the selective and broadband RC, respectively.*

The effects of increasing the convective heat transfer coefficient, $h$, and the solar absorptivity, $\alpha_{\text{Solar}}$, on the steady state temperature of the RC are displayed in Figure 4.9 for Case 6. The results for when the RC is a selective emitter are shown in Figures 4.9a and 4.9b, and the results for when

the RC is a broadband emitter are shown in Figures 4.9c and 4.9d. $T_{atm}$ was considered to be 300 K when calculating these results. The black lines in Figures 4.9a-d are isotherms and these lines are labelled with their corresponding temperatures in units of K. As shown in Figures 4.9a and 4.9c sub-ambient cooling is not achieved when $\alpha_{\text{Solar}} > \sim 0.12$ when the RC is a selective emitter or when $\alpha_{\text{Solar}} > \sim 0.13$ when the RC is a broadband emitter. Achieving sub-ambient cooling requires low values of both $h$ and $\alpha_{\text{Solar}}$, which corresponds to the bottom left corner in Figures 4.9a and 4.9c, respectively. The bottom left part of Figures 4.9a and 4.9c are magnified in Figures 4.9b and 4.9d, respectively. From Figures 4.9b and 4.9d it is apparent that when $h$ values are low, increasing $\alpha_{\text{Solar}}$ cause a significant increase in $T_{RC-ss}$. However, at larger $h$ values, the effects of changing $\alpha_{\text{Solar}}$ on $T_{RC-ss}$ are less pronounced.

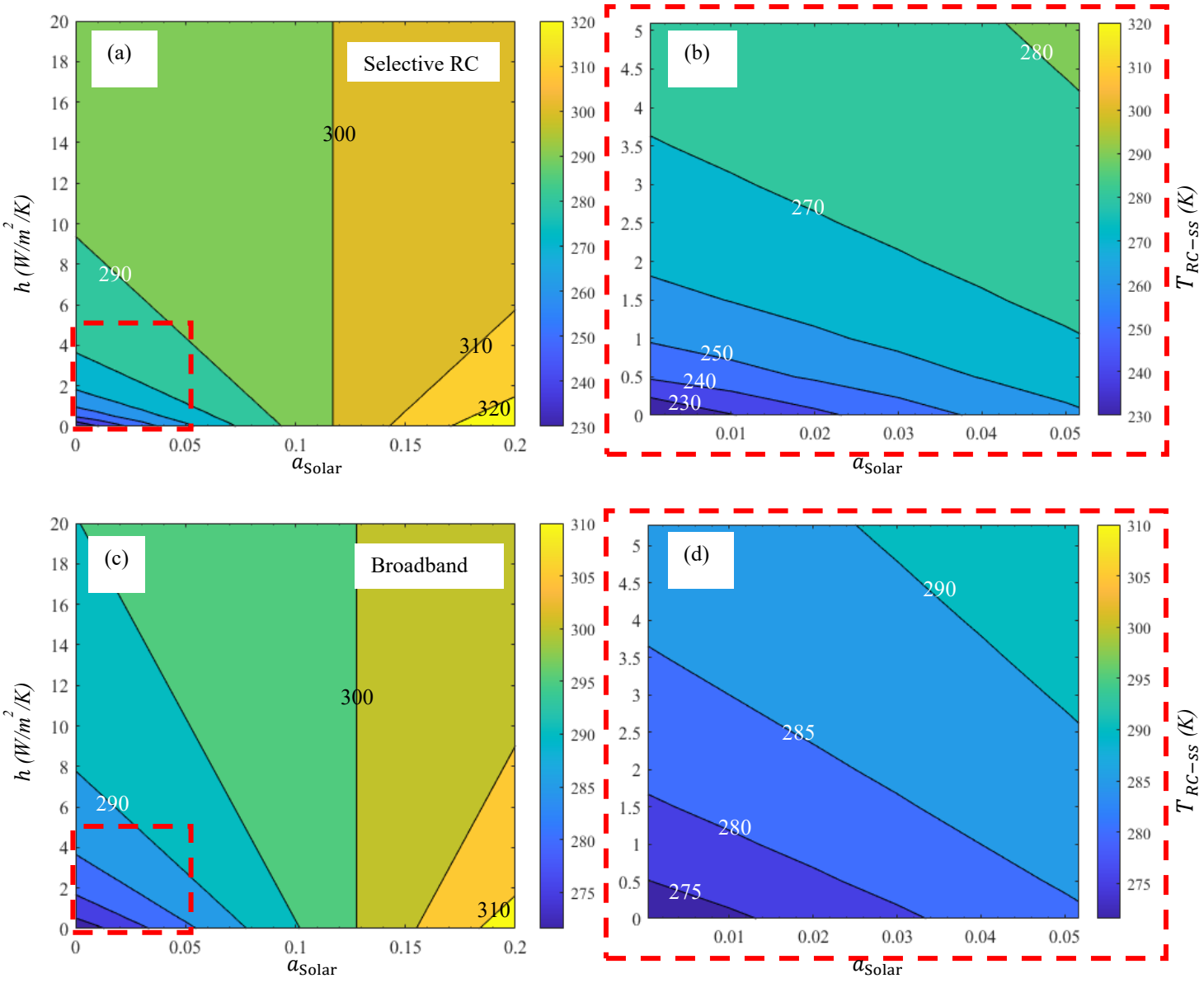


*Figure 4.9 (a) and (c) steady state cooling temperature results of the case 6 as a function of the convective heat transfer coefficient (h) and the solar absorptance ($\alpha_{Solar}$) for the selective and broadband RC materials, respectively, (b) and (d) The maximized graphs of parts shown in red dashed lines of the selective and broadband RC materials, respectively.*

The results presented thus far have been determined under the assumption that the emittance of the RC over the atmospheric window, which ranges from ~ 8 to ~ 13 μm, is one. However, in

practical applications the emittance of the RC over the atmospheric window will have some value less than one. To investigate the effects of reducing the emittance of the RC on its cooling performance we consider different values of the average emittance over the atmospheric window, denoted herein as $\varepsilon_{AW}$. The effects of $\varepsilon_{AW}$, $\alpha_{\text{Solar}}$, and $h$ on $T_{RC-ss}$ for Case 6 are shown in Figure 4.10. The results in Figure 4.10 were determined under the assumption that $T_{atm}$ = 300 K. The steady state temperature of the RC is constant along the black lines shown in Figure 4.10 and the corresponding temperature for these lines is shown in units of Kelvin. Moreover, Figures 4.10a and 4.10b show the results for when the RC is a selective emitter while for Figures 4.10c and 4.10d the RC has a broadband emitter. The emission spectra for the selective and broadband emitters shown in Figure 4.10 are similar to those shown in Figure 4.2, but with the emittance equal to $\varepsilon_{AW}$ rather than one.

Figures 4.10 a and c show that when $h$ = 0 W·m$^{-2}$·K$^{-1}$, increasing $\alpha_{\text{Solar}}$ causes a significant increase in $T_{RC-ss}$, whereas decreasing $\varepsilon_{AW}$ increases $T_{RC-ss}$ to a lesser extent. These trends are especially pronounced for low values of $\alpha_{\text{Solar}}$. For example, according to Figure 4.10a ($h$ = 0 W·m$^{-2}$·K$^{-1}$ and selective RC) when $\alpha_{\text{Solar}}$ = 0, increasing $\varepsilon_{AW}$ from 0.5 to 1 causes $T_{RC-ss}$ to decrease from about 260 K to 230.9 K. On the other hand, if $\varepsilon_{AW}$ is constant at 0.5 when $\alpha_{\text{Solar}}$ is decreased from 0.05 to 0 $T_{RC-ss}$ decreases from 308 K to 260 K. When $h$ is 5 W·m$^{-2}$·K$^{-1}$ the value of $T_{RC-ss}$ increases with increasing $\alpha_{\text{Solar}}$, although to a lesser extent as compared to when $h$ = 0. For example, Figure 4.10b shows that when $h$ = 5 W·m$^{-2}$·K$^{-1}$ a reduction of $\alpha_{\text{Solar}}$ from 0.05 to 0 results in a decrease of $T_{RC-ss}$ from 301.6 K to 293.5 K.

The results shown in Figure 4.10 are consistent with those reported in the literature. For example, Li *et al*. [25], [168] defined a standard figure of merit, $F_{RC}$, to evaluate the RC performance of structures tested under similar weather conditions as follows:

$$F_{RC} = \varepsilon_{AW} - q\,(1 - R_{\text{Solar}}) \tag{4.16}$$

where $\varepsilon_{AW}$ is the emittance of the radiative cooler over the atmospheric window and $q$ is the ratio of the solar radiation power divided by the radiative power of a blackbody at 300 K in the 8 – 13 μm spectral range (for example, when the solar irradiance is 1000 W·m$^{-2}$, and given that a blackbody at a temperature of 300 K radiates 100 W·m$^{-2}$ over the spectral range from 8 – 13 μm, $q$ is equal to 10), $R_{\text{Solar}}$ is the solar power reflectance of the structure ($R_{\text{Solar}}$= 1-$\alpha_{\text{Solar}}$ for an

opaque material). They also confirmed that due to the intense solar power compared to the radiative power emitted over the atmospheric window, to achieving high-performance radiative cooling under sunny conditions it is more important to increase the solar reflectance than the emittance of the RC.

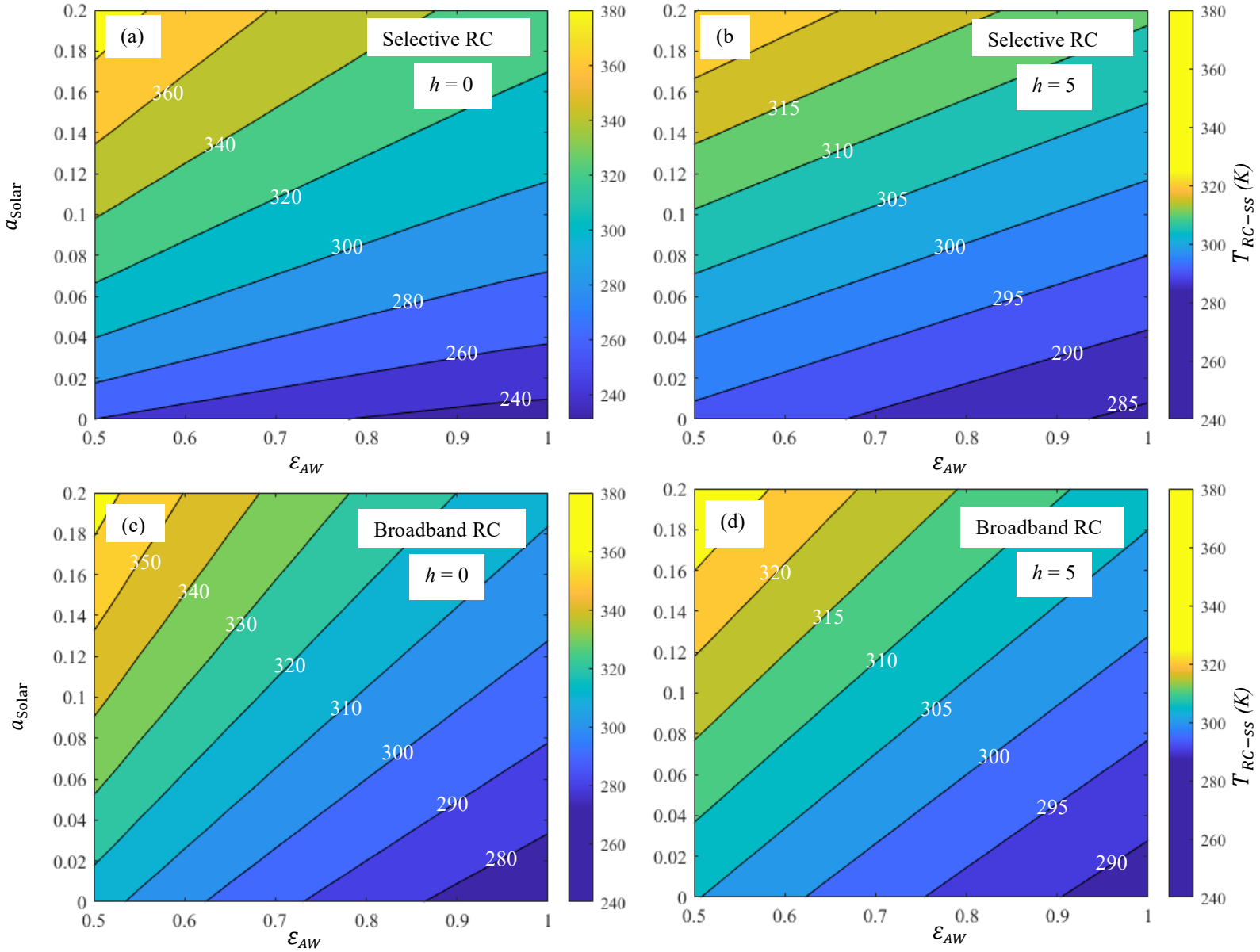


*Figure 4.10 steady state cooling temperature results of the case 6 as a function of the solar absorptance ($\alpha_{Solar}$) and the emittance in the atmospheric window ($\varepsilon_{AW}$) for (a) selective RC with h = 0, (b) selective RC with h = 5, (c) Broadband RC with h = 0, (d) Broadband RC with h = 5.*

## 4.4. Conclusion

In conclusion, this study has investigated the cooling performance of RC structures in three dimensions using various configurations with and without underside reflectors. The numerical analyses involve six different cases, including a blackbody undersurface (Case 1), an infinite flat reflector (Case 2), a flat reflector with a width of 1 m (Case 3), and parabolic reflectors (Cases 4, 5, and 6) with different focal lengths and dimensions. The investigations are performed using two different spectra: an ideal selective emitter and an ideal broadband emitter.

The study addresses the variations in the net cooling power calculations for the different cases. For Cases 4, 5, and 6, which utilize parabolic reflectors, MCRT methods are developed to simulate radiative heat transfer interactions. The code considers the emission and reflection angles of the rays to capture the fraction of rays emitted and reflected by the RC. The MCRT simulations provides the fractions of rays emitting spherically and reflecting from the parabolas to the sky within specific angles. These fractions are then incorporated into the cooling performance calculations to obtain the overall cooling results of the structures.

Results show that considering an ideal selective emittance spectrum in the absence of solar absorption and convective heat transfer at an ambient temperature of 300 K, the steady-state temperatures for Cases 4, 5, and 6 are approximately 237 K, 230 K, and 229 K, respectively. These temperatures are noticeably lower than those observed for Case 3 (1 m flat), Case 2 (infinite flat), and Case 1 (blackbody), which exhibit temperatures around 244 K, 243 K, and 276 K, respectively. In Case 6, a smaller entrance aperture surface area compared to Cases 4 and 5 limits the radiation arriving at the entrance aperture to smaller supplementary angle of the rim angle. Furthermore, approximately seven instances of Case 6 reflectors can be accommodated within the same surface area that Case 5 occupies.

The parabolic configuration studied here offers a versatile cooling solution that can be used independently or integrated into various applications such as air- and water-based cooling systems, air-conditioning, $CO_2$ capture, and water harvesting. By incorporating a parabolic reflective surface beneath a RC material, the proposed RC system achieves remarkable temperature reduction, making it ideal for enhancing water condensation and collection which demonstrates superior performance compared to existing RC structures.

# Chapter 5

## 5. Optimized porous PVDF-HFP as radiative cooling materials

### 5.1. Introduction

Currently, significant research efforts are being directed towards improving the surfaces of RC structures by tuning their emissivity, absorptivity, and reflectivity. The development of RC surfaces aims to prevent the absorption of solar radiation and enhance the emission of LWIR radiation over the atmospheric window (which ranges from ~ 8 to 13 μm). Attaining these specific spectral properties enables passive daytime RC of surfaces, even when being exposed to direct solar irradiation. Achieving sub-ambient cooling requires the RC coating to emit more radiant energy over the atmospheric window than it absorbs over the solar spectrum. Extensive investigations have been done to introduce a diverse array of inventive materials well-suited for passive daytime RC. Therefore, several advanced structures have been developed to simultaneously optimize both solar reflectivity and thermal emissivity. Examples include multilayered films [66][2][92], composite materials with nanoparticles [169][170][23][171][58][172], and coatings using porous media [170][94][121][55][50]. For example, Chae et al. [64] developed a multilayered structure using $Al_2O_3$, $Si_3N_4$, and $SiO_2$. The thickness of each layer was fine-tuned to increase emissions over the 8−13μm range. The resultant radiative cooler demonstrated an average emissivity of 87%

over the atmospheric window and a 5.2% average absorptivity in the solar spectral region (0.3−2.5μm). During direct sunlight exposure, the cooler effectively lowered temperatures by up to 8.2˚C compared to the inner ambient temperature. However, the reflectivity of solar energy in this material structure is suboptimal and necessitates improvements. Raman et al. [4] presented an integrated photonic solar reflector and thermal emitter composed of seven layers of $HfO_2$ and $SiO_2$. This innovative structure reflects 97% of incident sunlight, simultaneously exhibiting an average emissivity of 66% within the atmospheric transparency window. Nevertheless, there is room for improvement in the emissivity within the atmospheric window.

Polymeric coatings represent another strategy for passive daytime RC, known not only for their adaptability and easy application to surfaces with diverse compositions, textures, and geometries, such as roofs or walls but also for their scalability and low cost [50][173][85][53]. Various methods, such as the incorporation of nanoparticles and air voids to introduce porosity, can be employed to optimize both low solar absorption and enhanced mid-infrared emission in polymeric coatings. Efforts to develop paint like coatings with the capability of sub-ambient daytime RC have been ongoing for a considerable period. In many of these studies, common pigments found in commercial paints such as $TiO_2$, $SiO_2$, $BaSO_4$, and ZnS particles have been employed [174][175][26]. Zhang et al. [176] showed the daytime sub-ambient RC capabilities of a cellulose/calcium silicate composite film characterized by a broad size distribution of pores. The presence of numerous pores and calcium silicate particles contributed to outstanding performance, resulting in integrated solar reflectance of 97.3% and atmospheric emittance of 97.2%. Bao et al. [175] introduced a double-layer coatings, comprised of a highly reflective top layer with a high solar albedo and a bottom layer with enhanced emissivity through the careful design of $TiO_2$, $SiO_2$, and SiC nanoparticles. These coatings consist of densely packed $TiO_2$ particles atop closely packed SiO2 nanoparticles. When applied to an aluminum substrate, the $TiO_2$ and $SiO_2$ combination demonstrates an overall reflectivity of 90.7% in the solar spectrum, coupled with an emittance of 90.11% within the atmospheric window. Wang et al. [52] presented findings on a polymethyl methacrylate (PMMA) film structured hierarchically, featuring a micropore array with pore sizes spanning 5 to 7 μm and additional random nanopores with sizes ranging from 200–300 nm. The hierarchically porous PMMA film exhibits a solar reflectance of 95% and a high thermal emittance in the atmospheric window region, measuring 98%. PVDF-HFP is a compelling polymer employed in passive daytime RC. Its notable features include high emissivity within the atmospheric window,

attributed to molecular vibrations, coupled with solar radiation transparency. The material is characterized by flexibility, thermal stability, and easy modifiability through the incorporation of additives or nanoparticles, providing researchers the ability to customize its properties for improved RC performance. As an example, Mandal et al. [50] made significant steps in designing PVDF-HFP polymeric coatings for passive daytime RC. They utilized a phase inversion-based method to introduce random micro-/nano-pores, resulting in impressive properties, including high solar reflectance (96%) and elevated longwave infrared emittance (%97). In another study by Ma et al. [173], a porous composite was created by integrating silica microspheres into a cast of hierarchical porous PVDF-HFP polymer. Through the incorporation of a 12% fraction of $SiO_2$ and the influence of superimposed Mie scattering, the solar reflectance saw a notable increase to 94%, representing an 11% improvement when compared to traditional white paint. Xue et al. [170] also examined adding hydrophobic $SiO_2$ into PVDF-HFP polymer and suggested an approach to manufacture a hierarchically structured porous composite possessing super hydrophobicity and RC properties using a phase separation. In its pristine state, the porous PVDF-HFP film, without $SiO_2$, exhibited a solar reflectance of approximately 95% and LWIR emittance of around 97%. In their study, the introduction of a small quantity of silica reduced the solar energy reflectivity to 93%; however, this addition led to an enhancement in LWIR emittance to 98%. Nilson et al. used a polyethylene foil pigmented with $TiO_2$ and $BaSO_4$ to carry out an outdoor experiment regarding water condensation applications in Tanzania. They showed that pigmented polyethylene foils possessing a high solar reflectance and a high LWIR emittance can effectively collect dew water from humid air even in arid regions [177]. Also, low-cost, scalable, and robust plastic micro-grooved foils designed by Lavielle et al. showed a high enhancement in dew collection without aging effects and a great durability after 6 months [178]. While promising results have been achieved in lab-scale studies, further research is needed to address the scalability and practical applicability of these RC materials. This includes assessing their performance under real-world conditions and potential challenges in large-scale implementation. Therefore, there is still an opportunity for enhancement in the emissivity within the atmospheric window and solar reflectance in the PVDF-HFP polymeric RC system.

In alignment with the valuable insights from prior studies and the considerations highlighted earlier, a phase inversion technique was adopted to craft a hierarchically porous structure for PVDF-HFP with the aim of creating an efficient RC material. Parameters critical to the fabrication

process, including the polymer, solvent, and nonsolvent mass ratio, and thickness of the samples are precisely controlled to optimize solar reflectivity and emissivity over the atmospheric window. Leveraging the micro and nano-sized pore distributions within the structure facilitates a notable solar reflectivity of 98.2%, a parameter modifiable through variations in the polymer, solvent, and nonsolvent concentrations. Furthermore, the associated porous RC sample achieves a substantial emissivity of 98.5%, due to the intrinsic infrared resonance of ─$CF_3$/─$CF_2$ positioned within the atmospheric window (8−13 μm). Numerical analysis reveals this sample can potentially posses a cooling power and steady state cooling temperature of 86 $W \cdot m^{-2}$ and 291 K, respectively, when the convective heat transfer coefficient and ambient temperature are 5 $W \cdot m^{-2} \cdot K^{-1}$ [179] and 300 K, respectively. Moreover, an experimental setup is used to simulate dew collection and conduct measurements of the water harvesting ability of the developed RC samples. The use of this advanced apparatus facilitates a deeper understanding of the RC process and its potential for efficient dew harvesting applications, thereby contributing valuable insights to the field.

## 5.2. Materials and methods

### *5.2.1. Materials*

PVDF-HFP (Sigma-Aldrich, CAS Number: 9011-17-0) with an average molecular weight of approximately 400,000 and an average number molecular weight of about 130,000 was employed as the primary polymer in this study. Pellets of PVDF-HFP were sourced for the experiments. Deionized (DI) water and 99.9% acetone are utilized as the nonsolvent and solvent of the polymer, respectively.

PVDF-HFP was selected for RC samples due to its exceptional combination of thermal, optical, mechanical, and chemical properties. PVDF-HFP offers superior thermal stability, maintaining its structure and performance under high-temperature fluctuations, which is essential for outdoor applications. It exhibits high emissivity in the LWIR region, enabling effective heat radiation into the atmospheric window, a critical feature for RC materials. Additionally, PVDF-HFP's optical properties can be easily tailored through porosity or additives, enhancing solar reflectance and thermal emissivity. Its flexibility further allows it to conform to curved or edged surfaces, making it suitable for diverse applications such as cooling panels and irregularly shaped rooftops, where other polymers' rigidity poses limitations. PVDF-HFP also provides excellent resistance to UV

radiation, moisture, and corrosive chemicals, ensuring long-term durability in outdoor environments. Its lightweight nature, cost-effectiveness, scalability, and adaptability to various fabrication techniques, such as phase inversion, make PVDF-HFP an ideal choice for high-performance RC systems.

### *5.2.2. Fabrication of the porous RC samples*

Phase inversion was used to produce a hybrid micro- and nano-cellular structure in a PVDF-HFP film intended for use as a RC material in this investigation. Precursor solutions with different mass ratios of PVDF-HFP, acetone, and water were obtained. In this method, PVDF-HFP was initially dissolved in acetone under reflux conditions with continuous mechanical stirring, aiming to create a uniform casting solution. The PVDF-HFP concentration in the solution varied with mass ratios of 0.75, 1, and 1.25 relative to the acetone mass ratio of 8, and this process occurred at a temperature of 40˚C. During stirring, deionized water, accounting for 0.75, 1, and 1.25 relative to the acetone mass ratio of 8, was gradually introduced until homogeneity was achieved. The stirring was then halted, allowing the solution to stand undisturbed for 1 h to cool down. Subsequently, the casting solution was applied to a pristine glass plate. Upon the completion of acetone and water evaporation, the outcome was the formation of white, opaque porous RC film samples. Table 5.1 presents the polymer and water concentrations for each sample, along with their corresponding identifications used in this study. Additionally, Table 5.2 provides details on the samples investigated at various thicknesses, including their respective identifications. To achieve different thicknesses of the samples, varying volumes of the polymer solution were poured onto the substrate. After the solutions were allowed to dry, the resulting films had different thicknesses, which were then used for further investigation.

*Table 5.1 Composition and identification of the samples investigated in the study.*

| Sample | PVDF-HFP concentration (w/w) | Water concentration (w/w) | Identification |
|---|---|---|---|
| Sample 1 | 0.75 | 0.75 | **0.75-8-0.75** |
| Sample 2 | 0.75 | 1 | **0.75-8-1** |

| | | | |
|---|---|---|---|
| Sample 3 | 0.75 | 1.25 | **0.75-8-1.25** |
| Sample 4 | 1 | 0.75 | **1-8-0.75** |
| Sample 5 | 1 | 1 | **1-8-1** |
| Sample 6 | 1 | 1.25 | **1-8-1.25** |
| Sample 7 | 1.25 | 0.75 | **1.25-8-0.75** |
| Sample 8 | 1.25 | 1 | **1.25-8-1** |
| Sample 9 | 1.25 | 1.25 | **1.25-8-1.25** |

*Table 5.2 Sample thickness and corresponding identifications for variants of sample 6.*

| Sample | Thickness (µm) | Identification |
|---|---|---|
| Sample 6_320 | 320 | **1-8-1.25_320** |
| Sample 6_612 | 612 | **1-8-1.25_612** |
| Sample 6_726 | 726 | **1-8-1.25_726** |
| Sample 6_850 | 850 | **1-8-1.25_850** |

### *5.2.3. Characterization of the porous RC samples*

For phase morphology observation, the porous PVDF-HFP film samples were cryo-fractured and examined using a scanning electron microscope (SEM, Thermofisher Quanta 3D). The functionality of the RC materials was also assessed in terms of optical performance, including spectral reflection, transmission, and absorption, within the wavelength ranges of 0.3–2.5 µm, covering the ultraviolet, visible, and near-infrared spectrums, using a UV-Vis-NIR spectrophotometer. Additionally, the optical behavior in the mid-infrared wavelength ranges was examined through Fourier transform infrared (FTIR) spectroscopy, Bruker Vertex 70 FTIR Spectrometer. The EM-4 Emissometer was also employed to measure and analyze the total directional LWIR emissive properties of the fabricated materials at about 390 K (e.g. wavelengths 8-12 µm) using which the total hemispheric emissivity was calculated.

### *5.2.4. Theoretical assessments of radiative cooling efficiency*

A RC material structure exposed to the sky undergoes thermal energy exchange with its surroundings. Simultaneously radiating heat to outer space ($P_{RC}$), it is subject to influences from solar irradiance ($P_{solar}$), atmospheric downward thermal radiation ($P_{atm}$), and incoming convective thermal energy from the ambient surroundings ($P_{Conv.}$). Consequently, the net cooling power of a sky-facing RC material structure can be computed as follows [2][52]:

$$P_{\text{net},Cool}(T_{RC}) = P_{RC}(T_{RC}) - P_{atm}(T_{amb}) - P_{Solar} - P_{Conv.}(T_{RC}, T_{amb}) \quad (5.1)$$

where $T_{RC}$ and $T_{amb}$ are the RC sample and ambient temperatures, respectively. The following equations can be employed to calculate these thermal exchange factors:

$$P_{RC}(T_{RC}) = A\, 2\pi \int_0^{\frac{\pi}{2}} \sin\theta cos\theta \int_0^{\infty} I_{BB}(T_{RC}, \lambda)\, \varepsilon_{RC}(\lambda)\, d\lambda\, d\theta \quad (5.2)$$

$$P_{atm}(T_{amb}) = A\, 2\pi \int_0^{\frac{\pi}{2}} \sin\theta\, cos\theta \int_0^{\infty} I_{BB}(T_{amb}, \lambda)\, \varepsilon_{RC}(\lambda)\, \varepsilon_{atm}(\lambda, \theta) d\lambda\, d\theta \quad (5.3)$$

$$P_{\text{Solar}} = A \int_0^{\infty} G_{AM1.5}(\lambda)\, \varepsilon_{RC}(\lambda)\, d\lambda = 1000 \times (1 - \bar{R}_{solar}) \quad (5.4)$$

$$P_{Conv.} = A\, h\, (T_{atm} - T_{RC}) \quad (5.5)$$

In these equations, $A$ denotes the area of the top surface of the radiator, $\lambda$ represents the wavelength of radiation, and $I_{BB}$ is the spectral intensity of a blackbody, which can be determined using Planck's law. The sky temperature and the emissivity of the sky are assumed to be 0 K and 1, respectively. $\varepsilon_{RC}(\lambda)$ represents the spectral emittance of the radiator, considered independent of direction. $\varepsilon_{atm}(\lambda, \theta)$ denotes the spectral directional emittance of the atmosphere and can be determined as follows [180][52], where $\tau(\lambda)$ is the spectral atmospheric transmittance in the normal direction:

$$\varepsilon_{atm}(\lambda, \theta) = 1 - \tau(\lambda)^{1/\cos\theta} \quad (5.6)$$

The relationship between atmospheric transmittance and emissivity is expressed as

$$\varepsilon_{atm}(\lambda,\theta) = 1 - t_{atm}(\lambda,\theta) \tag{5.7}$$

$$t_{atm}(\lambda,\theta) = \tau(\lambda)^{1/\cos\theta} \tag{5.8}$$

In this study, the entire atmospheric layer, from ground to outer space, is modeled as a unified medium, and the ambient temperature is used as a substitute for the variable temperature, which naturally fluctuates with altitude. $\tau(\lambda)$ is obtained using ATRAN, a software computing the spectral transmittance of Earth's atmosphere in different locations, specifically for Toronto, Canada. The effects of radiation reflected from the atmosphere on the cooling performance of the radiative cooler are neglected. $G_{AM1.5}(\lambda)$ represents the solar air mass 1.5 (AM1.5) irradiance spectrum and $h$ indicates the convective heat transfer coefficient. For the analysis, it is assumed that the solar irradiance is constant at 1000 W·m$^{-2}$, representing typical conditions for direct solar exposure at noon time. This allows for the simplification of the maximum absorbed solar power, which can be expressed in relation to the average solar reflectance ($\bar{R}_{solar}$) of the material

To achieve successful passive daytime RC, an object must minimize heat gain from the solar energy and maximize the thermal energy radiated from the RC to the cold sky above. Achieving this goal requires a RC surface with a high $\bar{R}_{solar}$ as well as a high average hemispherical LWIR emittance ($\bar{\varepsilon}_{LWIR}$), which can be calculated using the following equations:

$$\bar{R}_{solar} = \frac{\int_0^{\infty} G_{AM1.5}(\lambda)\, R_{solar}(\lambda) d\lambda}{\int_0^{\infty} G_{AM1.5}(\lambda) d\lambda} \tag{5.9}$$

$$\bar{\varepsilon}_{LWIR} = \frac{\int_{8\,\mu m}^{13\,\mu m} I_{BB}(T_{RC},\lambda)\, \varepsilon_{RC}(T_{RC},\lambda) d\lambda}{\int_{8\,\mu m}^{13\,\mu m} I_{BB}(T_{RC},\lambda) d\lambda} \tag{5.10}$$

where $R_{solar}(\lambda)$ and $\varepsilon_{RC}(T_{RC},\lambda)$ are spectral hemispherical reflectance and spectral hemispherical emittance of the RC material.

## 5.3. Results and discussions

### *5.3.1. Phase morphology of porous PVDF-HFP samples*

The cross-sectional SEM micrographs of the PVDF-HFP porous samples presented in Figures 5.1 a-i offer invaluable insights into the morphological changes induced by altering the water and polymer contents during the fabrication process. Comparing the SEM micrographs at the same PVDF-HFP polymer content but different water contents reveals that an increase in water content resulted in a discernible transformation towards a more porous architecture. That is, with rising water content, specifically from a water-to-acetone concentration ratio of 1 to 1.25, while keeping the polymer content constant, an increase in pore sizes observed. Furthermore, at a water-to-acetone ratio of 1.25 to 8, regardless of polymer concentrations, a distinctive a bimodal distribution of the nano and micro pore sizes was observed, suggesting the successful creation of fine-tuned porous structures within the PVDF-HFP films. Micro-sized pores become more prevalent with averages sizes of 4.8 ± 0.8 μm, 8.18 ± 1.6 μm, and 5.0 ± 0.9 μm (the uncertainty is the standard deviation of the distribution shown in Fig. 2 c, f, and i), corresponding for samples with polymer-to-acetone-to-water ratios of 0.75-8-1.25, 1-8-1.25, and 1.25-8-1.25, respectively. The observed phenomenon regarding an increase in water content can be attributed to three main factors. Firstly, water, being a non-solvent for PVDF-HFP, induces a phase separation during the casting process. This separation leads to the creation of distinct polymer-rich and polymer-lean regions, contributing to the development of a porous structure. Secondly, the presence of water vapor acts as a nucleating agent for pore formation. As the vapor permeates through the polymer solution, it initiates the nucleation of micro-sized pores. With increasing water content, more nucleation sites are available, leading to the growth of a higher density of micro-sized pores within the material. Thirdly, higher water content accelerates the evaporation of the solvent (e.g., acetone in this study) and facilitates quicker phase separation. This rapid separation allows for the formation of a more porous structure with well-defined micro-sized pores. Therefore, the heightened evaporation rate and accelerated phase separation collectively contribute to the observed increase in porosity. However, according to the SEM images of samples with different polymer contents but a constant water concentration a different trend emerges. For example, as the polymer-to-acetone content rises from 0.75 to 1 and 1.25 in samples with a high consistent water-to-acetone concentration ratio of 1.25, an initial expansion in pore sizes from 4.8 ± 0.8 μm to 8.2 ± 1.6 μm, is observed, succeeded by a subsequent decrease to 5.0 ± 0.9 μm. Thermodynamically, phase separation occurs due to the non-solvency of the polymer (PVDF-HFP) in the solvent (Acetone)-water system particularly with

high water concentrations. Further, at higher water concentrations the presence of excess water reduces the solubility of the polymer in the solvent, leading to a stronger driving force for phase separation. Increasing the polymer content in this regime can more readily overcome the energetic barrier for phase separation, resulting in larger changes in pore sizes. Therefore, increasing the polymer concentration in high water concentration systems enhances the driving force for phase separation, leading to the formation of larger pores due to the stronger segregation of the polymer-rich and polymer-lean phases. As polymer content rises, the solvent-water system becomes less favorable for polymer solvation, leading to the spontaneous separation of the polymer-rich and polymer-lean phases. Since the polymer concentration continues to increase, the solution viscosity becomes significantly higher. This increased viscosity can hinder the mobility of polymer chains and solvent molecules, slowing down the phase separation process and the diffusion of solvent and water molecules out of the system. As a result, there may be less time for the formation and growth of large pores before the solution solidifies or sets. Conversely, at lower water concentrations, the polymer-solvent system tends to be closer to a single-phase region compared to higher water concentrations. In this scenario, the thermodynamic driving force for phase separation is weaker due to the higher solubility of the polymer in the solvent. As a result, even with an increase in polymer content, the system may not reach the threshold required for significant phase separation and pore growth. An increase in pore sizes is observed with rising water content, specifically from 1 to 1.25 while keeping the polymer content. In samples with water content of 0.75, the limited availability of the water as the nonsolvent leads to a slower phase separation during the phase separation process which favors the formation of finer pores with nano sizes. When water content increases to levels of 1.25 the phase separation dynamic increases significantly. The higher level of the nonsolvent accelerates the phase separation this results in the formation of the micropores as the primary structure with nano pores forming inside the nano pores.

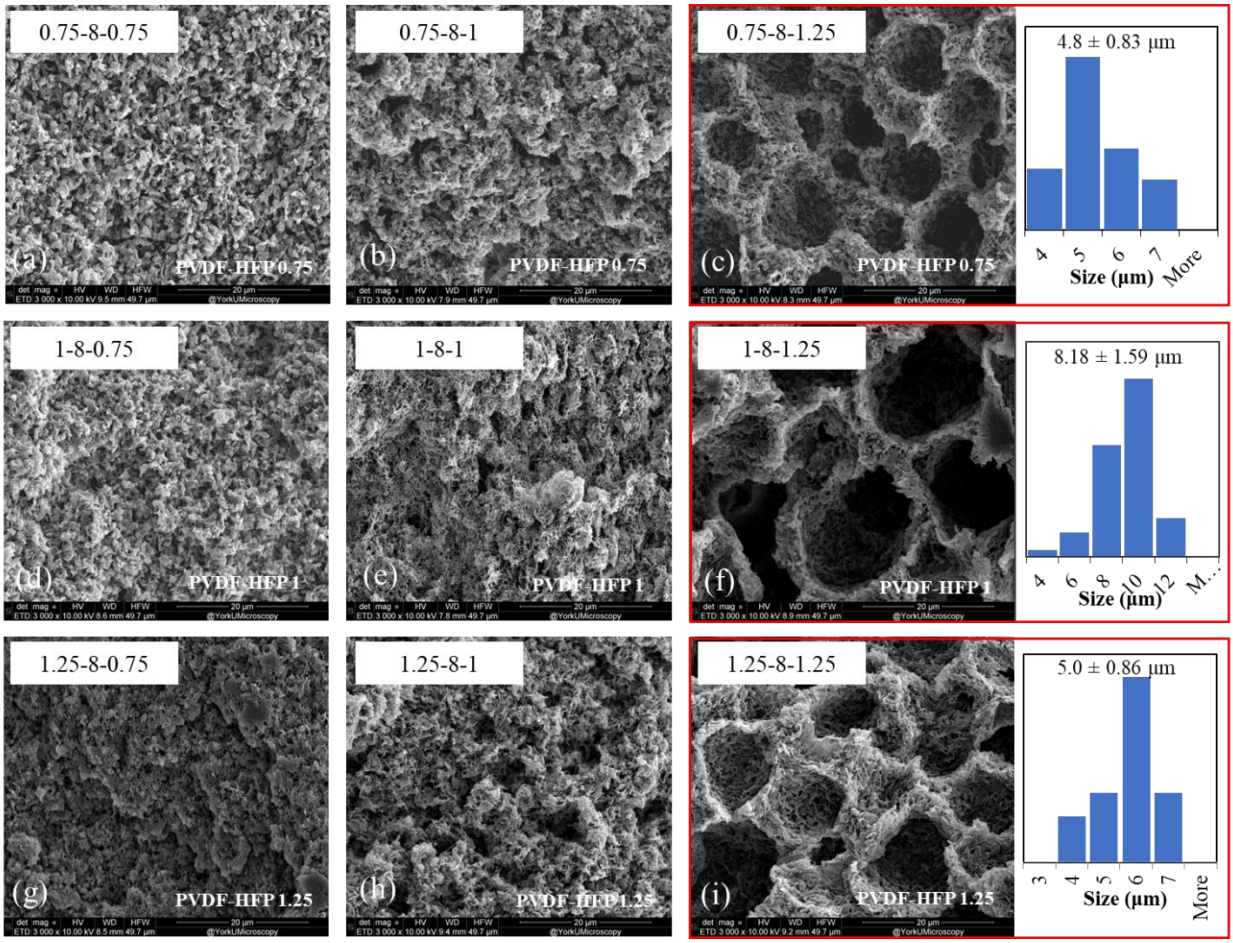


*Figure 5.1. SEM images of the samples with different concentration of the polymer and water at the same magnification.*

### *5.3.2. Solar reflectance: UV-Vis-NIR spectroscopy + Albedo calculations*

Figures 5.2 a-f illustrates the impact of varying water and polymer contents on the reflectivity of the produced hierarchically porous PVDF-HFP samples within the solar energy region (0.3 to 2.5 µm). The tables inset within the figures provide the average solar reflectance ($\bar{R}_{solar}$, albedo) values corresponding to each porous sample obtained using Equation 5.9, offering precise numerical insights into their reflective behavior. The results from Figures 3 a-c depict a clear trend showcasing the influence of water concentration on reflectivity. As the water-to-acetone concentration ratio increases from 0.75 to 1 and 1.25, there is a noticeable rise in reflectivity regardless of the polymer-to-acetone concentration ratio (0.75, 1, and 1.25). This observed

increment underscores the significance of water content in tailoring the reflective properties of the PVDF-HFP material for effective RC. The observed increase in reflectance with elevated water concentrations can be attributed to the micro- and nano-cellular structure formed during the phase inversion process. The introduction of water at higher concentrations contributes to the formation of a more porous structure, leading to increased reflectance. The microporous walls obtained when the water-to-acetone concentration is 1.25 exhibit strong light scattering properties which is attributed to Mie scattering. According to Mie theory, when light interacts with particles comparable in size to their wavelength, scattering contributes significantly to the increased reflectivity. The presence of microporous walls in this specific size range allows for effective scattering of sunlight, enhancing the reflective capabilities of the PVDF-HFP composite. The porous structures created introduce a mismatch in the refractive index between the PVDF-HFP matrix and the air within the pores. This refractive index discontinuity plays a crucial role in strongly scattering light in the solar spectral range. The variation in refractive indices induces multiple light reflections and refractions at the interface between the polymer matrix and the air-filled pores, leading to enhanced light scattering. The observed increase in reflectivity at higher water contents aligns with the structural refinement, as discussed with reference to the SEM images in Section 5.3.1. Conversely, Figures 5.2 d-f reveal a phenomenon where, while holding water content constant, an initial increase in the polymer-to-acetone concentration ratio from 0.75 to 1 leads to an elevation in reflectivity, followed by a subsequent decline upon further increasing the polymer content to 1.25. Higher polymer concentrations may lead to a denser and less porous structure, which can result in reduced light scattering and, consequently, lower reflectance. Figure 5.3 also illustrates how $\bar{R}_{solar}$ varies with increasing water concentration (Figure 5.3 a) and polymer (PVDF-HFP) concentration (Figure 5.3 b). The observed reflectance going above 100% at short wavelengths can occur due to the higher reflectance of the porous samples compared to the reference at shorter wavelengths, and it can be attributed to its optimized design and intrinsic optical properties. The porous material's tailored refractive index and surface morphology enhance its reflectivity in this spectral range. Additionally, the reference material may experience greater absorption or scattering losses at shorter wavelengths, further highlighting the superior performance of the developed bimodal pores sized polymeric materials in this regime.

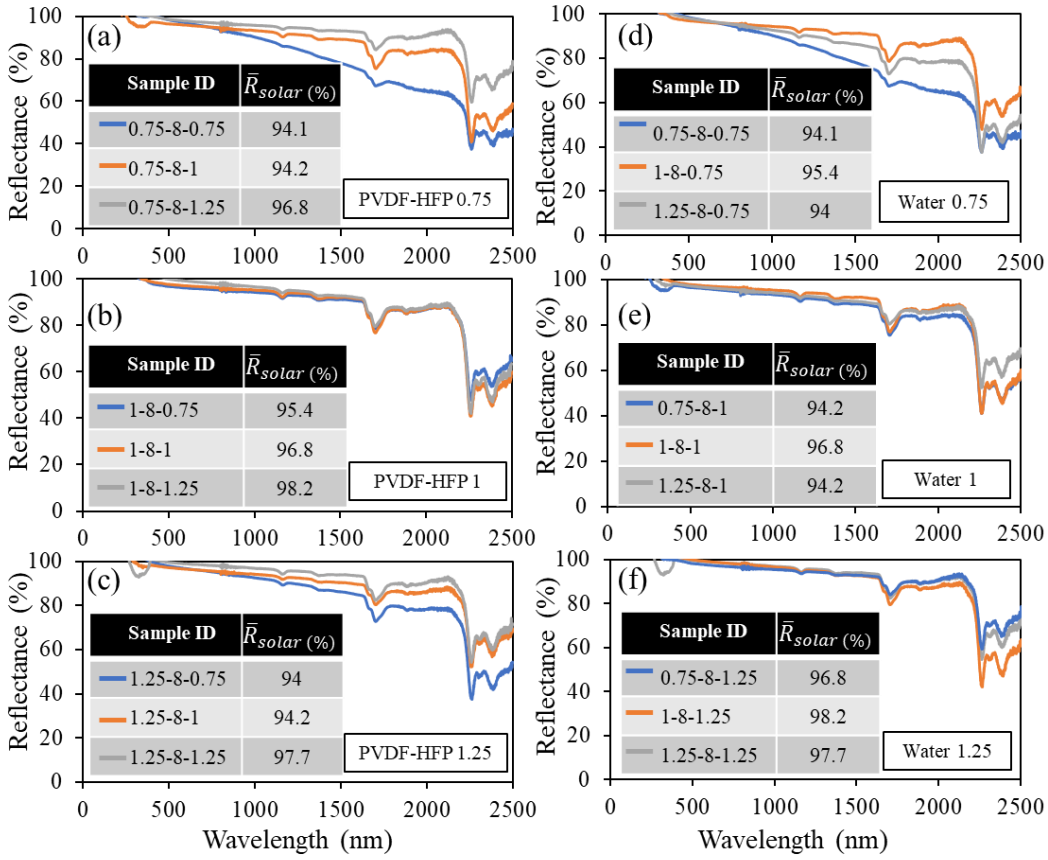


*Figure 5.2. Reflectance from 300 to 2,500 nm measured using UV-Vis-NIR spectroscopy when (a)-(c) the polymer concentration is fixed and the water content used to fabricate the samples changes, and (d)-(f) the water content is fixed, and the polymer concentration used to fabricate the samples changes.*

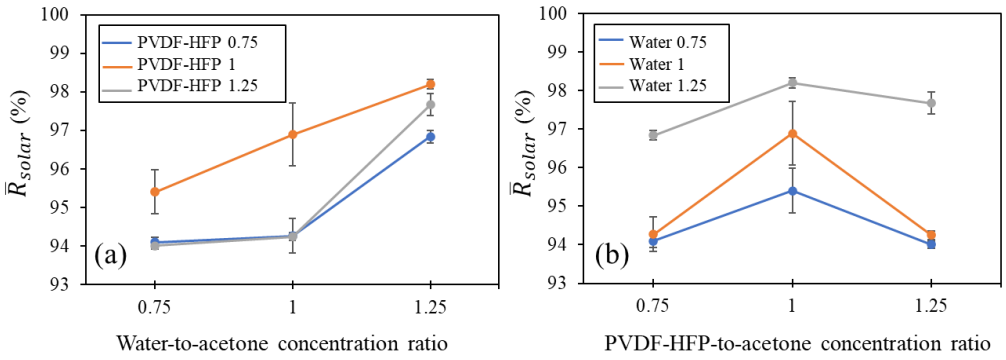


*Figure 5.3. $\bar{R}_{solar}$ of samples as a function of (a) the water concentration and (b) the polymer (PVDF-HFP) concentration used to fabricate the samples.*

### *5.3.3. LWIR thermal emission: FTIR spectroscopy + EM-4 Emissometer*

Figure 5.4 illustrates the spectral emittance of the samples in the LWIR region using FTIR spectroscopy. The insets complement this data by providing information on the average hemispherical emittance ($\bar{\varepsilon}_{LWIR}$) of the samples calculated using Equation 5.10. The molecular structure of P(VDF-HFP), characterized by C–F bonds, exhibits strong vibrational modes in the infrared spectrum. The C-F stretching vibrations in PVDF-HFP typically occur at 1100 $cm^{-1}$, corresponding to a wavelength of approximately 9.09 µm, and at 1200 $cm^{-1}$, corresponding to a wavelength of approximately 8.33 µm. Additionally, the C-F bending vibration appears at 700 $cm^{-1}$, which corresponds to a wavelength of approximately 14.29 µm [181]. Additionally, the porous structure of PVDF-HFP can influence its mid-infrared emissivity to a certain extent. The highest emittance, measured at 98.5%, is associated with sample 1-8-1.25. This notable value underscores the material's effectiveness in emitting infrared radiation within the LWIR region. Furthermore, the total directional emissivity of sample 1-8-1.25, measured at normal direction and 390 K using the Emissometer EM4, is determined to be 99.5%. Correspondingly, the total hemispherical emissivity calculated for sample 1-8-1.25 is 98.9%.

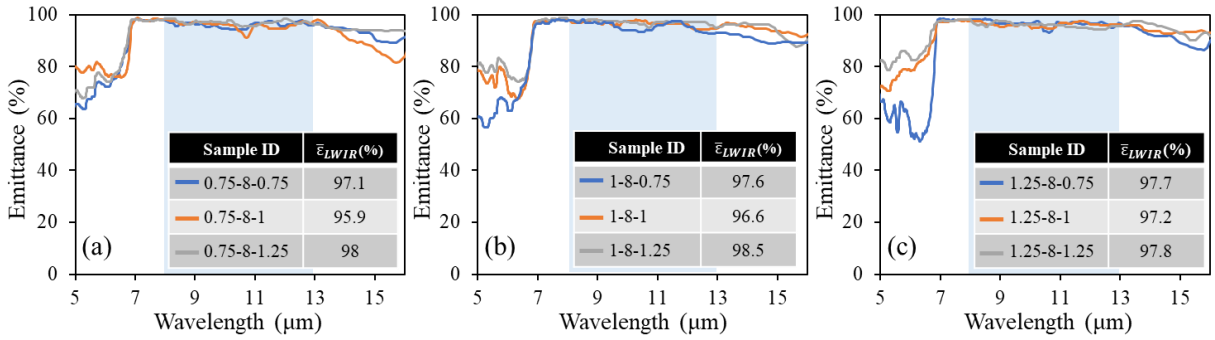


*Figure 5.4. Emittance spectra of the samples obtained using FTIR spectroscopy with the average hemispherical emittance ($\bar{\varepsilon}_{LWIR}$) of the samples calculated using Equation 5.10.*

### *5.3.4. Cooling power calculations*

Figure 5.5 depicts the cooling performance calculations alongside a graph (Figure 5.5 c) summarizing the optical properties (average solar reflectance, $\bar{R}_{solar}$, and average LWIR emissivity, $\bar{\varepsilon}_{LWIR}$) of the samples investigated in this study. In Figure 5.5 a, a bar chart displays the radiative heat transfer from the radiator to outer space ($P_{RC}$), solar energy absorbed by the sample ($P_{solar}$), absorbed atmospheric downward thermal radiation ($P_{atm}$), and the net cooling power, $P_{net,\,Cool}$, which is the cumulative effect of all factors. Negative values for $P_{solar}$ and $P_{atm}$ indicate the absorbed thermal energy by the samples, leading to decreased cooling power. These results are derived under conditions where the convective thermal energy from the ambient surroundings ($P_{Conv.}$) is assumed to be zero ($T_{RC} = T_{amb}$ = 300 K). Notably, sample 1-8-1.25 demonstrates the highest net cooling power ($P_{net,\,Cool}$ = 86 W·m$^{-2}$), correlating with its elevated values of $\bar{R}_{solar}$ and $\bar{\varepsilon}_{LWIR}$, reaching 98.2% and 98.5%, respectively. This indicates that as $\bar{R}_{solar}$ is high, the sample experiences low solar energy absorption, resulting in a decreased $P_{solar}$ and an increased $P_{net,\,Cool}$. Additionally, with an increase in $\bar{\varepsilon}_{LWIR}$, the $P_{RC}$ enhances which increases the $P_{net,\,Cool}$. Figure 5.5 b presents a comparative analysis of the cooling power ($P_{net,\,Cool}$) for the samples as a function of the radiator temperature ($T_{RC}$), considering a heat exchange coefficient of $h$ = 5 W·m$^{-2}$·K$^{-1}$ and $T_{atm}$ = 300 K. The steady-state temperature of the samples, $T_{RC-ss}$, is the equilibrium temperature where the net cooling power equals zero, $P_{net,\,Cool}$ = 0 W·m$^{-2}$. This steady-state temperature is determined by solving Equation 5.1 and can be extracted from Figure 5.5 b. The corresponding values are listed in Table 5.3. Additionally, there is a correlation between the steady-

state temperature of the samples and their optical properties. The lowest steady-state temperature is calculated for sample 1-8-1.25, which has the highest $\bar{R}_{solar}$ and $\bar{\varepsilon}_{LWIR}$ values ($T_{RC-ss}$ = 291 K). This is followed by sample 1.25-8-1.25, which exhibits the second-highest values of $\bar{R}_{solar}$ and $\bar{\varepsilon}_{LWIR}$ (resulting in $T_{RC-ss}$ = 292 K). Furthermore, Figure 5.5 d showcases the net cooling potential of the optimized sample (1-8-1.25) under varying environmental conditions of the convective heat transfer coefficient ($h$), ranging from 0 W·m$^{-2}$·K$^{-1}$ to 12 W·m$^{-2}$·K$^{-1}$, assuming $T_{amb}$ = 300 K. Table 5.4 summarizes the $T_{RC-ss}$ results from Figure 5.5 d for sample 1-8-1.25 across different $h$ values. This underscores the significant impact of the convective heat transfer coefficient on the cooling performance, as higher $h$ values lead to increased ambient thermal influences and consequently higher steady-state temperatures. Conversely, in near-vacuum conditions, where $h$ = 0 W·m$^{-2}$·K$^{-1}$, the sample demonstrates its optimal cooling capability with substantially lower steady-state temperatures. Remarkably, under vacuum conditions, sample 1-8-1.25 potentially exhibits an extraordinary $T_{RC-ss}$ of 281 K.

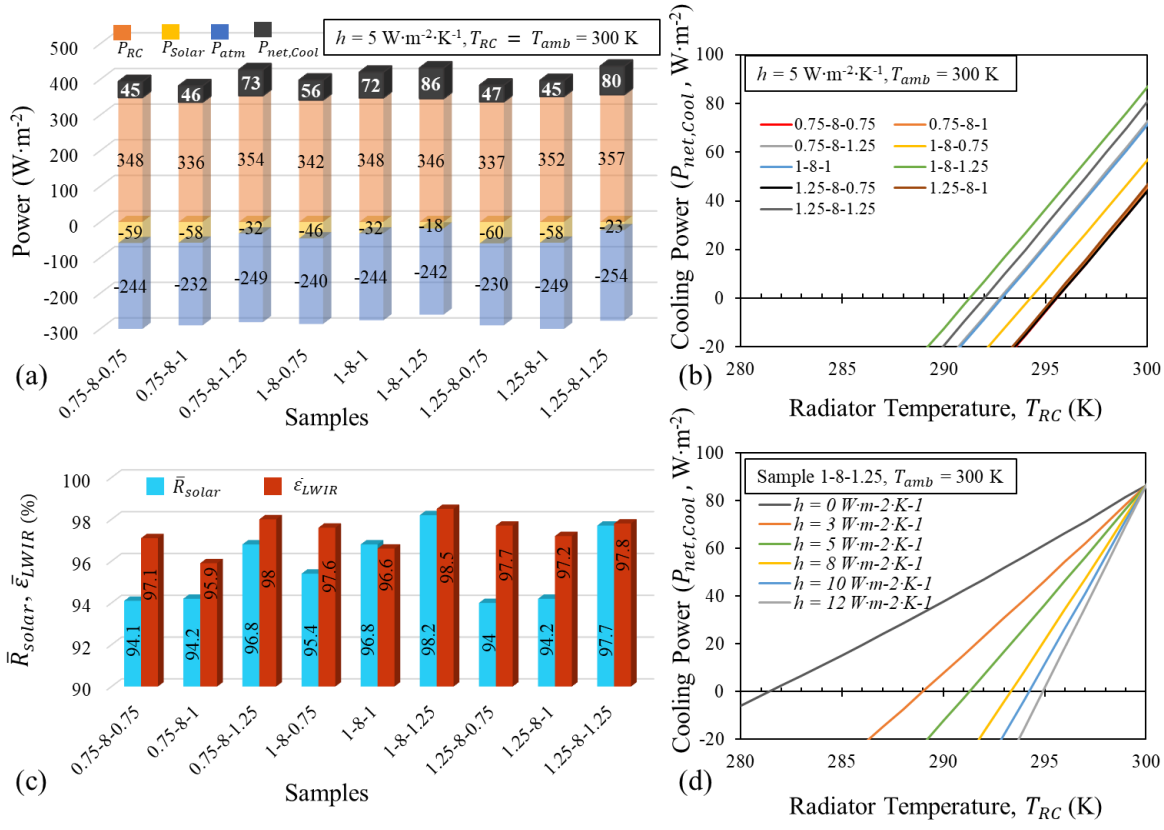


*Figure 5.5. (a) Power parameters involved in daytime RC performance of all samples. (b) Net cooling power ($P_{net,\,Cool}$) for the samples as a function of the radiator temperature ($T_{RC}$). (c) Optical properties*

*($\bar{R}_{solar}$ and $\bar{\varepsilon}_{LWIR}$) of the samples. (d) Net cooling power of the optimized sample (1-8-1.25) under different convective heat transfer coefficient (h) values.*

*Table 5.4.The steady state cooling temperatures ($T_{RC-SS}$) of the samples when $P_{net,Cool}$ = 0, h = 5 W·m$^{-2}$·K$^{-1}$, $T_{amb}$ = 300 K*

| Sample | 0.75-8-0.75 | 0.75-8-1 | 0.75-8-1.25 | 1-8-0.75 | 1-8-1 | 1-8-1.25 | 1.25-8-0.75 | 1.25-8-1 | 1.25-8-1.25 |
|---|---|---|---|---|---|---|---|---|---|
| $T_{RC-SS}$ (K) | 296 | 295 | 293 | 294 | 293 | 291 | 296 | 295 | 292 |

*Table 5.5. The steady state cooling temperatures ($T_{RC-SS}$) of the sample 1-8-1.25 under different h values.*

| $h$ (W·m$^{-2}$·K$^{-1}$) | 0 | 3 | 5 | 8 | 10 | 12 |
|---|---|---|---|---|---|---|
| $T_{RC-SS}$ (K) | 281 | 289 | 291 | 293 | 294 | 295 |

**Steady-State Temperature vs. Cooling Power:** The steady-state temperature as a performance measure for RC material structures directly shows the system's capability to sustain a surface cooled under specific environmental conditions. Steady-state temperature reflects the balance between all the thermal interaction of the RC and the surrounding such as the incoming solar radiation, outgoing thermal radiation, and nonradiative heat exchange with the surroundings, offering a clear metric for the effectiveness of RC materials in real-world applications. This measure is particularly relevant for passive applications where the temperature is playing a huge role like rooftop cooling, where the goal is to reduce surface or interior temperatures sustainably. It provides a direct understanding of how the material will perform under prolonged exposure to ambient conditions.

In contrast, cooling power is a dynamic metric that quantifies the net heat flux (measured in $W \cdot m^{-2}$) removed by the material under specific conditions, such as a set ambient temperature and solar irradiance. Cooling power is valuable for comparing the intrinsic thermal performance of different RC materials and is more versatile for engineering applications where energy balance is critical, such as in heat dissipation for electronics or refrigerated systems.

The relationship between these metrics and applications depends on the priorities of the use case. For example, in building applications, steady-state temperature may be prioritized to ensure consistent cooling over time. In contrast, for refrigeration or industrial systems, cooling power is more relevant to evaluate the material's capacity to offset heat loads under varying operational conditions. Both metrics are interrelated; materials with high cooling power typically achieve lower steady-state temperatures under comparable conditions. However, external factors like thermal mass, convective heat transfer, and environmental variability can affect how closely these metrics correlate, highlighting the need to select the most appropriate metric based on the specific application.

### *5.3.5. Effects of thickness of the RC films*

Figure 5.6 provides comprehensive insights into the effects of thickness variations on the morphology, optical properties, and cooling performance of the RC samples. The SEM images (Figure 5.5 a-d) depict the microstructural characteristics of four samples with identical compositions of water and polymer (1-8-1.25) but differing thicknesses of 320 μm, 612 μm, 726 μm, and 850 μm. Concurrently, bar charts derived from SEM images illustrate the pore size distributions present within each sample. The SEM images illustrate that as the thickness increases from 320 μm to 612 μm, there is some escalation in pore sizes (~ 33%), averaging from 6.82 ± 1.32 μm to 9.10 ± 1.77 μm. However, beyond this thickness range, further increases do not significantly alter pore sizes. In general, the relationship between thickness and pore size can be complex and influenced by multiple factors. In some conditions, thicker layers of polymer solution tend to exhibit larger and more widely distributed pores compared to thinner layers. This phenomenon arises due to prolonged evaporation times, allowing for greater solvent diffusion and subsequent phase separation. As a result, thicker layers may yield materials with coarser pore structures and higher porosity. In other words, thinner samples have a higher surface-to-volume

ratio compared to thicker samples. This means that a larger proportion of the material is exposed to the surrounding environment during evaporation. As a result, solvent evaporation occurs more rapidly at the surface of thinner samples, leading to the formation of smaller pores. Moreover, thinner layers of polymer solution tend to promote more uniform solvent evaporation and phase separation, leading to greater structural homogeneity in the final material. Conversely, thicker layers may exhibit greater variability in pore size and distribution, resulting in a less homogeneous structure. Figures 5.6 e and 5.6 f shows the effects of sample thickness on their solar reflectance and LWIR emittance. There is a rise in both the reflectance and the LWIR emittance of the samples as their thickness increases. Figures 5.6 g also shows $\bar{R}_{solar}$ and $\bar{\varepsilon}_{LWIR}$ values calculated for the 1-8-1.25 samples with different thicknesses (Samples 1-8-1.25_320, 1-8-1.25_612, 1-8-1.25_726, and 1-8-1.25_850). That is, as the thickness of the 1-8-1.25 sample increases from 320 μm to 850 μm, $\bar{R}_{solar}$ increases from 90.3% to 98.2% and $\bar{\varepsilon}_{LWIR}$ increase from 93% to 98.5%, respectively. Thicker samples provide a longer optical path length for incident solar radiation and this increased path length allows for more interactions between the radiation and the material, resulting in higher reflectance. Higher sample thicknesses also typically mean a higher density of polymer material, thereby enhancing $\bar{\varepsilon}_{LWIR}$. Moreover, the abundant presence of a hierarchically porous structure, which alters the effective refractive index and facilitates a smoother transition across the polymer-air interface, improves the impedance matching between the porous polymer and surrounding air and diminishes surface reflectance, thereby consistently enhancing emissivity of the samples in LWIR wavelengths [52].

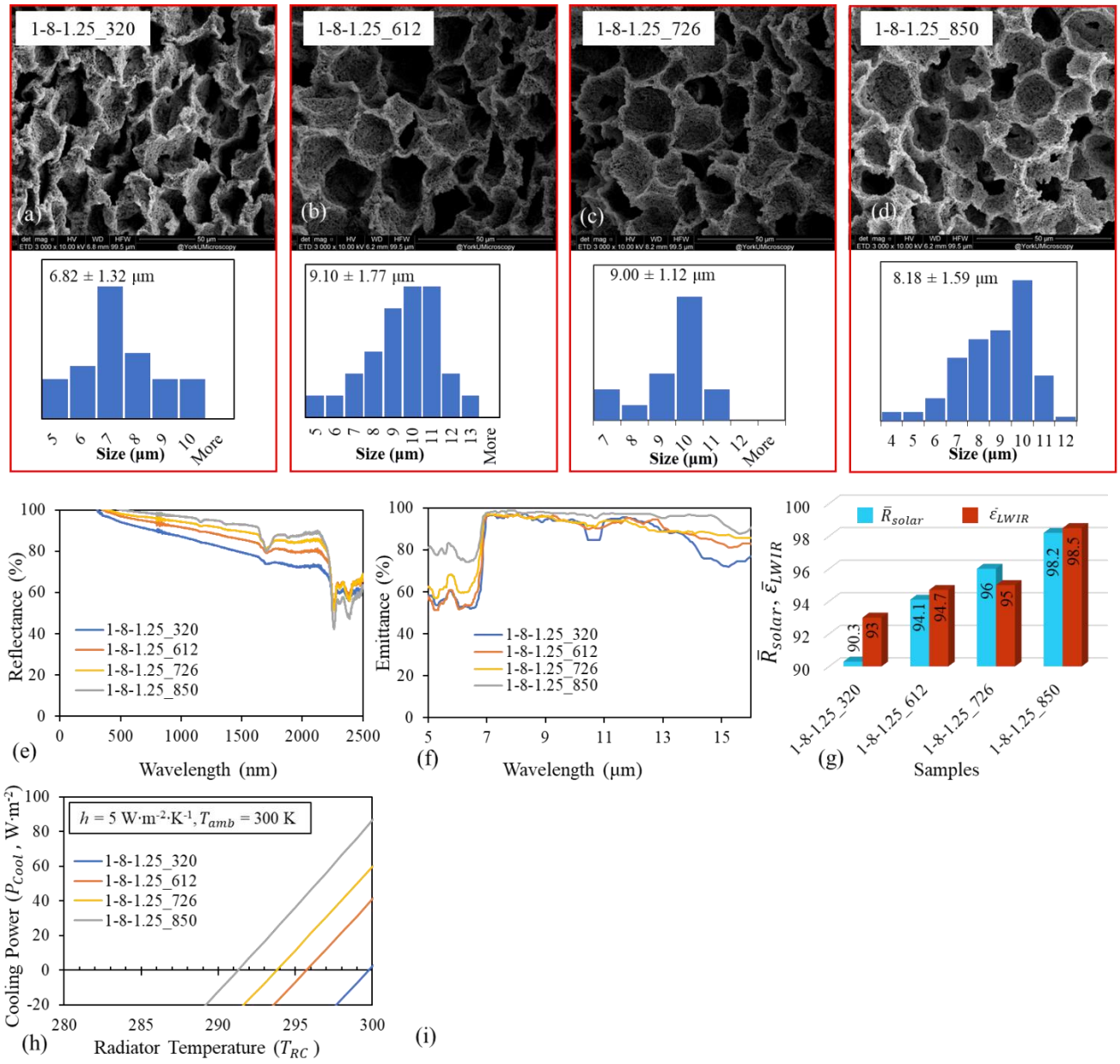


*Figure 5.6. (a)-(d) SEM images, (e)-(g) reflectance, emittance, $\bar{R}_{solar}$, $\bar{\varepsilon}_{LWIR}$ results, and (h) the net cooling power of the sample 1-8-1.25 with different thicknesses.*

## 5.4. Conclusion

This study focuses on the development of effective porous polymeric materials for RC applications, with an emphasis placed on how the tailoring of pore structures can enhance both optical properties and cooling performance. The concentrations of water and polymer, as well as the thickness of the films, were varied to optimize the material characteristics for improved RC

capabilities. In this investigation, adjustments were made to the water-to-acetone and polymer to-acetone ratios to evaluate their impact on the optical and thermal properties of PVDF-HFP hierarchical porous films. It was observed that variations in water concentrations significantly affected pore size, distribution, and density, which in turn influenced the optical properties of the samples, particularly their solar. The sample designated as (1-8-1.25), characterized by a polymer to-acetone ratio of 1 and a water-to-acetone ratio of 1.25, exhibited remarkable optical properties, achieving an average solar reflectance ($\bar{R}_{solar}$) of 98.2% and an average LWIR emittance ($\bar{\varepsilon}_{LWIR}$) of 98.5%. These high values were correlated with a net cooling power ($P_{net,\,Cool}$) of 86 $W \cdot m^{-2}$ under an intense solar irradiance of 1000 $W \cdot m^{-2}$, indicating effective RC capabilities. Significant impacts on pore size and distribution were revealed through the analysis of sample thickness.

# Chapter 6

## 6. Experimental evaluation of outdoor radiative cooling performance and dew condensation via RC

### 6.1. Introduction

This chapter presents the experimental methodologies and setups used to evaluate the performance of RC materials under outdoor conditions and in a controlled environment for dew condensation. The outdoor rooftop experiments were designed to assess the cooling potential of the RC samples by monitoring temperature variations in different configurations, while the indoor setup aimed to simulate dew collection through RC under controlled climate conditions. Both methods are intended to provide a comprehensive understanding of the cooling effectiveness of the porous PVDF-HFP RC materials and also their capability to enhance dew formation, with the potential for applications in energy-efficient systems and water harvesting in arid regions.

The first part of the chapter details the design and implementation of the rooftop experimental setup, where the RC samples are tested alongside blackbody references. Different scenarios are considered to isolate and compare the RC effects, including the use of mirrors, insulation, and parabolic reflectors. The second part focuses on the dew condensation experiments carried out in a climate-controlled chamber, simulating nocturnal conditions. The experimental setups and

procedures provide a framework for assessing the performance of RC materials in practical applications.

## 6.2. Methods

### *6.2.1. Outdoor radiative cooling performance*

To evaluate the cooling potential of the developed RC material structures, an outdoor rooftop experimental setup was designed (Figure 6.1). This setup consists of several test configurations to compare the RC effects under varying conditions. The following cases were tested:

I. **Parabolic Reflector Embedding RC:** The RC sample, a 2 cm diameter disk, is positioned at the focal point of a parabolic dish from Opti-Forms, Inc. (Model P25-300). This parabolic dish has an outer diameter of 6.072 inches (15.42 cm), a focal length of 1 inch (2.54 cm), and is made of electroformed nickel with an $SiO_2$ (AQ) thin-film coating, providing a highly reflective surface with excellent optical properties. The RC sample is mounted on a thin needle, maximizing exposure to direct radiative heat transfer.

II. **Parabolic Reflector Embedding Blackbody:** A 2 cm diameter blackbody reference sample, made of aluminum oxide blackbody tape, is placed at the focal point of an identical P25-300 parabolic dish from Opti-Forms, Inc. This configuration allows for a direct comparison of the cooling effects between the RC sample and an ideal blackbody. The blackbody sample is also mounted on a thin needle for precision positioning.

III. **Parabolic Blackbody Embedding RC:** The RC sample (2 cm in diameter) is placed at the focal point of a parabola with the same dimensions of the P25-300 parabolic dish from Opti-Forms, Inc. coated with blackbody tape (aluminum oxide-based). This setup allows the blackbody coating to influence heat absorption and emission, contrasting with the reflective parabolic setup to analyze the effect on radiative cooling.

IV. **Flat Reflector Embedding RC:** The RC sample, a 2 cm diameter disk, is positioned on a needle at the center of a flat reflective aluminum square mirror (50 cm side length with 5 cm edges) from Anomet Inc. This mirror is crafted from anodized reflective aluminum,

offering high durability and enhanced solar reflectivity to simulate an infinite flat reflective surface beneath the RC sample.

V. **Flat Blackbody Embedding RC:** The RC sample (2 cm diameter) is mounted on a needle and placed at the center of an identical 50 cm square flat surface covered with blackbody tape (aluminum oxide). This configuration serves to compare the cooling performance of the RC material on a reflective surface versus a blackbody-coated surface, highlighting differences in heat transfer behavior between the two surfaces.

The radiative cooling (RC) performance of sample 1-8-1.25 (850 μm in thickness) was measured from 5:00 PM on October 11th, 2024, to 5:30 PM on October 12th, 2024. This continuous thermal measurement was conducted on the flat roof of the five-story Bergeron Centre for Engineering Excellence under clear sky conditions in Toronto, Canada. Both the RC and blackbody samples were disks with a diameter of 2 cm. Omega J-type thermocouples, applied with thermoconductive paste, were attached to measure temperatures directly beneath the samples and in the surrounding air. Environmental conditions, including relative humidity and wind speed, were monitored using an Extech SDL350 data logger, while hemispherical solar irradiance was measured using a Hukseflux SR05 pyranometer. This setup allowed for the accurate recording of air temperature, sample temperature, and solar irradiance over time, with the apparatus positioned on a rooftop to reflect realistic outdoor conditions.

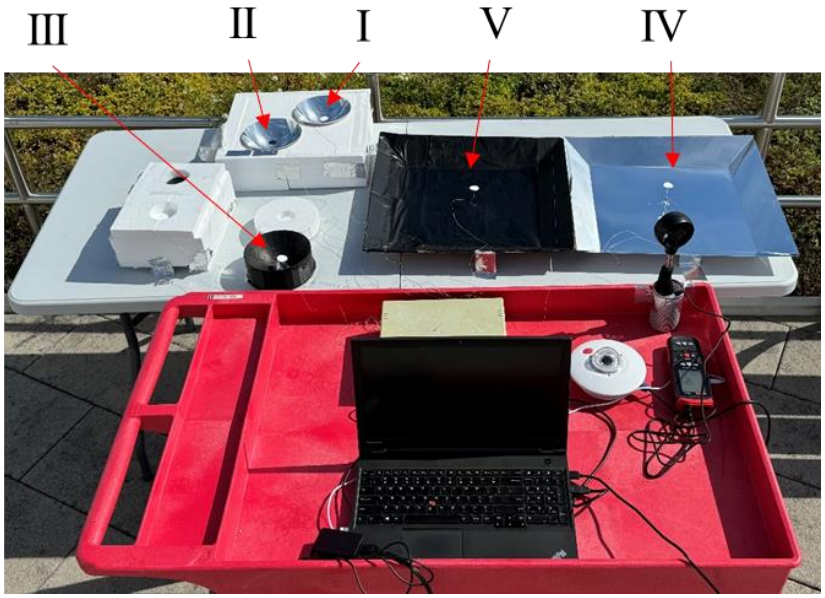


*Figure 6.1. Experimental setup for evaluating radiative cooling performance of various configurations.*

### *6.2.2. Dew condensation experimental setup*

Herein, the experimental setup and methods to produce dew collection via RC are described. This setup, developed by the LIED group (UMR 8236 Laboratoire Interdisciplinaire des Energies de Demain) at Université Paris Cité following the initial design by Trosseille et al. [182], aims to overcome the limitations of outdoor experiments, such as weather variability, experiment duration, and associated costs. The setup tests the ability of samples to collect dew via the RC process in a controlled indoor environment. The device developed by the LIED group replicates the natural phenomenon of radiative dew formation in a laboratory setting by using radiative exchange with a cold source in a climate-controlled chamber. This setup allows for the collection of quantitative data on the dynamics of the dew formation process. The basic requirements for simulating natural dew include exposing the condensation surface (also known as the "dew collector") to an exclusively radiative thermal deficit and surrounding it with humid air at controlled temperature and relative humidity. A high content of water vapor in the air is essential to mimic nocturnal conditions. Figure 6.2 illustrates the setup and provides a schematic representation of its developed components. The experimental setup consists of the following components:

**Climate-Controlled Chamber (1)**: Controls the climate conditions, with the temperature set at 30˚C and the humidity at 90%.

**Cold Source (2)**: Solid carbon dioxide (dry ice) is used as the cold source. Dry ice pellets in the form of cylinders with a thickness of about 1 cm and length of 1 to 5 cm are stored in a Styrofoam box. The temperature of dry ice in equilibrium with its vapor at atmospheric pressure is 194.7 K, ensuring a constant temperature of the cold source. During sublimation, no liquid carbon dioxide is formed, simplifying its use. Although the sublimation rate is low, refilling the vessel every few hours is necessary to maintain a near-constant dry ice level and stabilized radiative heat flux. When exposed to room humid air, dry ice pellets become covered by a layer of frozen water forming ice crystals, which may affect the surface temperature. Despite this layer, no significant modification of the RC power is observed. The ice water emissivity is approximately $\varepsilon g \approx 0.98$, and the presence of water crystals suggests diffuse emission of infrared light, allowing the cold source to be considered as a black body. Additionally, the density of $CO_2$ in its gaseous form at 194.7 K is higher than the density of air, causing the cold $CO_2$ vapor to flow downward and not disturb the window situated above the cold source.

**Dew Collector (3)**: The RC samples used for testing, placed on a sample holder (4) inside the cylindrical chamber.

**Sample Holder (4)**: Holds the dew collector, with dimensions of $3\times3\times1$ $cm^3$.

**Cylindrical Chamber (5)**: A chamber with a height of 10 cm and an internal diameter of 8 cm, covered with aluminum inside to facilitate radiative exchange between the cold source and the RC samples located atop the sample holder.

**Balance (6)**: Measures the mass of condensed water placed underneath the sample holder.

**IR Transparent Double Windows (7)**: Separates the chamber from the cold source, allowing radiative heat exchange while preventing humid air from condensing on the window. Ventilation is provided to flow the air and prevent condensation on the window, which could limit the heat exchange between the cold source and the RC samples.

**Reflector Cap (8)**: An aluminum-covered cap placed upon the cylindrical chamber, facilitates the radiative exchange between the cold source and the RC samples by allowing the RCs to "see" the cold source.

**IR Camera (9)**: Captures the internal conditions and condensation process within the chamber.

**Thermocouples and Sensors (10)**: Attached to different locations inside the cylindrical chamber, the sample holder, and inside the climate-controlled chamber outside the cylindrical chamber to measure heat radiative and thermal flux and temperatures at various points.

The RC samples (dew collector) are cleaned and placed on the sample holder inside the cylindrical chamber. The chamber is then sealed with the IR transparent double windows. The air temperature and relative humidity are set to 30˚C and 90%, respectively. The cold source including dry ice is placed under the cylindrical chamber. The balance measures the mass of condensed water, while thermocouples and sensors record the temperatures of the air, the dew collector, and various points inside and outside the cylindrical chamber. The cold source, which simulates the nocturnal sky, is positioned beneath the dew collector. To enhance radiative exchange above the sample, both the interior of the cylindrical chamber and the cap are lined with aluminum. This aluminum lining effectively directs the radiation emitted by the dew collector towards the cold source. An IR camera captures the internal conditions and condensation process within the chamber. This setup enables precise control and measurement of dew formation, allowing for the thorough testing and analysis of different samples under simulated nocturnal conditions.

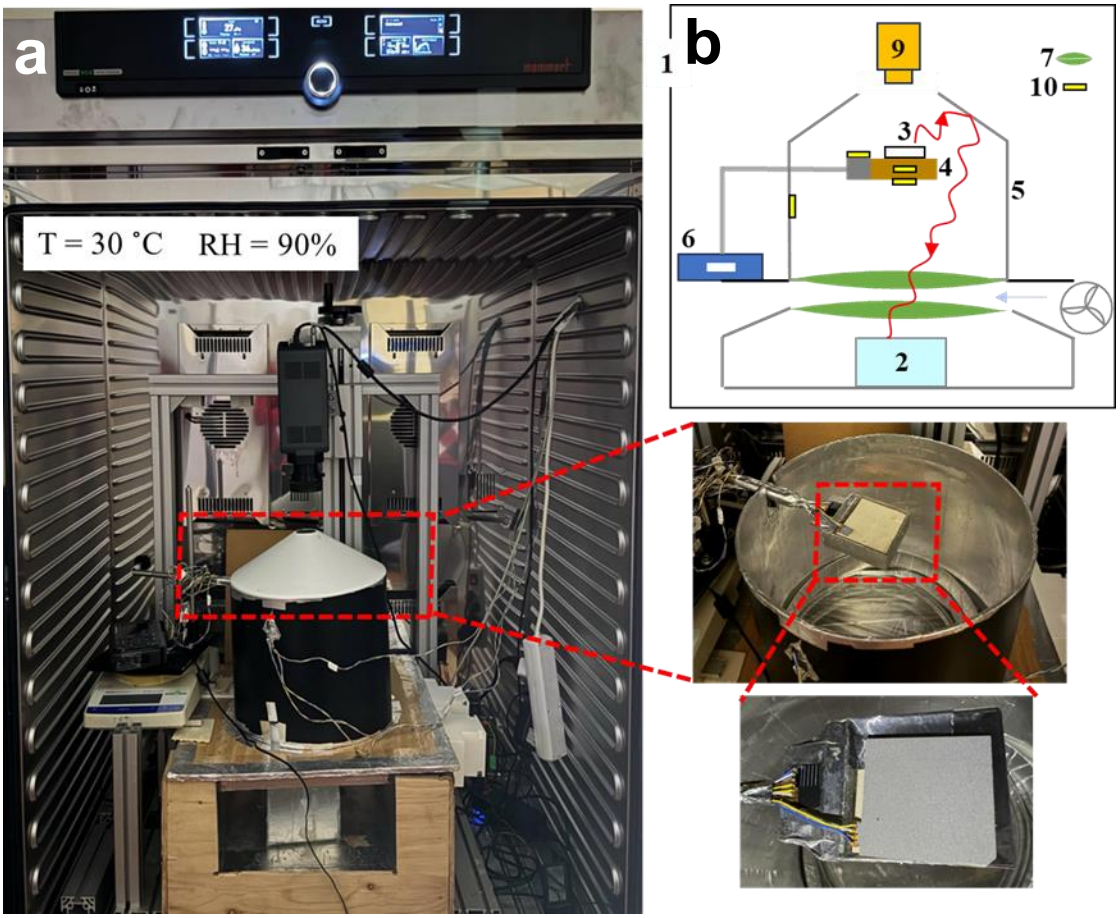


*Figure 6.2. Experimental setup (a) and schematics of the components (b). 1: Climate-Controlled Chamber; 2: Cold source; 3: Dew collector (RC samples); 4: Sample holder; 5: IR reflective cylindrical chamber; 6: Balance; 7: IR transparent double windows; 8: IR Reflector cap; 9: IR camera; and 10: Thermocouples and radiative and thermal sensors.*

## 6.3. Results

### *6.3.1. Outdoor RC measurement results*

Figure 6.3 shows the temperature variation (˚C) over time for different configurations involving RC materials and blackbody structures. The x-axis represents the time of day, while the y-axis displays temperature (˚C). The experimental setups include various configurations of RC and blackbody materials embedded within flat or parabolic reflectors, and ambient air temperature is also measured as a reference.

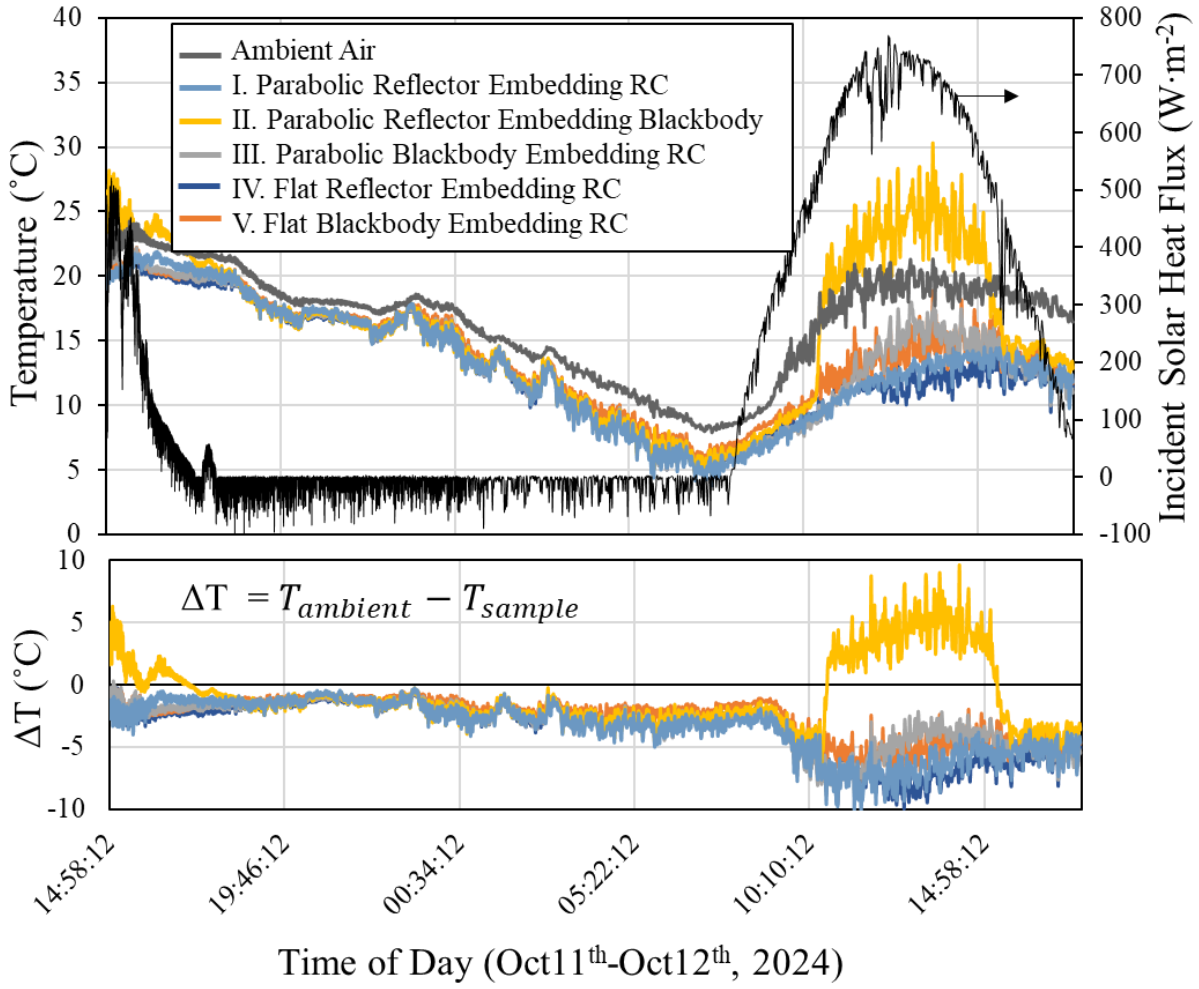


*Figure 6.3. (a) Temperature variation (˚C) over time (b) thermal reduction compared to the ambient for different configurations of RC materials and blackbody structures embedded within reflective and blackbody flat and parabolic under surfaces.*

From the beginning of the experiment to early morning (approximately 17:00 to 07:00), where the external heat source (sunlight) diminishes, the Parabolic Reflector Embedding RC (I: light blue line) stands out as achieving the lowest absolute temperature among all setups (5 ˚C). However, it's important to note that the difference between the structure temperatures and the ambient air (dark gray line), or the ΔT, is not the highest during this period (ΔT = -3.5 ˚C, the negative sign shows the cooling effects). This means that, although the absolute cooling effect is prominent, the relative cooling compared to the ambient air might not be the most significant. Here's a breakdown:

- The ambient air temperature (dark gray line) decreases slowly as the environment cools down, starting at approximately 22 ˚C (17:00) and reaching around 9.5 ˚C (7:00).
- The Parabolic Reflector Embedding RC (I: light blue line) case maintains the lowest temperature throughout the night, exhibiting consistent cooling.
- The Flat Reflector Embedding RC configuration (IV: dark blue line) follows closely behind the Parabolic Reflector Embedding RC (I: light blue line) in terms of cooling performance, although the material structure does not reach as low of a temperature as the Parabolic Reflector.
- The blackbody configurations (II. Parabolic Reflector Embedding Blackbody, yellow line, III. Parabolic Blackbody Embedding RC, light gray line, and V. Flat Blackbody Embedding RC, orange line) also experience cooling, but to a lesser extent. In the configurations where the blackbody material substitutes the RC material, the blackbody exhibits a high emissivity (100%) within the atmospheric window (8–13 μm). This high emissivity enables the blackbody to effectively radiate thermal energy into the sky, facilitating RC during nighttime. However, the blackbody's broadband emissivity is not restricted to the atmospheric window alone; it also possesses high emissivity across other spectral bands. As a result, while the blackbody efficiently radiates energy outward, it also absorbs a significant amount of the downwelling atmospheric radiation, even in the absence of direct solar radiation. The blackbody undersurfaces also absorb and re-radiate heat effectively, leading to higher temperatures throughout the night compared to the reflective configurations.

As sunlight returns, the heating phase begins (07:00–12:00), with temperatures rising in all setups after approximately 07:00. This configuration maintains the lowest temperatures among all setups, outperforming even the flat reflector setup. However, the rate of temperature increase differs between configurations based on their material properties and interaction with solar radiation.

- The Parabolic Reflector Embedding Blackbody configuration (II, yellow line) exhibits the steepest increase in temperature, reaching nearly 30 ˚C by noon when the ambient temperature is around 20 ˚C. This rapid heating reflects the high absorption capacity of the blackbody material, particularly when combined with the parabolic reflector that focuses

solar radiation onto the surface. The sharp rise in temperature demonstrates how blackbody materials, while effective at radiating heat at night, are highly susceptible to solar heating during the day.

- Conversely, the Parabolic Reflector Embedding RC (I: light blue line) shows slower temperature increase with a maximum ΔT of -10 ˚C compared to the ambient at around 11:30. The Flat Reflector Embedding RC configuration (IV: dark blue line) follows closely behind the Parabolic Reflector Embedding RC (I: light blue line) in terms of cooling performance. This indicates the superior cooling capacity of RC materials in reducing the impact of solar heating, particularly when combined with a reflective surface. The parabolic shape assists in dissipating downwelling radiation from the atmosphere. The atmosphere continuously emits longwave infrared radiation back towards the Earth's surface, which can potentially be absorbed by cooling materials and reduce their cooling efficiency. However, the parabolic reflector structure redirects much of this downwelling atmospheric radiation away from the RC material. And due to reciprocity, it just redirects the normal incident atmospheric radiation towards the RC.

During the afternoon and early evening, from 1:00 PM until around 16:00, the Flat Reflector Embedding RC (IV: dark blue line), with a maximum ΔT of -9 ˚C, outperforms the Parabolic Reflector Embedding RC (I: light blue line), with a maximum ΔT of -8.5 ˚C. The shift in performance is largely attributed to the orientation of the setups relative to the sun's position in the sky, which leads to differences in how solar radiation interacts with the reflectors and the RC material. The parabolic shape, which typically aids in RC by focusing outward radiation, might unintentionally focus incoming solar radiation on the RC surface at certain angles of incidence. This unintended solar concentration raises the surface temperature of the RC material, reducing its cooling efficiency during the later hours of the day. The Flat Reflector Embedding RC configuration, by contrast, maintains a more consistent performance in the afternoon and evening. The flat surface evenly reflects incident solar radiation, preventing any concentration of sunlight on the RC material. This ensures that the RC surface remains protected from solar heating, allowing it to continue dissipating heat through RC. As a result, the flat reflector setup exhibits a better cooling performance than the parabolic configuration during the afternoon and evening, even though both setups outperform the ambient air temperature. After 16:00 until the experiment

ends, the Parabolic Reflector Embedding RC (I: light blue line) again shows the best cooling performance.

### *6.3.2. Dew condensation results*

This section presents the quantitative results of radiative condensation experiments conducted on RC samples. The specific material tested is Sample 6_850, 1-8-1.25, characterized by a thickness of 850 μm and the highest recorded values of solar reflectance ($\bar{R}_{solar}$ = 98.2%) and long-wave infrared emittance ($\bar{\varepsilon}_{LWIR}$ = 98.5%). During the condensation experiment, the air conditions inside the climate-controlled chamber are maintained at a temperature of 30 ˚C and a relative humidity of 90%.

Figure 6.4 illustrates the temperature profiles obtained from thermocouples placed at three different locations within the setup: two thermocouples ($T_1$ and $T_2$) are positioned on the interior wall of the cylindrical chamber, while one thermocouple ($T_3$) is situated outside the cylindrical chamber in the climate-controlled chamber. The data in Figure 8 demonstrate that the air temperatures both inside and outside the cylindrical chamber stabilized after approximately 2000 seconds. Minor fluctuations in temperature are observed, which can be attributed to the ambient room temperature thermostat-based control system, which regulate the surrounding environment and can cause slight variations in room temperature. The temperatures recorded by $T_1$ and $T_2$, located inside the cylindrical chamber, are slightly lower than those recorded by $T_3$. This difference is due to the radiative thermal exchange occurring between the RC sample and the cold source situated below the cylindrical chamber. The thermocouple placed outside the cylindrical chamber ($T_3$) reflected the general climate conditions maintained in the chamber. The stabilization of temperature readings indicates that the experimental setup effectively simulates the set conditions necessary for studying radiative condensation on the RC samples.

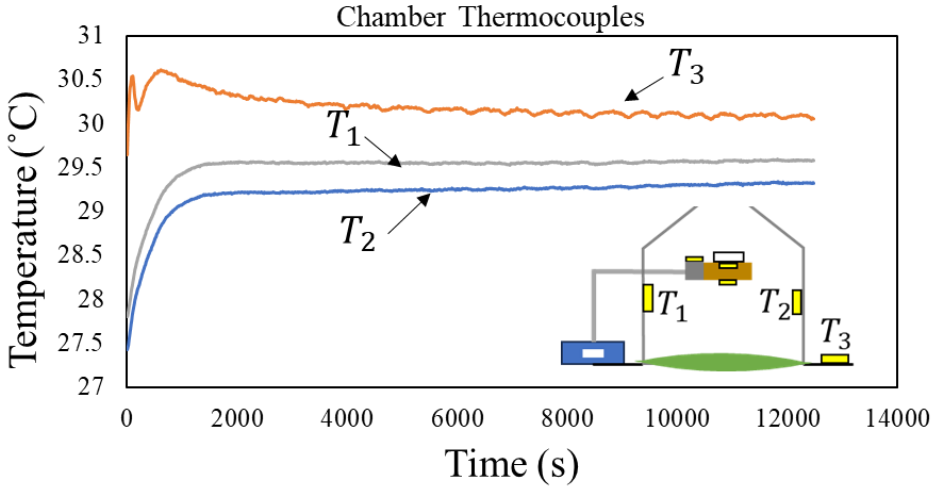


*Figure 6.4. Temperature profiles measured by thermocouples at three different locations within the experimental setup. Thermocouples T1 and T2, located inside the cylindrical chamber with thermocouple T3, positioned outside the cylindrical chamber within the climate-controlled environment.*

Figures 6.5 and 6.6 demonstrate the temperature and heat flux results obtained from heat flux/thermocouple sensors placed at different locations around and inside the sample holder situated in the centre of the cylindrical chamber during a condensation experiment. The specific heat flux/thermocouple sensors and their locations are as follows:

$T_{Cond,atop}$ and $P_{Cond,atop}$ = Temperature and heat flux, respectively, from the conductive sensor located at the top of the sample holder attached beneath the RC sample

$T_{Con+Rad,atop}$ and $P_{Con+Rad,atop}$ = Temperature and heat flux, respectively, from the global (convective + radiative) heat flux sensor atop the sample holder

$T_{Rad,atop}$ and $P_{Rad,atop}$ = Temperature and heat flux, respectively, from the radiative heat flux sensor atop the sample holder

$T_{Con+Rad,under}$ and $P_{Con+Rad,under}$ = Temperature and heat flux, respectively, from the global heat flux sensor under the sample holder

According to Figure 9, $T_{Con,atop}$ is in direct contact with the RC sample and shows the lowest temperature profile. This is attributed to the radiative heat exchange between the RC sample and

the cold source, resulting in significant cooling. $T_{Con+Rad,atop}$ and $T_{Con+Rad,under}$ measure the combined effects of radiation and convection on the top and bottom surfaces of the sample holder. Both sensors exhibit nearly identical temperatures, indicating uniform thermal conditions on both sides of the sample holder. This uniformity reflects the effectiveness of the aluminum-lined cap in directing radiation toward the cold source. However, $T_{Con+Rad,under}$ records slightly lower temperatures than $T_{Con+Rad,atop}$ due to its direct thermal exchange with the cold source, however, considering an uncertainty of 0.5 ˚C it can be interpreted as identical values showcasing the uniformity of the thermal conditions in the chamber. $T_{Rad,atop}$, measuring the radiative heat exchange, shows a distinct temperature profile. It reaches lower temperatures compared to $T_{Con+Rad,atop}$ and $T_{Con+Rad,under}$ because it does not account for convective heat transfer from the ambient environment, maintained at around 30 ˚C. In general, the collected data elucidate the different impacts of conductive, convective, and radiative heat transfer mechanisms on various parts of the sample holder.

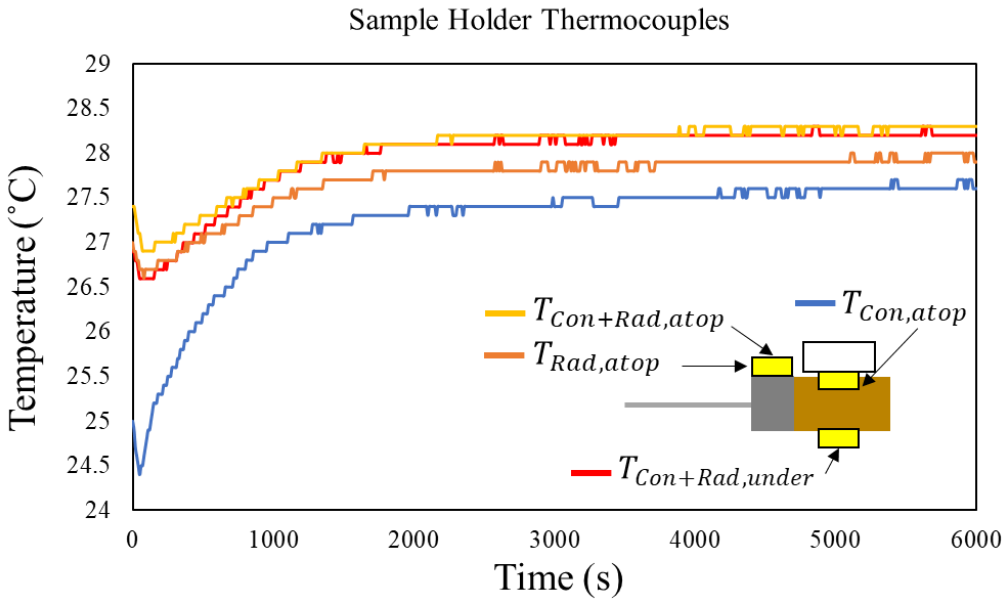


*Figure 6.5. Temperature evolution at different locations during a condensation experiment, obtained using heat sensors.*

As shown in Figure 10, the global flux sensor, $P_{Con+Rad,under}$ flux sensor, starts with a high cooling flux, -100 W·m$^{-2}$ with the negative sign due to cooling, indicating significant heat loss due to its direct contact with exposure to the cold source. The negative sign indicates cooling. Over time, this value decreases to a final value of -60 W·m$^{-2}$, suggesting that while the cooling effect decreases over time, it remains substantial, indicating continuous heat loss to the cold source. $P_{Rad,atop}$ shows higher cooling powers than $P_{Con+Rad,atop}$ as it just shows the radiative flux neglecting the convective heat transfer. The radiative flux sensor ($P_{Rad,atop}$) exhibits higher cooling power compared to the global flux sensor ($P_{Con+Rad,atop}$). This difference arises because $P_{Rad,atop}$ measures only the radiative heat transfer, excluding the convective heat transfer occurring within the chamber. $P_{Con,atop}$, conductive sensor, shows fluctuating heat loss initially, which stabilizes to zero, indicating that the RC sample's temperature reaches equilibrium with the surrounding environment. The initial cooling suggests the RC sample was losing heat, but as it approaches the steady state temperature, the net heat flux stabilizes.

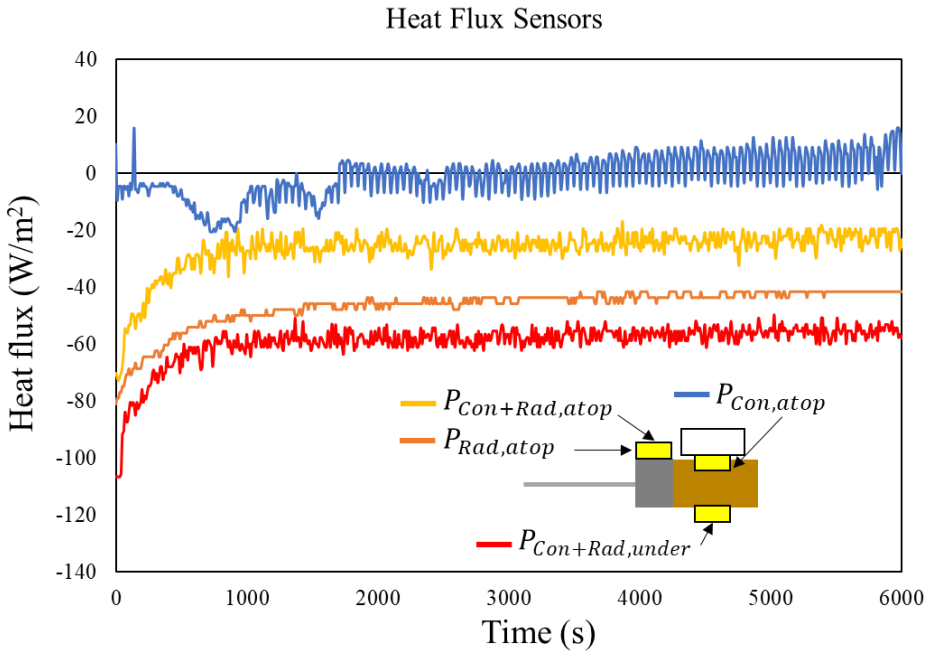


*Figure 6.6. Heat flux evolution of different spots measured by various sensors during the condensation experiment.*

Figure 6.7 illustrates the measured mass of condensed water over time during the experiment. It corresponds to the total mass condensed on all exposed surfaces, including the RC surface, as well as the lateral and bottom surfaces of the sample holder. Initially, the mass increases non-linearly until approximately 2400 s, after which it reaches a steady state with a constant condensation rate of $4\times10^{-5}$ g·s$^{-1}$. These results are consistent with findings reported in other studies [182][183]. The initial non-linear increase can be attributed to a transient phase caused by (i) the establishment of a new energy balance initiated by the release of latent heat from condensation, and (ii) the delayed condensation on the lateral surface of the sample holder, which has lower emissivity and thus a higher temperature compared to the RC sample.

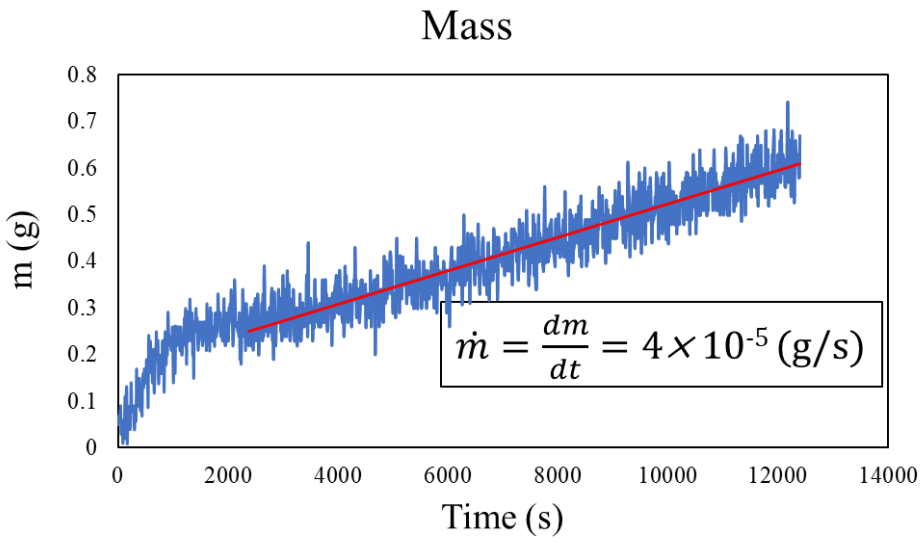


*Figure 6.7. Evolution of the water mass condensed on the RC sample during the RC experiment.*

## 6.4. Conclusion

The temperature variation results in this section for the outdoor RC performance setups provide valuable insights into the effectiveness of various configurations involving RC materials and blackbody structures. During the nighttime (17:00 to 07:00), the Parabolic Reflector Embedding RC configuration achieves the lowest temperature of 5 ˚C, with a relative cooling effect of ΔT = -3.5 ˚C compared to the ambient air. The Flat Reflector Embedding RC setup also performs well, while the blackbody configurations exhibit less effective cooling due to higher absorption of atmospheric radiation. In the heating phase (07:00–12:00), the Parabolic Reflector Embedding

Blackbody configuration shows the fastest temperature increase, reaching nearly 30 ˚C by noon. In contrast, the RC configuration demonstrates a cooing effect with a maximum ΔT of -10 ˚C around 11:30. Notably, the Flat Reflector Embedding RC configuration outperforms the Parabolic Reflector in the afternoon and early evening, indicating the importance of orientation and solar interaction for optimizing cooling performance. Overall, these findings highlight the complex interactions between RC materials, their configurations, and environmental factors.

In the dew condensation experiments, the results from Sample 6_850 demonstrate the effectiveness of RC materials in facilitating water condensation. The temperature profiles obtained from thermocouples within the experimental setup reveal that the air temperatures inside the cylindrical chamber ($T_1$ and $T_2$) are consistently lower than those measured outside ($T_3$), indicating effective thermal exchange with the cold source. The stabilization of these temperatures after approximately 2000 seconds suggests that the experimental conditions were well-maintained, allowing for accurate assessment of radiative condensation. The heat flux data illustrate the dynamics of conductive, convective, and radiative heat transfer, with $P_{Rad,atop}$ showing higher cooling powers compared to $P_{Con+Rad,atop}$, underscoring the dominant role of radiative heat transfer in cooling. Furthermore, the mass of condensed water measured over time exhibits a steady state with a constant condensation rate of $4\times10^{-5}$ g·s$^{-1}$ after an initial non-linear increase, attributed to the establishment of a new energy balance and the varying thermal properties of the surfaces involved. These findings affirm the potential of RC materials for enhancing dew condensation processes, contributing to sustainable water harvesting solutions.

# Chapter 7

## 7. Conclusion and future work

### 7.1. Conclusion

In light of the escalating global environmental issues, such as climate change, urban heat islands, and rising energy demands, innovative solutions are urgently needed to address these challenges. The overarching goal of this thesis was to explore and analyze novel configurations of micro and nano-structured materials with controlled radiative properties for effective RC applications. In this thesis, the aim was to design effective underside reflectors to enhance RC performance. The use of underside reflectors was pursued to minimize radiative losses and increase the cooling effect by directing thermal emissions towards the atmospheric window while limiting exposure to both solar irradiance and atmospheric radiation. This design approach was based on the fact that atmospheric transmittance decreases with increasing zenith angle, making surfaces with normal aligned directly upwards more effective in RC. By incorporating reflectors, radiative heat loss to the atmosphere was reduced, thereby enhancing the system's overall efficiency. Furthermore, highly reflective and LWIR-emissive porous PVDF-HFP samples were fabricated using the phase inversion method. These samples were engineered to maximize solar reflectance and longwave infrared emissivity,

promoting enhanced net cooling power. The porous structure of the PVDF-HFP was developed to create a hybrid micro- and nano-cellular matrix that efficiently scatters and emits thermal radiation, making it an ideal material for passive daytime RC applications. It was also aimed to investigate the potential of RC technologies to mitigate climate change by reducing global warming potential (GWP) and lowering cooling energy demands. The work sought to address both theoretical and practical aspects of the RC material structures, from their fundamental cooling mechanisms to real-world applications. By examining various configurations and materials, this research aimed to provide a holistic understanding of how RC technologies can be implemented to enhance environmental sustainability.

The objectives of this thesis following with the methods utilized and the results obtained for each objective were as follows:

1. **To develop Life Cycle Assessment methods for RC technologies and to determine the impact of RC on the global warming potential in geoengineering applications**: The goal was to quantify the GWP reduction associated with RC materials, considering both direct RC effects and indirect reductions in cooling loads. Further, the impacts of covering broad areas (about 1% of Earth's surface) with high-performance RC materials on terrestrial radiative forcing was determined.

   **Methods (LCA, GWP, and RF Analysis**): By employing LCA techniques, this thesis compared RC materials' environmental impact to that of traditional construction materials. it focused on evaluating the performance of RC materials by determining their net cooling power, GWP, and radiative forcing. The net cooling power serves as a crucial metric for assessing the effectiveness of RC technologies in providing cooling benefits. By analyzing the balance between the cooling effects of thermal radiation emitted from the RC materials and the various heat gains from solar radiation, convection, and atmospheric influences, a comprehensive understanding of their cooling potential was established. The study compared various materials, including RC material structures, conventional construction and roofing materials such as white cement paste, road asphalt, concrete, roofing shingles, ceramic roofing tiles, and PVC roofing material. These comparisons highlighted the superior performance of RC materials in terms of both net cooling power and radiative

forcing. The research also emphasized the significance of RF, which measures the impact of these materials on the Earth's energy balance. By quantifying the difference between incoming solar radiation and the thermal energy emitted back to space, the analysis provided insights into how the investigated materials can exacerbate or mitigate the warming effects of climate change. Notably, it was estimated that if just 1% of the Earth's surface were covered with these innovative RC materials, the resultant RF and GWP could significantly contribute to global warming mitigation efforts. The findings underscore the potential of RC technologies in reducing global warming potential and enhancing sustainability in building materials, making them a promising avenue for future research and practical applications in climate change mitigation.

**Results (Environmental Impact and GWP Reduction)**: RC technologies effectively reduce GWP through increased radiative heat flow to outer space and reduced cooling loads, leading to lower $CO_2$ emissions from electricity generation. Notably, RC materials with an optical solar reflectance of 98.25% and long-wavelength infrared emissivity of 98.5% achieved a net cooling power of 160.8 $W \cdot m^{-2}$ and a GWP of -252 $kgCO2\text{-}eq \cdot m^{-2}$ over 20 years, demonstrating their effectiveness. Additionally, the RF value for this sample was -1.01 $W \cdot m^{-2}$ when covering 1% of the Earth's surface. In contrast, roofing shingles showed a net cooling power of -12.3 $W \cdot m^{-2}$ with a GWP of 19.3 $kgCO2\text{-}eq \cdot m^{-2}$, highlighting their less favorable environmental impact. The results suggest that covering just 1% of the Earth's surface with effective RC materials could significantly offset anthropogenic $CO_2$ emissions, reinforcing the potential of RC technologies in climate mitigation strategies.

2. **To perform numerical simulations to investigate the effects of placing reflective surfaces under a RC material structure:** The study intended to model and simulate different structural configurations and underside surfaces, such as parabolic reflectors, to enhance the cooling efficiency of RC systems by cooling them from their bottom side as well as their top side.

**Methods (Placing reflective materials with different configurations beneath RC material structures)**: Detailed Monte Carlo ray-tracing (MCRT) methods were developed to simulate the cooling performance of RC material structures in various configurations. These simulations enabled the assessment of different geometric designs, including flat and parabolic reflectors, by calculating the net cooling power and determining the temperature reductions achievable through RC systems. This study employs a three-dimensional numerical analysis to explore the impact of an underside reflector on the cooling effectiveness of RC systems. Six distinct configurations are examined, each designed to assess how varying reflective surfaces influence the cooling performance of a point source RC:

i. **Case 1 (Blackbody)**: The first configuration featured a flat surface with infinite width and blackbody properties positioned beneath the RC. This served as the reference case for comparison.
ii. **Case 2 (Infinite Flat Reflector)**: In this setup, the RC was situated above an infinite flat reflective surface, allowing for enhanced reflection of emitted radiation.
iii. **Case 3 (1 m Flat Reflector)**: A flat circular reflector, 1 meter in width, was placed 0.1 meters below the RC material structure. This design enabled a focused reflection of emitted thermal energy.
iv. **Cases 4, 5, and 6 (Parabolic Reflectors)**: These cases utilized parabolic reflective dishes to enhance cooling performance further. The RC was positioned at the focal point of the dishes, with varying focal lengths and heights specified for each case: **Case 4**: Focal length of 0.1 m and height of 0.1 m. **Case 5**: Focal length of 0.1 m with a greater height of 0.625 m. **Case 6**: Focal length of 0.016 m with a height of 0.625 m.

In all configurations, the reflective surfaces were treated as perfectly specular reflectors, maximizing the efficiency of thermal radiation reflection. Two different emittance spectra were analyzed to determine the radiation emitted from the RC material structure and the radiation received from the atmosphere. The first spectrum represented an ideal top-hat selective radiator, which exhibits high emittance (100%) within the atmospheric window

(8 to 13 μm) and zero emittance outside this range. The second spectrum corresponded to an ideal step-function broadband radiator, having zero emittance for wavelengths less than 4 μm and full emittance (100%) for longer wavelengths. The cooling performance of the RC systems was assessed by analyzing how effectively they can dissipate thermal energy to the surroundings. The analysis considered factors such as the RC's temperature, atmospheric conditions, and the nature of the reflective surfaces.

**Results (Cooling Performance of Underside Configurations for RC Technology)**: Numerical simulations comparing different RC configurations demonstrated the superior cooling performance of parabolic geometries. Parabolic reflectors (Cases 4, 5, and 6) achieved the lowest temperatures under ideal conditions when ambient temperature is 300 K, outperforming flat reflectors and blackbody configurations. The results indicate that when assuming an ideal selective emittance spectrum without solar absorption and convective heat transfer at an ambient temperature of 300 K, the steady-state temperatures for Cases 4, 5, and 6 were roughly 237 K, 230 K, and 229 K, respectively. These configurations present a promising option for integration into various cooling systems, such as air conditioning, water harvesting, and $CO_2$ capture.

3. **To design and experimentally investigate a porous Passive Daytime Radiative Cooler (PDRC) system with an optimized and controlled pore size distribution of micro and nano sizes using a phase inversion fabrication technique to demonstrate high solar reflectivity as well as high emissivity in Long Wavelength Infrared (LWIR) wavelengths**: Through a phase inversion fabrication technique, the goal was to engineer porous PVDF-HFP RC materials with enhanced optical properties and RC performance.

**Methods (Fabrication of enhanced porous RC materials)**: This study employed PVDF-HFP as the primary polymer. Phase inversion was utilized to create hybrid micro- and nano-cellular material structures within the PVDF-HFP film for RC applications. Precursor solutions were prepared using varying mass ratios of PVDF-HFP, acetone, and water.

Different volumes of the polymer solution were poured onto the substrate to create samples of varying thicknesses for further investigation. Sample compositions and identifications are detailed in the study's tables. The phase morphology of the porous PVDF-HFP films was analyzed through cryo-fracturing and scanning electron microscopy (SEM). The optical performance of the RC materials was evaluated using a UV-Vis-NIR spectrophotometer, covering wavelengths from 0.3 to 2.5 μm. The mid-infrared optical behavior was examined with Fourier transform infrared (FTIR) spectroscopy. The emissive properties of the materials were measured using the EM-4 Emissometer at approximately 390 K, allowing for the calculation of total hemispheric emissivity. The study aims to understand the thermal energy exchange of a RC material structure exposed to the sky. It evaluates the cooling performance by analyzing factors such as the radiated heat to outer space, solar irradiance, atmospheric thermal radiation, and convective heat transfer from the surrounding environment. To achieve effective passive daytime RC, the materials must minimize solar heat gain while maximizing thermal energy radiation to the cold sky. This necessitates high solar reflectance and significant long-wave infrared emissivity in the RC surface. The overall goal is to optimize the RC performance for practical applications.

**Results (Fabrication of Enhanced Porous PVDF-HFP samples as RC Materials)**: This study aimed on optimizing porous PVDF-HFP films for RC by tailoring pore structures through adjustments in water, polymer concentrations, and film thickness. Varying the water-to-acetone and polymer-to-acetone ratios revealed a significant influence on pore size, distribution, and optical properties, particularly solar reflectance. The sample (1-8-1.25), with a polymer-to-acetone ratio of 1 and water-to-acetone ratio of 1.25, achieved a high solar reflectance of 98.2% and LWIR emittance of 98.5%, resulting in a net cooling power of 86 $W \cdot m^{-2}$ under 1000 $W \cdot m^{-2}$ solar irradiance. These findings highlight the effectiveness of hierarchical porous films in RC applications.

4. **To demonstrate a proof-of-concept of the developed PDRC** material **structure in a practical application and to evaluate its performance in an outdoor setup:** To provide practical validation for the developed PDRC material structure, this objective involved the

design and implementation of an outdoor experimental setup. The setup was specifically tailored to assess the performance of PDRC materials in real-world conditions.

**Methods (Outdoor RC Performance Measurements and Dew Condensation Experimental Setup Dew Condensation Experiments):** The outdoor experimental setup to measure the RC performance of the samples consisted of eight distinct configurations designed to evaluate the performance of the RC samples and underside surfaces under controlled conditions. The configurations include:

I. Parabolic Reflector Embedding RC: A 2 cm diameter RC disk is positioned at the focal point of a mirrored parabolic dish, maximizing its exposure to direct radiative heat transfer.
II. Parabolic Reflector Embedding Blackbody: A 2 cm diameter blackbody disk is similarly placed at the focal point of a parabolic dish, allowing direct comparison of cooling effects between the RC and an ideal blackbody.
III. Parabolic Blackbody Embedding RC: The RC sample is positioned at the focal point of a blackbody-coated paraboloid, enabling analysis of how the blackbody influences the heat absorption and emission of the RC in contrast to a reflective paraboloid setup.
IV. Flat Reflector Embedding RC: A 2 cm diameter disk, is mounted on a needle and placed in the middle of a flat square reflector with a side length of 5 cm. This setup simulates an infinite flat reflective surface beneath the RC sample to enhance RC.
V. Flat Blackbody Embedding RC: The RC sample is similarly placed on a needle at the center of a square surface covered with blackbody material. This configuration allows for evaluation of the RC's cooling performance on a blackbody-coated surface compared to a reflective surface, highlighting differences in heat transfer behavior.

Measurement tools included thermocouples for temperature monitoring, an anemometer for relative humidity and wind speed, and a pyranometer for solar irradiance measurement, with the entire apparatus positioned on a rooftop to simulate real-world conditions. Data loggers were also used to capture the data over a period.

Another experimental setup aimed to replicate and analyze the dew collection process under controlled indoor conditions, overcoming the limitations associated with outdoor experiments, such as weather variability and high costs. The test was done using the device designed by the LIED group at Université Paris Cité. The Dew Condensation Experimental Setup consisted of several key components designed to facilitate controlled dew formation through RC. The **climate-controlled chamber** maintained stable temperature and high humidity (30˚C and 90%, respectively) to replicate ideal conditions for dew collection. A **cold source** made from solid carbon dioxide (dry ice) served to provide a constant low temperature, promoting effective RC. The **dew collector** holds the RC samples, while the **sample holder** secures them for optimal heat exchange. The cold source (dry ice) was placed beneath the chamber, enabling effective RC, while data collection was facilitated through a balance for measuring condensed water, thermocouples for temperature monitoring, and an IR camera for visual documentation of the dew formation process, ultimately allowing for an analysis of the RC materials' effectiveness in dew collection.

**Results (Outdoor RC Performance Measurements and Dew Condensation Experimental Setup Dew Condensation Experiments):** The experimental results reveal that from approximately 17:00 to 07:00, the Parabolic Reflector Embedding RC configuration (I: light blue line) achieved the lowest absolute temperature of 5 °C, showcasing effective cooling throughout the night. However, the temperature differential (ΔT) relative to the ambient air was -3.5 °C, indicating significant cooling effects but less pronounced relative performance. As sunlight returned from 07:00 to 12:00, the Parabolic Reflector Embedding Blackbody (II: yellow line) exhibited the steepest temperature increase due to its high absorption capacity, while the Parabolic Reflector Embedding RC (I) showed a slower rise with a maximum ΔT of -10 °C, highlighting its ability to mitigate solar heating. Notably, from 13:00 to 16:00, the Flat Reflector Embedding RC (IV: dark blue line) outperformed the Parabolic Reflector configuration, achieving a maximum ΔT

of -9 °C compared to -8.5 °C due to its effective reflection of solar radiation. Overall, these findings emphasize the effectiveness of the Parabolic Reflector Embedding RC and the Flat Reflector's superior performance, underscoring the importance of design choices in optimizing RC applications under varying environmental conditions.

Dew condensation experiments conducted at 30 ˚C and 90% relative humidity demonstrated the effectiveness of the sample (1-8-1.25) with 850 μm thickness, which achieved a steady-state condensation rate of $4 \times 10^{-5}$ $g \cdot s^{-1}$. The thermal profiles showed significant cooling, with temperatures dropping below ambient due to efficient radiative heat exchange. The cooling flux started at -100 $W \cdot m^{-2}$ and stabilized at -60 $W \cdot m^{-2}$, highlighting the sample's sustained cooling performance and moisture capture efficiency under the given conditions.

Overall, this thesis has demonstrated the viability of RC technologies as both a passive cooling solution and a climate change mitigation tool. By addressing critical challenges related to cooling efficiency, material performance, and environmental impact, this research has established RC materials and configurations as viable options for widespread adoption in sustainable building practices and environmental applications.

## 7.2. Future work

While this thesis has made significant strides in understanding the performance and environmental benefits of RC materials, several areas require further investigation to optimize these technologies for broader application:

1. **Large-Scale Deployment and Economic Feasibility**: Although the environmental benefits of RC materials are well-established, future work should address the economic feasibility of large-scale deployment. This includes analyzing the costs of production,

installation, and long-term maintenance, as well as assessing potential barriers to adoption in both developed and developing regions.

2. **Hybrid RC and Renewable Energy Systems**: The integration of RC technologies with renewable energy systems—such as solar photovoltaics—presents a compelling avenue for future research. Hybrid systems could provide both cooling and electricity generation, maximizing energy efficiency and reducing reliance on traditional cooling and energy generation systems.

3. **Durability and Environmental Impact over Time**: The long-term performance and durability of RC materials, especially in harsh or extreme environmental conditions, requires further investigation. Research should also explore the environmental impact of potential material degradation, disposal, or recycling, ensuring that RC technologies remain sustainable throughout their lifecycle.

4. **Innovative Applications Beyond Building Cooling**: While much of this research has focused on building cooling, future work should explore additional applications of RC technologies, such as in water harvesting, greenhouse cooling, or carbon capture. The parabolic reflector configurations, in particular, have shown promise in enhancing condensation for water collection and could be adapted for a range of industrial and agricultural uses.

5. **Policy and Standards Development**: For RC technologies to be widely adopted, there is a need for the development of international standards and policies governing their implementation. Future research could work towards establishing guidelines for RC material performance, integration in urban planning, and financial incentives for adoption.

In conclusion, this thesis has laid the foundation for the widespread adoption of RC technologies as an integral part of sustainable building practices and climate change mitigation strategies. By addressing the outlined challenges and pursuing innovative research directions, RC technologies have the potential to significantly contribute to the global effort to reduce greenhouse gas emissions, manage energy consumption, and restore balance to the Earth's climate system.

# References


[1] M. M. Hossain and M. Gu, "Radiative cooling: Principles, progress, and potentials," *Adv. Sci.*, vol. 3, no. 7, pp. 1–10, 2016, doi: 10.1002/advs.201500360.

[2] B. Zhao, M. Hu, X. Ao, N. Chen, and G. Pei, "Radiative cooling: A review of fundamentals, materials, applications, and prospects," *Appl. Energy*, vol. 236, no. August 2018, pp. 489–513, 2019, doi: 10.1016/j.apenergy.2018.12.018.

[3] G. Heidarinejad, M. Farmahini Farahani, and S. Delfani, "Investigation of a hybrid system of nocturnal radiative cooling and direct evaporative cooling," *Build. Environ.*, vol. 45, no. 6, pp. 1521–1528, 2010, doi: 10.1016/j.buildenv.2010.01.003.

[4] A. P. Raman, M. A. Anoma, L. Zhu, E. Rephaeli, and S. Fan, "Passive radiative cooling below ambient air temperature under direct sunlight," *Nature*, vol. 515, no. 7528, pp. 540–544, 2014, doi: 10.1038/nature13883.

[5] W. Wang, N. Fernandez, S. Katipamula, and K. Alvine, "Performance assessment of a photonic radiative cooling system for office buildings," *Renew. Energy*, vol. 118, pp. 265–277, 2018, doi: 10.1016/j.renene.2017.10.062.

[6] K. Zhang, D. Zhao, X. Yin, R. Yang, and G. Tan, "Energy saving and economic analysis of a new hybrid radiative cooling system for single-family houses in the USA," *Appl. Energy*, vol. 224, no. March, pp. 371–381, 2018, doi: 10.1016/j.apenergy.2018.04.115.

[7] M. Santamouris, A. Synnefa, and T. Karlessi, "Using advanced cool materials in the urban built environment to mitigate heat islands and improve thermal comfort conditions," *Sol. Energy*, vol. 85, no. 12, pp. 3085–3102, Dec. 2011, doi: 10.1016/J.SOLENER.2010.12.023.

[8] V. Costanzo, G. Evola, and L. Marletta, "Cool roofs for passive cooling: performance in different climates and for different insulation levels in Italy," *Adv. Build. Energy Res.*, vol. 7, no. 2, pp. 155–169, 2013, doi: 10.1080/17512549.2013.865556.

[9] B. Ko, D. Lee, T. Badloe, and J. Rho, "Metamaterial-based radiative cooling: Towards energy-free all-day cooling," *Energies*, vol. 12, no. 1, pp. 1–14, 2019, doi: 10.3390/en12010089.

[10] L. Pérez-Lombard, J. Ortiz, and C. Pout, "A review on buildings energy consumption information," *Energy Build.*, vol. 40, no. 3, pp. 394–398, 2008, doi: 10.1016/j.enbuild.2007.03.007.

[11] L. Chen, K. Zhang, M. Ma, S. Tang, F. Li, and X. Niu, "Sub-ambient radiative cooling and its application in buildings," *Build. Simul.*, vol. 13, no. 6, pp. 1165–1189, 2020, doi: 10.1007/s12273-020-0646-x.

[12] H. Fang *et al.*, "Performance evaluation of a metamaterial-based new cool roof using improved Roof Thermal Transfer Value model," *Appl. Energy*, vol. 248, no. April, pp. 589–599, 2019, doi: 10.1016/j.apenergy.2019.04.116.

[13] B. Zhao, M. Hu, X. Ao, and G. Pei, "Conceptual development of a building-integrated photovoltaic–radiative cooling system and preliminary performance analysis in Eastern China," *Appl. Energy*, vol. 205, no. August, pp. 626–634, 2017, doi: 10.1016/j.apenergy.2017.08.011.

[14] J. Chen, L. Lu, Q. Gong, W. Y. Lau, and K. H. Cheung, "Techno-economic and environmental performance assessment of radiative sky cooling-based super-cool roof applications in China," *Energy Convers. Manag.*, vol. 245, p. 114621, 2021, doi: 10.1016/j.enconman.2021.114621.

[15] T. L. Bergman, "Active daytime radiative cooling using spectrally selective surfaces for air conditioning and refrigeration systems," *Sol. Energy*, vol. 174, no. January, pp. 16–23, 2018, doi: 10.1016/j.solener.2018.08.070.

[16] A. Castaldo, G. Vitiello, E. Gambale, M. Lanchi, M. Ferrara, and M. Zinzi, "Mirroring solar radiation

emitting heat toward the universe: design, production, and preliminary testing of a metamaterial based daytime passive radiative cooler," *Energies*, vol. 13, no. 6, pp. 1–16, 2020, doi: 10.3390/en13164192.

[17] X. Yin, R. Yang, G. Tan, and S. Fan, "Terrestrial radiative cooling: Using the cold universe as a renewable and sustainable energy source," *Science (80-. ).*, vol. 370, no. 6518, pp. 786–791, 2020, doi: 10.1126/science.abb0971.

[18] X. Lu, P. Xu, H. Wang, T. Yang, and J. Hou, "Cooling potential and applications prospects of passive radiative cooling in buildings: The current state-of-the-art," *Renew. Sustain. Energy Rev.*, vol. 65, no. 4800, pp. 1079–1097, 2016, doi: 10.1016/j.rser.2016.07.058.

[19] J. Liu, Z. Zhou, J. Zhang, W. Feng, and J. Zuo, "Advances and challenges in commercializing radiative cooling," *Mater. Today Phys.*, vol. 11, p. 100161, 2019, doi: 10.1016/j.mtphys.2019.100161.

[20] R. Family and M. P. Mengüç, "Materials for Radiative Cooling: A Review," *Procedia Environ. Sci.*, vol. 38, pp. 752–759, 2017, doi: 10.1016/j.proenv.2017.03.158.

[21] S. Catalanotti, V. Cuomo, G. Piro, D. Ruggi, V. Silvestrini, and G. Troise, "The radiative cooling of selective surfaces," *Sol. Energy*, vol. 17, no. 2, pp. 83–89, 1975, doi: 10.1016/0038-092X(75)90062-6.

[22] M. Zeyghami, D. Y. Goswami, and E. Stefanakos, "A review of clear sky radiative cooling developments and applications in renewable power systems and passive building cooling," *Sol. Energy Mater. Sol. Cells*, vol. 178, no. December 2017, pp. 115–128, 2018, doi: 10.1016/j.solmat.2018.01.015.

[23] W. Li, Y. Li, and K. W. Shah, "A materials perspective on radiative cooling structures for buildings," *Sol. Energy*, vol. 207, no. April, pp. 247–269, 2020, doi: 10.1016/j.solener.2020.06.095.

[24] B. Bhatia *et al.*, "Passive directional sub-ambient daytime radiative cooling," *Nat. Commun.*, vol. 9, no. 1, pp. 1–8, 2018, doi: 10.1038/s41467-018-07293-9.

[25] X. Li, J. Peoples, Z. Huang, Z. Zhao, J. Qiu, and X. Ruan, "Full Daytime Sub-ambient Radiative Cooling in Commercial-like Paints with High Figure of Merit," *Cell Reports Phys. Sci.*, vol. 1, no. 10, p. 100221, 2020, doi: 10.1016/j.xcrp.2020.100221.

[26] S. Atiganyanun *et al.*, "Effective Radiative Cooling by Paint-Format Microsphere-Based Photonic Random Media," *ACS Photonics*, vol. 5, no. 4, pp. 1181–1187, 2018, doi: 10.1021/acsphotonics.7b01492.

[27] A. Kafaei *et al.*, "Transient Computational Fluid Dynamics Analysis of Passive Cooling in a Building with Diurnal Radiative Cooling Material Coated onto Its Rooftop," *Energy Technol.*, vol. 12, no. 2, pp. 1–9, 2024, doi: 10.1002/ente.202300888.

[28] A. Pirvaram, N. Talebzadeh, S. N. Leung, and P. G. O'Brien, "Radiative cooling for buildings: A review of techno-enviro-economics and life-cycle assessment methods," *Renew. Sustain. Energy Rev.*, vol. 162, no. October 2021, p. 112415, 2022, doi: 10.1016/j.rser.2022.112415.

[29] S. Jeon and J. Shin, "Ideal spectral emissivity for radiative cooling of earthbound objects," *Sci. Rep.*, vol. 10, no. 1, pp. 1–7, 2020, doi: 10.1038/s41598-020-70105-y.

[30] J. Chen and L. Lu, "Development of radiative cooling and its integration with buildings: A comprehensive review," *Sol. Energy*, vol. 212, no. October, pp. 125–151, 2020, doi: 10.1016/j.solener.2020.10.013.

[31] Suhendri, M. Hu, Y. Su, J. Darkwa, and S. Riffat, "Implementation of passive radiative cooling technology in buildings: A review," *Buildings*, vol. 10, no. 12, pp. 1–28, 2020, doi: 10.3390/buildings10120215.

[32] S. Vall and A. Castell, "Radiative cooling as low-grade energy source: A literature review," *Renew. Sustain. Energy Rev.*, vol. 77, no. August 2016, pp. 803–820, 2017, doi: 10.1016/j.rser.2017.04.010.

[33] J. P. Bijarniya, J. Sarkar, and P. Maiti, "Review on passive daytime radiative cooling: Fundamentals, recent researches, challenges and opportunities," *Renew. Sustain. Energy Rev.*, vol. 133, no. August, p. 110263, 2020, doi: 10.1016/j.rser.2020.110263.

[34] M. Santamouris and J. Feng, “Recent progress in daytime radiative cooling: Is it the air conditioner of the future?,” *Buildings*, vol. 8, no. 12, 2018, doi: 10.3390/buildings8120168.

[35] W. Li and S. Fan, “Harvesting the Coldness,” *Opt. Photonics News*, no. November, pp. 32–39, 2019.

[36] K. W. Lee *et al.*, “Visibly Clear Radiative Cooling Metamaterials for Enhanced Thermal Management in Solar Cells and Windows,” *Adv. Funct. Mater.*, vol. 32, no. 1, pp. 1–10, 2022, doi: 10.1002/adfm.202105882.

[37] M. Medrano, “Optimal Characteristics of an Adaptive Windshield for a Solar Collector and Radiative Cooling Combined System,” pp. 1–8, 2021, doi: 10.18086/eurosun.2020.06.04.

[38] Z. Chen, L. Zhu, A. Raman, and S. Fan, “Radiative cooling to deep sub-freezing temperatures through a 24-h day-night cycle,” *Nat. Commun.*, vol. 7, pp. 1–5, 2016, doi: 10.1038/ncomms13729.

[39] A. Leroy *et al.*, “MATERIALS SCIENCE High-performance subambient radiative cooling enabled by optically selective and thermally insulating polyethylene aerogel,” *Sci. Adv.*, vol. 5, no. 10, pp. 1–8, 2019, doi: 10.1126/sciadv.aat9480.

[40] S. N. Bathgate and S. G. Bosi, “A robust convection cover material for selective radiative cooling applications,” *Sol. Energy Mater. Sol. Cells*, vol. 95, no. 10, pp. 2778–2785, 2011, doi: 10.1016/j.solmat.2011.05.027.

[41] J. Liu *et al.*, “Sub-ambient radiative cooling with wind cover,” *Renew. Sustain. Energy Rev.*, vol. 130, no. May, p. 109935, 2020, doi: 10.1016/j.rser.2020.109935.

[42] X. Sun, Y. Sun, Z. Zhou, M. A. Alam, and P. Bermel, “Radiative sky cooling: Fundamental physics, materials, structures, and applications,” *Nanophotonics*, vol. 6, no. 5, pp. 997–1015, 2017, doi: 10.1515/nanoph-2017-0020.

[43] M. Hu *et al.*, “An analytical study of the nocturnal radiative cooling potential of typical photovoltaic/thermal module,” *Appl. Energy*, vol. 277, no. April, p. 115625, 2020, doi: 10.1016/j.apenergy.2020.115625.

[44] S. Zhang and J. Niu, “Cooling performance of nocturnal radiative cooling combined with microencapsulated phase change material (MPCM) slurry storage,” *Energy Build.*, vol. 54, pp. 122–130, 2012, doi: 10.1016/j.enbuild.2012.07.041.

[45] B. Zhao, M. Hu, X. Ao, X. Huang, X. Ren, and G. Pei, “Conventional photovoltaic panel for nocturnal radiative cooling and preliminary performance analysis,” *Energy*, vol. 175, pp. 677–686, 2019, doi: 10.1016/j.energy.2019.03.106.

[46] M. Hu, G. Pei, Q. Wang, J. Li, Y. Wang, and J. Ji, “Field test and preliminary analysis of a combined diurnal solar heating and nocturnal radiative cooling system,” *Appl. Energy*, vol. 179, pp. 899–908, Oct. 2016, doi: 10.1016/J.APENERGY.2016.07.066.

[47] D. Shen, C. Yu, and W. Wang, “Investigation on the thermal performance of the novel phase change materials wall with radiative cooling,” *Appl. Therm. Eng.*, vol. 176, no. May, p. 115479, 2020, doi: 10.1016/j.applthermaleng.2020.115479.

[48] M. Farmahini Farahani, G. Heidarinejad, and S. Delfani, “A two-stage system of nocturnal radiative and indirect evaporative cooling for conditions in Tehran,” *Energy Build.*, vol. 42, no. 11, pp. 2131–2138, 2010, doi: 10.1016/j.enbuild.2010.07.003.

[49] C. G. Granqvist and A. Hjortsberg, “Radiative cooling to low temperatures: General considerations and application to selectively emitting SiO films,” *J. Appl. Phys.*, vol. 52, no. 6, pp. 4205–4220, 1981, doi: 10.1063/1.329270.

[50] J. Mandal *et al.*, “Hierarchically porous polymer coatings for highly efficient passive daytime radiative cooling,” *Science (80-. ).*, vol. 362, no. 6412, pp. 315–319, 2018, doi: 10.1126/science.aat9513.

[51] H. Zhang and D. Fan, “Improving Heat Dissipation and Temperature Uniformity in Radiative Cooling

Coating," *Energy Technol.*, vol. 8, no. 5, pp. 1–7, 2020, doi: 10.1002/ente.201901362.

[52] T. Wang, Y. Wu, L. Shi, X. Hu, M. Chen, and L. Wu, "A structural polymer for highly efficient all-day passive radiative cooling," *Nat. Commun.*, vol. 12, no. 1, pp. 1–11, 2021, doi: 10.1038/s41467-020-20646-7.

[53] S. Y. Jeong, C. Y. Tso, Y. M. Wong, C. Y. H. Chao, and B. Huang, "Daytime passive radiative cooling by ultra emissive bio-inspired polymeric surface," *Sol. Energy Mater. Sol. Cells*, vol. 206, no. July 2019, p. 110296, 2020, doi: 10.1016/j.solmat.2019.110296.

[54] Y. Zhang *et al.*, "Effective radiative cooling with ZrO2/PDMS reflective coating," *Sol. Energy Mater. Sol. Cells*, vol. 229, no. May, p. 111129, 2021, doi: 10.1016/j.solmat.2021.111129.

[55] Y. Weng, W. Zhang, Y. Jiang, W. Zhao, and Y. Deng, "Effective daytime radiative cooling via a template method based PDMS sponge emitter with synergistic thermo-optical activity," *Sol. Energy Mater. Sol. Cells*, vol. 230, no. May, p. 111205, 2021, doi: 10.1016/j.solmat.2021.111205.

[56] E. Lee and T. Luo, "Black body-like radiative cooling for flexible thin-film solar cells," *Sol. Energy Mater. Sol. Cells*, vol. 194, no. August 2018, pp. 222–228, 2019, doi: 10.1016/j.solmat.2019.02.015.

[57] L. Zhou *et al.*, "A polydimethylsiloxane-coated metal structure for all-day radiative cooling," *Nat. Sustain.*, vol. 2, no. 8, pp. 718–724, 2019, doi: 10.1038/s41893-019-0348-5.

[58] S. Son *et al.*, "Colored emitters with silica-embedded perovskite nanocrystals for efficient daytime radiative cooling," *Nano Energy*, vol. 79, no. October 2020, p. 105461, 2021, doi: 10.1016/j.nanoen.2020.105461.

[59] M. Hu, G. Pei, Q. Wang, J. Li, Y. Wang, and J. Ji, "Field test and preliminary analysis of a combined diurnal solar heating and nocturnal radiative cooling system," *Appl. Energy*, vol. 179, pp. 899–908, 2016, doi: 10.1016/j.apenergy.2016.07.066.

[60] B. Orel, M. K. Gunde, and A. Krainer, "Radiative cooling efficiency of white pigmented paints," *Sol. Energy*, vol. 50, no. 6, pp. 477–482, 1993, doi: 10.1016/0038-092X(93)90108-Z.

[61] A. Andretta and B. Bartoli, "Resume . - L ' espace extra-atmospherique fonctionne en pratique comme un absorbeur de radiation et il peut Otre utilise ainsi qu ' une sour- ce non conventionnelle d ' energie . Les surfaces ayant une 6missivit6 qui s ' accorde avec la fenstre at- froid ," 1981.

[62] T. M. J. Nilsson, G. A. Niklasson, and C. G. Granqvist, "A solar reflecting material for radiative cooling applications: ZnS pigmented polyethylene," *Sol. Energy Mater. Sol. Cells*, vol. 28, no. 2, pp. 175–193, 1992, doi: 10.1016/0927-0248(92)90010-M.

[63] D. Chae, S. Son, H. Lim, P. H. Jung, J. Ha, and H. Lee, "Scalable and paint-format microparticle–polymer composite enabling high-performance daytime radiative cooling," *Mater. Today Phys.*, vol. 18, 2021, doi: 10.1016/j.mtphys.2021.100389.

[64] D. Chae *et al.*, "Spectrally Selective Inorganic-Based Multilayer Emitter for Daytime Radiative Cooling," *ACS Appl. Mater. Interfaces*, vol. 12, no. 7, pp. 8073–8081, 2020, doi: 10.1021/acsami.9b16742.

[65] K. Yao *et al.*, "Near-Perfect Selective Photonic Crystal Emitter with Nanoscale Layers for Daytime Radiative Cooling," *ACS Appl. Nano Mater.*, vol. 2, no. 9, pp. 5512–5519, 2019, doi: 10.1021/acsanm.9b01097.

[66] H. Ma *et al.*, "Multilayered SiO2/Si3N4 photonic emitter to achieve high-performance all-day radiative cooling," *Sol. Energy Mater. Sol. Cells*, vol. 212, p. 110584, Aug. 2020, doi: 10.1016/J.SOLMAT.2020.110584.

[67] D. Hu and Y. Gu, "A membrane reflector, polymer hybrid infrared emitter for better radiative cooling performance," *Sol. Energy Mater. Sol. Cells*, vol. 234, no. June 2021, 2022, doi: 10.1016/j.solmat.2021.111417.

[68] M. M. Hossain, B. Jia, and M. Gu, "A Metamaterial Emitter for Highly Efficient Radiative Cooling," *Adv. Opt. Mater.*, vol. 3, no. 8, pp. 1047–1051, 2015, doi: 10.1002/adom.201500119.

[69] E. Rephaeli, A. Raman, and S. Fan, "Ultrabroadband photonic structures to achieve high-performance daytime radiative cooling," *Nano Lett.*, vol. 13, no. 4, pp. 1457–1461, 2013, doi: 10.1021/nl4004283.

[70] M. Gao *et al.*, "Approach to fabricating high-performance cooler with near-ideal emissive spectrum for above-ambient air temperature radiative cooling," *Sol. Energy Mater. Sol. Cells*, vol. 200, no. June, p. 110013, 2019, doi: 10.1016/j.solmat.2019.110013.

[71] D. Wu *et al.*, "The design of ultra-broadband selective near-perfect absorber based on photonic structures to achieve near-ideal daytime radiative cooling," *Mater. Des.*, vol. 139, pp. 104–111, 2018, doi: 10.1016/j.matdes.2017.10.077.

[72] L. Zhu, A. P. Raman, and S. Fan, "Radiative cooling of solar absorbers using a visibly transparent photonic crystal thermal blackbody," *Proc. Natl. Acad. Sci. U. S. A.*, vol. 112, no. 40, pp. 12282–12287, 2015, doi: 10.1073/pnas.1509453112.

[73] L. Zhu, A. Raman, and S. Fan, "Color-preserving daytime radiative cooling," *Appl. Phys. Lett.*, vol. 103, no. 22, 2013, doi: 10.1063/1.4835995.

[74] Y. Yang, S. Taylor, H. Alshehri, and L. Wang, "Wavelength-selective and diffuse infrared thermal emission mediated by magnetic polaritons from silicon carbide metasurfaces," *Appl. Phys. Lett.*, vol. 111, no. 5, 2017, doi: 10.1063/1.4996865.

[75] H. Zhang *et al.*, "Biologically inspired flexible photonic films for efficient passive radiative cooling," *Proc. Natl. Acad. Sci. U. S. A.*, vol. 117, no. 26, pp. 14657–14666, 2020, doi: 10.1073/pnas.2001802117.

[76] Y. Xu, Y. Xuan, and X. Liu, "Broadband selective tailoring of spectral features with multiple-scale and multi-material metasurfaces," *Opt. Commun.*, vol. 467, no. November 2019, p. 125691, 2020, doi: 10.1016/j.optcom.2020.125691.

[77] C. Zou *et al.*, "Metal-Loaded Dielectric Resonator Metasurfaces for Radiative Cooling," *Adv. Opt. Mater.*, vol. 5, no. 20, pp. 1–7, 2017, doi: 10.1002/adom.201700460.

[78] N. Lee *et al.*, "Multiple Resonance Metamaterial Emitter for Deception of Infrared Emission with Enhanced Energy Dissipation," *ACS Appl. Mater. Interfaces*, vol. 12, no. 7, pp. 8862–8869, 2020, doi: 10.1021/acsami.9b21030.

[79] K. Sun *et al.*, "VO2 Thermochromic Metamaterial-Based Smart Optical Solar Reflector," *ACS Photonics*, vol. 5, no. 6, pp. 2280–2286, 2018, doi: 10.1021/acsphotonics.8b00119.

[80] K. Sun *et al.*, "Metasurface Optical Solar Reflectors Using AZO Transparent Conducting Oxides for Radiative Cooling of Spacecraft," *ACS Photonics*, vol. 5, no. 2, pp. 495–501, 2018, doi: 10.1021/acsphotonics.7b00991.

[81] Y. Zhai *et al.*, "Scalable-manufactured randomized glass-polymer hybrid metamaterial for daytime radiative cooling," *Science (80-. ).*, vol. 355, no. 6329, pp. 1062–1066, 2017, doi: 10.1126/science.aai7899.

[82] A. Hervé, J. Drévillon, Y. Ezzahri, and K. Joulain, "Radiative cooling by tailoring surfaces with microstructures: Association of a grating and a multi-layer structure," *J. Quant. Spectrosc. Radiat. Transf.*, vol. 221, pp. 155–163, 2018, doi: 10.1016/j.jqsrt.2018.09.015.

[83] D. H. Kim, G. J. Lee, S. Y. Heo, I. S. Kang, and Y. M. Song, "Thermostat property of Janus emitter in enclosures," *Sol. Energy Mater. Sol. Cells*, vol. 230, p. 111173, 2021, doi: 10.1016/j.solmat.2021.111173.

[84] K. Zhou *et al.*, "Three-Dimensional Printable Nanoporous Polymer Matrix Composites for Daytime Radiative Cooling," *Nano Lett.*, vol. 21, no. 3, pp. 1493–1499, 2021, doi: 10.1021/acs.nanolett.0c04810.

[85] C. Feng *et al.*, "Bilayer porous polymer for efficient passive building cooling," *Nano Energy*, vol. 85, no. March, p. 105971, 2021, doi: 10.1016/j.nanoen.2021.105971.

[86] J. long Kou, Z. Jurado, Z. Chen, S. Fan, and A. J. Minnich, "Daytime Radiative Cooling Using Near-Black Infrared Emitters," *ACS Photonics*, vol. 4, no. 3, pp. 626–630, 2017, doi: 10.1021/acsphotonics.6b00991.

[87] D. Li *et al.*, “Scalable and hierarchically designed polymer film as a selective thermal emitter for high-performance all-day radiative cooling,” *Nat. Nanotechnol.*, vol. 16, no. 2, pp. 153–158, 2021, doi: 10.1038/s41565-020-00800-4.

[88] P. Yang, C. Chen, and Z. M. Zhang, “A dual-layer structure with record-high solar reflectance for daytime radiative cooling,” *Sol. Energy*, vol. 169, no. May, pp. 316–324, 2018, doi: 10.1016/j.solener.2018.04.031.

[89] X. Wang *et al.*, “Scalable Flexible Hybrid Membranes with Photonic Structures for Daytime Radiative Cooling,” *Adv. Funct. Mater.*, vol. 30, no. 5, pp. 1–9, 2020, doi: 10.1002/adfm.201907562.

[90] Y. Liu, S. Son, D. Chae, P. H. Jung, and H. Lee, “Acrylic membrane doped with Al2O3 nanoparticle resonators for zero-energy consuming radiative cooling,” *Sol. Energy Mater. Sol. Cells*, vol. 213, no. April, p. 110561, 2020, doi: 10.1016/j.solmat.2020.110561.

[91] D. Lee *et al.*, “Sub-ambient daytime radiative cooling by silica-coated porous anodic aluminum oxide,” *Nano Energy*, vol. 79, no. September 2020, 2021, doi: 10.1016/j.nanoen.2020.105426.

[92] Q. Zhai and Q. Zhu, “Radiative cooling film with self-cleaning function,” *Sol. Energy Mater. Sol. Cells*, vol. 228, no. March, p. 111117, 2021, doi: 10.1016/j.solmat.2021.111117.

[93] Y. Fu, J. Yang, Y. S. Su, W. Du, and Y. G. Ma, “Daytime passive radiative cooler using porous alumina,” *Sol. Energy Mater. Sol. Cells*, vol. 191, no. October 2018, pp. 50–54, 2019, doi: 10.1016/j.solmat.2018.10.027.

[94] J. Jaramillo-Fernandez *et al.*, “Highly-Scattering Cellulose-Based Films for Radiative Cooling,” *Adv. Sci.*, vol. 9, no. 8, pp. 1–8, 2022, doi: 10.1002/advs.202104758.

[95] R. Dong *et al.*, “A weather-resistant daytime radiative cooler based on fluorocarbon resin,” *Sol. Energy Mater. Sol. Cells*, vol. 235, no. November 2021, pp. 4–13, 2022, doi: 10.1016/j.solmat.2021.111486.

[96] Z. Yang *et al.*, “Bio-inspired structure using random, three-dimensional pores in the polymeric matrix for daytime radiative cooling,” *Sol. Energy Mater. Sol. Cells*, vol. 227, no. September 2020, p. 111101, 2021, doi: 10.1016/j.solmat.2021.111101.

[97] Y. Zhang, T. Wang, X. Mei, M. Chen, and L. Wu, “Ordered Porous Polymer Films for Highly Efficient Passive Daytime Radiative Cooling,” *ACS Photonics*, vol. 10, no. 9, pp. 3124–3132, 2023, doi: 10.1021/acsphotonics.3c00494.

[98] M. Ahmadi Bonakdar and D. Rodrigue, “Electrospinning: Processes, Structures, and Materials,” *Macromol*, vol. 4, no. 1, pp. 58–103, 2024, doi: 10.3390/macromol4010004.

[99] T. Han *et al.*, “Advances in radiative sky cooling based on the promising electrospinning,” *Renew. Sustain. Energy Rev.*, vol. 200, no. April, p. 114533, 2024, doi: 10.1016/j.rser.2024.114533.

[100] H. Zhong *et al.*, “Hierarchically Hollow Microfibers as a Scalable and Effective Thermal Insulating Cooler for Buildings,” *ACS Nano*, vol. 15, no. 6, pp. 10076–10083, 2021, doi: 10.1021/acsnano.1c01814.

[101] H. Kim, S. McSherry, B. Brown, and A. Lenert, “Selectively Enhancing Solar Scattering for Direct Radiative Cooling through Control of Polymer Nanofiber Morphology,” *ACS Appl. Mater. Interfaces*, vol. 12, no. 39, pp. 43553–43559, 2020, doi: 10.1021/acsami.0c09374.

[102] Y. Zhang and J. Yu, “Scalable and High-Performance Radiative Cooling Fabrics through an Electrospinning Method,” *ACS Appl. Mater. Interfaces*, vol. 14, no. 40, pp. 45707–45715, 2022, doi: 10.1021/acsami.2c13727.

[103] J. Martín-de León, V. Bernardo, and M. Á. Rodríguez-Pérez, “Nanocellular polymers: The challenge of creating cells in the nanoscale,” *Materials (Basel).*, vol. 12, no. 5, pp. 1–19, 2019, doi: 10.3390/MA12050797.

[104] L. J. M. Jacobs, M. F. Kemmere, and J. T. F. Keurentjes, “Sustainable polymer foaming using high pressure carbon dioxide: A review on fundamentals, processes and applications,” *Green Chem.*, vol. 10, no. 7, pp.

731–73, 2008, doi: 10.1039/b801895b.

[105] Y. Wang, Z. Liao, S. Mathieu, and X. Tu, “Jo ur n al Pr pr oo,” *J. Hazard. Mater.*, p. 123965, 2020, doi: 10.1016/j.nanoen.2024.109695.

[106] A. K. Hołda and I. F. J. Vankelecom, “Understanding and guiding the phase inversion process for synthesis of solvent resistant nanofiltration membranes,” *J. Appl. Polym. Sci.*, vol. 132, no. 27, pp. 1–17, 2015, doi: 10.1002/app.42130.

[107] G. R. Guillen, Y. Pan, M. Li, and E. M. V. Hoek, “Preparation and characterization of membranes formed by nonsolvent induced phase separation: A review,” *Ind. Eng. Chem. Res.*, vol. 50, no. 7, pp. 3798–3817, 2011, doi: 10.1021/ie101928r.

[108] S. L. Duraikkannu, R. Castro-Muñoz, and A. Figoli, “A review on phase-inversion technique-based polymer microsphere fabrication,” *Colloids Interface Sci. Commun.*, vol. 40, no. October 2020, 2021, doi: 10.1016/j.colcom.2020.100329.

[109] Y. Tang *et al.*, “A review on models and simulations of membrane formation via phase inversion processes,” *J. Memb. Sci.*, vol. 640, no. August, p. 119810, 2021, doi: 10.1016/j.memsci.2021.119810.

[110] J. M. Maffi, G. R. Meira, and D. A. Estenoz, “Mechanisms and conditions that affect phase inversion processes: A review,” *Can. J. Chem. Eng.*, vol. 99, no. 1, pp. 178–208, 2021, doi: 10.1002/cjce.23853.

[111] B. Zhao, M. Hu, Q. Xuan, T. H. Kwan, Y. N. Dabwan, and G. Pei, “Tunable thermal management based on solar heating and radiative cooling,” *Sol. Energy Mater. Sol. Cells*, vol. 235, no. October 2021, p. 111457, 2022, doi: 10.1016/j.solmat.2021.111457.

[112] J. Prakash Bijarniya, J. Sarkar, and P. Maiti, “Performance improvement of CO2 air conditioner by integrating photonic radiative cooler as sub-cooler or/and roof envelope,” *Energy Convers. Manag.*, vol. 251, no. November 2021, p. 115019, 2022, doi: 10.1016/j.enconman.2021.115019.

[113] S. Y. Jeong, C. Y. Tso, M. Zouagui, Y. M. Wong, and C. Y. H. Chao, “A numerical study of daytime passive radiative coolers for space cooling in buildings,” *Build. Simul.*, vol. 11, no. 5, pp. 1011–1028, 2018, doi: 10.1007/s12273-018-0474-4.

[114] A. Baniassadi, D. J. Sailor, and G. A. Ban-Weiss, “Potential energy and climate benefits of super-cool materials as a rooftop strategy,” *Urban Clim.*, vol. 29, no. June, p. 100495, 2019, doi: 10.1016/j.uclim.2019.100495.

[115] Z. Zhang, S. Tong, and H. Yu, “Life Cycle Analysis of Cool Roof in Tropical Areas,” *Procedia Eng.*, vol. 169, pp. 392–399, 2016, doi: 10.1016/j.proeng.2016.10.048.

[116] C. Romeo and M. Zinzi, “Impact of a cool roof application on the energy and comfort performance in an existing non-residential building. A Sicilian case study,” *Energy Build.*, vol. 67, pp. 647–657, 2013, doi: 10.1016/j.enbuild.2011.07.023.

[117] D. Kolokotsa, M. Santamouris, and S. C. Zerefos, “Green and cool roofs’ urban heat island mitigation potential in European climates for office buildings under free floating conditions,” *Sol. Energy*, vol. 95, pp. 118–130, 2013, doi: 10.1016/j.solener.2013.06.001.

[118] H. Takebayashi, M. Moriyama, and T. Sugihara, “Study on the cool roof effect of Japanese traditional tiled roof: Numerical analysis of solar reflectance of unevenness tiled surface and heat budget of typical tiled roof system,” *Energy Build.*, vol. 55, pp. 77–84, 2012, doi: 10.1016/j.enbuild.2011.09.023.

[119] T. Xu, J. Sathaye, H. Akbari, V. Garg, and S. Tetali, “Quantifying the direct benefits of cool roofs in an urban setting: Reduced cooling energy use and lowered greenhouse gas emissions,” *Build. Environ.*, vol. 48, no. 1, pp. 1–6, 2012, doi: 10.1016/j.buildenv.2011.08.011.

[120] E. Bozonnet, M. Doya, and F. Allard, “Cool roofs impact on building thermal response: A French case study,” *Energy Build.*, vol. 43, no. 11, pp. 3006–3012, 2011, doi: 10.1016/j.enbuild.2011.07.017.

[121] X. Yu, J. Chan, and C. Chen, “Review of radiative cooling materials: Performance evaluation and design approaches,” *Nano Energy*, vol. 88, no. January, p. 106259, 2021, doi: 10.1016/j.nanoen.2021.106259.

[122] International Energy Agency (IEA), “The Future of Cooling Opportunities for energy- efficient air conditioning <https://iea.blob.core.windows.net/assets/0bb45525-277f-4c9c-8d0c-9c0cb5e7d525/The_Future_of_Cooling.pdf>,” p. 92, 2018, [Online]. Available: https://iea.blob.core.windows.net/assets/0bb45525-277f-4c9c-8d0c-9c0cb5e7d525/The_Future_of_Cooling.pdf

[123] L. Pérez-Lombard, J. Ortiz, and C. Pout, “A review on buildings energy consumption information,” *Energy Build.*, vol. 40, no. 3, pp. 394–398, Jan. 2008, doi: 10.1016/J.ENBUILD.2007.03.007.

[124] K. Z. (Canada) Myles Allen (UK), Mustafa Babiker (Sudan), Yang Chen (China), Heleen de Coninck (Netherlands), Sarah Connors (UK), Renée van Diemen (Netherlands), Opha Pauline Dube (Botswana), Kris Ebi (USA), Francois Engelbrecht (South Africa), Marion Ferrat (UK/France), “GLOBAL WARMING OF 1 . 5 ° C an IPCC special report on the impacts of global,” *Ipcc*, no. October 2018, 2018, [Online]. Available: https://www.ipcc.ch/sr15/chapter/summary-for-policy-makers/

[125] K. P. Shine, “Radiative forcing of climate change,” *Space Sci. Rev.*, vol. 94, no. 1–2, pp. 363–373, 2000, doi: 10.1023/A:1026752230256.

[126] Hodnebrog *et al.*, “Global warming potentials and radiative efficiencies of halocarbons and related compounds: A comprehensive review,” *Rev. Geophys.*, vol. 51, no. 2, pp. 300–378, 2013, doi: 10.1002/rog.20013.

[127] U. E. N. C. for E. Assessment, “Changes in atmospheric constituents and in radiative forcing,” pp. 1–2, 2009, [Online]. Available: http://hero.epa.gov/index.cfm?action=reference.details&reference_id=92936

[128] H. E. Armstrong, “The Paris Observatory,” *Nature*, vol. 127, no. 3207, pp. 600–601, 1931, doi: 10.1038/127600a0.

[129] S. Fawzy, A. I. Osman, J. Doran, and D. W. Rooney, “Strategies for mitigation of climate change: a review,” *Environ. Chem. Lett.*, vol. 18, no. 6, pp. 2069–2094, 2020, doi: 10.1007/s10311-020-01059-w.

[130] C. E. Wieners *et al.*, “Solar radiation modification is risky, but so is rejecting it: a call for balanced research,” *Oxford Open Clim. Chang.*, vol. 3, no. 1, pp. 4–7, 2023, doi: 10.1093/oxfclm/kgad002.

[131] H. K. Jeswani, D. M. Saharudin, and A. Azapagic, “Environmental sustainability of negative emissions technologies: A review,” *Sustain. Prod. Consum.*, vol. 33, pp. 608–635, 2022, doi: 10.1016/j.spc.2022.06.028.

[132] S. Cobo *et al.*, “Sustainable scale-up of negative emissions technologies and practices: where to focus,” *Environ. Res. Lett.*, vol. 18, no. 2, 2023, doi: 10.1088/1748-9326/acacb3.

[133] M. Kolokotroni *et al.*, “Cool roofs: High tech low cost solution for energy efficiency and thermal comfort in low rise low income houses in high solar radiation countries,” *Energy Build.*, vol. 176, pp. 58–70, 2018, doi: 10.1016/j.enbuild.2018.07.005.

[134] A. M. Brander *et al.*, “Electricity-specific emission factors for grid electricity,” *Ecometrica*, no. August, pp. 1–22, 2011.

[135] D. Pirvaram, Atousa, O’Brien, Paul, Leungt, Siu Ning, Royon, Laurent, Beysens, “No Title”.

[136] A. Pirvaram, T. Cooper, S. N. Leung, and P. G. O’Brien, “A comprehensive study on using underside infrared reflectors to enhance the performance of radiative cooling structures,” *Energy Convers. Manag.*, vol. 304, no. February, p. 118180, 2024, doi: 10.1016/j.enconman.2024.118180.

[137] N. G. Loeb *et al.*, “Toward optimal closure of the Earth’s top-of-atmosphere radiation budget,” *J. Clim.*, vol. 22, no. 3, pp. 748–766, 2009, doi: 10.1175/2008JCLI2637.1.

[138] K. E. Trenberth, J. T. Fasullo, and J. Kiehl, “Earth’s global energy budget,” *Bull. Am. Meteorol. Soc.*, vol.

90, no. 3, pp. 311–323, 2009, doi: 10.1175/2008BAMS2634.1.

[139] G. C. Johnson, J. M. Lyman, and N. G. Loeb, “Improving estimates of Earth’s energy imbalance,” *Nat. Clim. Chang.*, vol. 6, no. 7, pp. 639–640, 2016, doi: 10.1038/nclimate3043.

[140] P. Balcombe, J. F. Speirs, N. P. Brandon, and A. D. Hawkes, “Methane emissions: choosing the right climate metric and time horizon,” *Environ. Sci. Process. Impacts*, vol. 20, no. 10, pp. 1323–1339, 2018, doi: 10.1039/c8em00414e.

[141] “Acrymax Technologies, AF-130 Product Data.” http://preservationproducts.com/HP-1000-elastomeric-roof-coating

[142] City of Winnipeg, “Emission factors in kg CO2-equivalent per unit,” *WSTP South End Plant Process Sel. Rep.*, pp. 1366–1393, 2011, [Online]. Available: https://www.winnipeg.ca/finance/findata/matmgt/documents/2012/682-2012/682-2012_Appendix_H-WSTP_South_End_Plant_Process_Selection_Report/Appendix 7.pdf

[143] W. Chalmers *et al.*, “Poly ( methyl methacrylate ),” no. January, pp. 1–14, 2019.

[144] C. I. Emissions, I. Guidelines, N. Greenhouse, and G. Inventories, “CHAPTER 3,” pp. 1–110, 2006.

[145] A. Dominguez-Delgado, H. Domínguez-Torres, and C. A. Domínguez-Torres, “Energy and economic life cycle assessment of cool roofs applied to the refurbishment of social housing in southern Spain,” *Sustain.*, vol. 12, no. 14, 2020, doi: 10.3390/su12145602.

[146] J. S. Dolado *et al.*, “Radiative Cooling Properties of Portlandite and Tobermorite: Two Cementitious Minerals of Great Relevance in Concrete Science and Technology,” *ACS Appl. Opt. Mater.*, 2023, doi: 10.1021/acsaom.3c00082.

[147] S. Kotthaus, T. E. L. Smith, M. J. Wooster, and C. S. B. Grimmond, “Derivation of an urban materials spectral library through emittance and reflectance spectroscopy,” *ISPRS J. Photogramm. Remote Sens.*, vol. 94, pp. 194–212, 2014, doi: 10.1016/j.isprsjprs.2014.05.005.

[148] H. C. Ward, S. Kotthaus, L. Järvi, and C. S. B. Grimmond, “Surface Urban Energy and Water Balance Scheme (SUEWS): Development and evaluation at two UK sites,” *Urban Clim.*, vol. 18, no. November, pp. 1–32, 2016, doi: 10.1016/j.uclim.2016.05.001.

[149] R. Seitz, “Bright water: Hydrosols, water conservation and climate change,” *Clim. Change*, vol. 105, no. 3–4, pp. 365–381, 2011, doi: 10.1007/s10584-010-9965-8.

[150] M. Konda, N. Imasato, K. Nishi, and T. Toda, “Measurement of the sea surface emissivity,” *J. Oceanogr.*, vol. 50, no. 1, pp. 17–30, 1994, doi: 10.1007/BF02233853.

[151] H. Akbari, S. Menon, and A. Rosenfeld, “Global cooling: Increasing world-wide urban albedos to offset CO 2,” *Clim. Change*, vol. 94, no. 3–4, pp. 275–286, 2009, doi: 10.1007/s10584-008-9515-9.

[152] J. N. Munday, “Tackling Climate Change through Radiative Cooling,” *Joule*, vol. 3, no. 9, pp. 2057–2060, 2019, doi: 10.1016/j.joule.2019.07.010.

[153] Z. Liu, C. He, Y. Zhou, and J. Wu, “How much of the world’s land has been urbanized, really? A hierarchical framework for avoiding confusion,” *Landsc. Ecol.*, vol. 29, no. 5, pp. 763–771, 2014, doi: 10.1007/s10980-014-0034-y.

[154] S. Joshi *et al.*, “Global high-resolution growth projections dataset for rooftop area consistent with the shared socioeconomic pathways, 2020–2050,” *Sci. Data*, vol. 11, no. 1, 2024, doi: 10.1038/s41597-024-03378-x.

[155] Á. Andueza, C. Pinto, D. Navajas, and J. Sevilla, “Enhanced thermal performance of photovoltaic panels based on glass surface texturization,” *Opt. Mater. (Amst).*, vol. 121, 2021, doi: 10.1016/j.optmat.2021.111511.

[156] T. Sahu, K. K. Ghuman, and P. G. O’Brien, “A review of materials used for carbon dioxide capture,” *Prog.*

*Sustain. Dev. Sustain. Eng. Pract.*, pp. 205–232, Jan. 2023, doi: 10.1016/B978-0-323-99207-7.00003-8.

[157] K. S. Lackner, S. Brennan, J. M. Matter, A. H. A. Park, A. Wright, and B. Van Der Zwaan, "The urgency of the development of CO 2 capture from ambient air," *Proc. Natl. Acad. Sci. U. S. A.*, vol. 109, no. 33, pp. 13156–13162, 2012, doi: 10.1073/pnas.1108765109.

[158] A. Dubey and A. Arora, "Advancements in carbon capture technologies: A review," *J. Clean. Prod.*, vol. 373, no. August, p. 133932, 2022, doi: 10.1016/j.jclepro.2022.133932.

[159] D. Archer, *How Humans Are Changing the Next 100,000 Years of Earth's Climate*. Princeton: Princeton University Press, 2016. doi: doi:10.1515/9781400880775.

[160] H. D. Matthews, "Emissions targets for CO2 stabilization as modified by carbon cycle feedbacks," *Tellus, Ser. B Chem. Phys. Meteorol.*, vol. 58, no. 5, pp. 591–602, 2006, doi: 10.1111/j.1600-0889.2006.00200.x.

[161] S. Jeon and J. Shin, "Directional radiation for optimal radiative cooling," *Opt. Express*, vol. 29, no. 6, p. 8376, 2021, doi: 10.1364/oe.416475.

[162] J. Peoples *et al.*, "Concentrated radiative cooling," *Appl. Energy*, vol. 310, no. November 2021, p. 118368, 2022, doi: 10.1016/j.apenergy.2021.118368.

[163] L. Zhou *et al.*, "Hybrid concentrated radiative cooling and solar heating in a single system," *Cell Reports Phys. Sci.*, vol. 2, no. 2, p. 100338, 2021, doi: 10.1016/j.xcrp.2021.100338.

[164] H. Ma *et al.*, "Multilayered SiO2/Si3N4 photonic emitter to achieve high-performance all-day radiative cooling," *Sol. Energy Mater. Sol. Cells*, vol. 212, no. March, p. 110584, 2020, doi: 10.1016/j.solmat.2020.110584.

[165] Lord SD, *A new software tool for computing Earth's atmospheric transmission of near-and far-infrared radiation. Ames Research Center; 1992.* 1992.

[166] M. Dong, N. Chen, X. Zhao, S. Fan, and Z. Chen, "Nighttime radiative cooling in hot and humid climates," *Opt. Express*, vol. 27, no. 22, p. 31587, 2019, doi: 10.1364/oe.27.031587.

[167] J. Feng, K. Gao, M. Santamouris, K. W. Shah, and G. Ranzi, "Dynamic impact of climate on the performance of daytime radiative cooling materials," *Sol. Energy Mater. Sol. Cells*, vol. 208, no. January, p. 110426, 2020, doi: 10.1016/j.solmat.2020.110426.

[168] X. Li, J. Peoples, P. Yao, and X. Ruan, "Ultrawhite BaSO4Paints and Films for Remarkable Daytime Subambient Radiative Cooling," *ACS Appl. Mater. Interfaces*, vol. 13, no. 18, pp. 21733–21739, 2021, doi: 10.1021/acsami.1c02368.

[169] Z. Cheng, F. Wang, H. Wang, H. Liang, and L. Ma, "Effect of embedded polydisperse glass microspheres on radiative cooling of a coating," *Int. J. Therm. Sci.*, vol. 140, no. March, pp. 358–367, 2019, doi: 10.1016/j.ijthermalsci.2019.03.014.

[170] C. H. Xue *et al.*, "Fabrication of superhydrophobic P(VDF-HFP)/SiO2 composite film for stable radiative cooling," *Compos. Sci. Technol.*, vol. 220, no. May 2021, 2022, doi: 10.1016/j.compscitech.2022.109279.

[171] Y. Zhang, X. Chen, B. Cai, H. Luan, Q. Zhang, and M. Gu, "Photonics Empowered Passive Radiative Cooling," *Adv. Photonics Res.*, vol. 2, no. 4, pp. 1–12, 2021, doi: 10.1002/adpr.202000106.

[172] G. Gangisetty and R. Zevenhoven, "A Review of Nanoparticle Material Coatings in Passive Radiative Cooling Systems Including Skylights," *Energies*, vol. 16, no. 4, 2023, doi: 10.3390/en16041975.

[173] H. Ma *et al.*, "Flexible Daytime Radiative Cooling Enhanced by Enabling Three-Phase Composites with Scattering Interfaces between Silica Microspheres and Hierarchical Porous Coatings," *ACS Appl. Mater. Interfaces*, vol. 13, no. 16, pp. 19282–19290, 2021, doi: 10.1021/acsami.1c02145.

[174] A. W. Harrison and M. R. Walton, "Radiative cooling of TiO2 white paint," *Sol. Energy*, vol. 20, no. 2, pp. 185–188, 1978, doi: 10.1016/0038-092X(78)90195-0.

[175] H. Bao, C. Yan, B. Wang, X. Fang, C. Y. Zhao, and X. Ruan, “Double-layer nanoparticle-based coatings for efficient terrestrial radiative cooling,” *Sol. Energy Mater. Sol. Cells*, vol. 168, no. April, pp. 78–84, 2017, doi: 10.1016/j.solmat.2017.04.020.

[176] S. Zhang *et al.*, “Full daytime sub-ambient radiative cooling film with high efficiency and low cost,” *Renew. Energy*, vol. 194, pp. 850–857, 2022, doi: 10.1016/j.renene.2022.05.151.

[177] T. M. J. Nilsson, “Pergamon,” vol. 5, pp. 310–317, 1994.

[178] N. Lavielle, A. Mongruel, T. Bourouina, L. Royon, and D. Beysens, “Plastic foil micro-grooved by embossing enhances dew collection without aging effects,” *Mater. Today Sustain.*, vol. 24, no. September, p. 100566, 2023, doi: 10.1016/j.mtsust.2023.100566.

[179] D. Beysens, *“Dew Water,” in Dew Water*. River Publishers, 2018.

[180] X. Berger and J. Bathiebo, “Directional spectral emissivities of clear skies,” *Renew. Energy*, vol. 28, no. 12, pp. 1925–1933, 2003, doi: 10.1016/S0960-1481(03)00059-4.

[181] N. Cheng *et al.*, “Nanosphere-structured hierarchically porous PVDF-HFP fabric for passive daytime radiative cooling via one-step water vapor-induced phase separation,” *Chem. Eng. J.*, vol. 460, no. January, p. 141581, 2023, doi: 10.1016/j.cej.2023.141581.

[182] J. Trosseille, A. Mongruel, L. Royon, and D. Beysens, “Radiative cooling for dew condensation,” *Int. J. Heat Mass Transf.*, vol. 172, p. 121160, 2021, doi: 10.1016/j.ijheatmasstransfer.2021.121160.

[183] J. Trosseille, A. Mongruel, L. Royon, and D. Beysens, “Effective substrate emissivity during dew water condensation,” *Int. J. Heat Mass Transf.*, vol. 183, p. 122078, 2022, doi: 10.1016/j.ijheatmasstransfer.2021.122078.